

**Charge carrier traps in organic semiconductors: A review on the underlying physics and impact on electronic devices**

Journal:	<i>Journal of Materials Chemistry C</i>
Manuscript ID	TC-REV-10-2019-005695.R1
Article Type:	Review Article
Date Submitted by the Author:	13-Dec-2019
Complete List of Authors:	Haneef, Hamna; Wake Forest University, Physics and Center for Functional Materials Zeidell, Andrew; Wake Forest University, Physics Jurchescu, Oana; Wake Forest University, Physics

# 1 **Charge carrier traps in organic semiconductors: A review on the underlying** 2 **physics and impact on electronic devices**

3 Hamna F. Haneef,<sup>1</sup> Andrew M. Zeidell,<sup>1</sup> and Oana D. Jurchescu<sup>1</sup>

4 <sup>1</sup>Department of Physics and Center for Functional Materials, Wake Forest University, Winston  
5 Salem, NC 27109, USA

6

## 7 **1. Introduction**

8         The promise of low-cost manufacturing, ease of processing, mechanical flexibility and  
9 versatility in chemical synthesis make organic semiconductors (OSCs) very attractive as  
10 components in electronic and opto-electronic devices. Examples include organic field-effect  
11 transistors (OFETs), organic light-emitting diodes (OLEDs), organic photovoltaics (OPV) and  
12 sensors.<sup>1-6</sup> OSCs consist of conjugated molecules containing delocalized electrons resulting from  
13 the overlap of  $\pi$ -orbitals. The spatial overlap between the molecular orbitals of adjacent  
14 molecules determines the intermolecular electronic coupling and thereby the mechanism of  
15 charge transport.<sup>5,7-9</sup> The intermolecular interactions in the condensed state are weak, mainly  
16 consisting of van der Waals forces, as opposed to covalent and ionic bonds prevalent in inorganic  
17 solids. As a result, the processing requirements, as well as the mechanical, optical and electronic  
18 properties of OSCs, differ considerably from conventional crystalline or elemental  
19 semiconductors.<sup>4,10,11</sup> Binding energies in OSCs are typically low ( $\sim 10$  kcal mol<sup>-1</sup>, for reference,  
20 in crystalline Si (c-Si) the energy is  $\sim 80$  kcal mol<sup>-1</sup>),<sup>12</sup> which makes them attractive for printable  
21 electronic applications.<sup>1</sup> Their mechanical properties, coupled with manufacturing in ambient  
22 conditions, render them compatible with flexible substrates such as plastic, enabling their use in  
23 applications like bioelectronics, display technologies and wearable electronics.

24 OSCs are clearly exciting materials, providing a wealth of technologically attractive  
25 properties and intriguing platforms to explore new science, but there are still many unanswered  
26 questions and challenges that need to be addressed before their widespread adoption. For  
27 example, charge carrier mobilities in OSCs rarely exceed  $10 \text{ cm}^2 \text{ V}^{-1} \text{ s}^{-1}$ , a value which is orders  
28 of magnitude lower than in c-Si or graphene, where mobilities in the order of  $10^3 \text{ cm}^2 \text{ V}^{-1} \text{ s}^{-1}$  and  
29  $10^6 \text{ cm}^2 \text{ V}^{-1} \text{ s}^{-1}$ , respectively, have been reported.<sup>13</sup> The main reason for such low mobilities is the  
30 *localization* of charge carriers, a phenomenon that alters the already narrow bands resulting from  
31 van der Waals intermolecular interactions. In the early years of research on organic electronics  
32 (1950's), localization of charge carriers in molecular crystals was attributed to polarization  
33 whereby charge carriers interact with the surrounding electrons and nuclei in the lattice to form  
34 self-localized 'polarons'.<sup>14</sup> The transport of polarons was modelled using the polaron band  
35 theory and small polaron theory.<sup>15</sup> Most crystalline OSCs measured in the nineties showed  
36 activated transport, which led to the wide acceptance of hopping as the dominant charge  
37 transport mechanism in OSCs.<sup>12,15</sup> Later, observations of power-law temperature dependence of  
38 mobilities in high quality single crystals, which is reminiscent of band (delocalized) charge  
39 transport, challenged these theories.<sup>15</sup> In the semi-classical description, band transport implies  
40 that charge carriers are delocalized over large distances compared to the lattice spacing and are  
41 only occasionally scattered by impurities and lattice vibrations. In OSCs however, delocalization  
42 of charge carriers is limited to a few molecules, hence the term '*band-like*' was introduced to  
43 describe charge transport in these materials.<sup>16</sup> Despite the observation of band-like transport, the  
44 mean free path of charge carriers in OSCs is comparable, and sometimes even lower than the  
45 intermolecular spacing, supporting localization of charge carriers and consequently low  
46 mobilities. This was a rather puzzling contradiction which piqued the interest of the scientific

47 community. Recently it has been shown that dynamic disorder caused by large amplitude thermal  
48 motions of molecules is the main factor that limits the mobilities down to a few tens of  $\text{cm}^2 \text{V}^{-1} \text{s}^{-1}$ .  
49 <sup>1,13</sup> This type of localization is short lived (*transient* localization) and survives only up to the  
50 timescale of the molecular vibrations, which in turn, can be suppressed at sufficiently low  
51 temperatures. New models based on a combination of quantum and classical dynamic concepts  
52 have been proposed to reconcile the coexistence of band-like/localized charge carriers and  
53 establish a proper theory to describe charge transport in OSCs.<sup>13,17</sup>

54         Localization of charge carriers can be caused by other sources of disorder such as  
55 chemical impurities and structural defects (static disorder). In addition, these sources can lead to  
56 the formation of electronic states in the band gap of the OSC. These in-gap states can  
57 subsequently trap charge carriers and hinder their transport, further preventing the OSC from  
58 realizing their intrinsic mobilities. Charge carrier trapping is a ubiquitous phenomenon that has  
59 repercussions on the performance and stability of OSC opto-electronic devices, as well as on our  
60 ability to access their intrinsic properties. Understanding the mechanisms and processes related  
61 to trap formation, the dynamics and timescales over which these processes occur is decisive in  
62 extracting fundamental performance limits of OSCs and subsequently engineering high-  
63 performance devices. This article aims to provide a comprehensive and timely review on the  
64 phenomenon of charge carrier trapping in OSCs, with emphasis on its impact on device  
65 operation. Starting with the definition of traps in Section 2, we continue by describing the  
66 different origins of traps in OSCs (Section 3), followed by a discussion on the effect of traps on  
67 the performance of organic opto-electronic devices (Section 4) and on the mechanism of charge  
68 transport in OSCs (Section 5). An overview of the experimental techniques available to detect  
69 and characterize traps will be provided in Section 6. Charge carrier traps can also be viewed as

70 an opportunity for advanced detection: in Section 7, we discuss the exploitation of traps for  
71 organic-electronics-based sensing and memory applications.

72

## 73 **2. What are charge carrier traps?**

74 Before we move onto the description of traps, we introduce the density of states (DOS)  
75 function, which describes the energetic distribution of electronic states within energy bands. In a  
76 perfectly-ordered, crystalline semiconductor, such as c-Si, the density of delocalized (extended)  
77 states takes the form of a lying parabola ( $E^{1/2}$  dependency, where  $E$  is the energy of an electronic  
78 state) with well-defined band edges and hence a band gap (see Figure 1a).<sup>18</sup> In semiconductors  
79 with weak localization, such as amorphous Si (a-Si), the extended states tail into the band gap to  
80 create localized states as shown in Figure 1b.<sup>19</sup> These tail states are often modelled by an  
81 exponential function.<sup>20,21</sup> In this case, an energy gap and band edges cannot be precisely defined;  
82 instead a *mobility-edge* that separates extended states from localized states was introduced.<sup>19,22</sup> In  
83 disordered semiconductors, the localization is strong and the DOS is typically approximated with  
84 a Gaussian distribution (Figure 1c) or an exponential distribution (Figure 1d).<sup>20,23</sup> The highest  
85 occupied molecular orbital (HOMO) and the lowest unoccupied molecular orbital (LUMO) are  
86 analogous to the top of the valence band and bottom of the conduction band, respectively. These  
87 terms will be used interchangeably throughout this review. For a Gaussian shaped DOS, an  
88 *effective transport energy* is defined as the energy at which a charge carrier equilibrates over  
89 time after multiple hopping between the localized states.<sup>19,24</sup> The onset of the HOMO and  
90 LUMO are defined at the onset of the Gaussian when the tangent through the inflection point  
91 crosses the baseline (see Figure 1c).<sup>11,19</sup> Depending on the extent of localization of charge  
92 carriers, which is decided by various factors such as the molecular structure, molecular packing

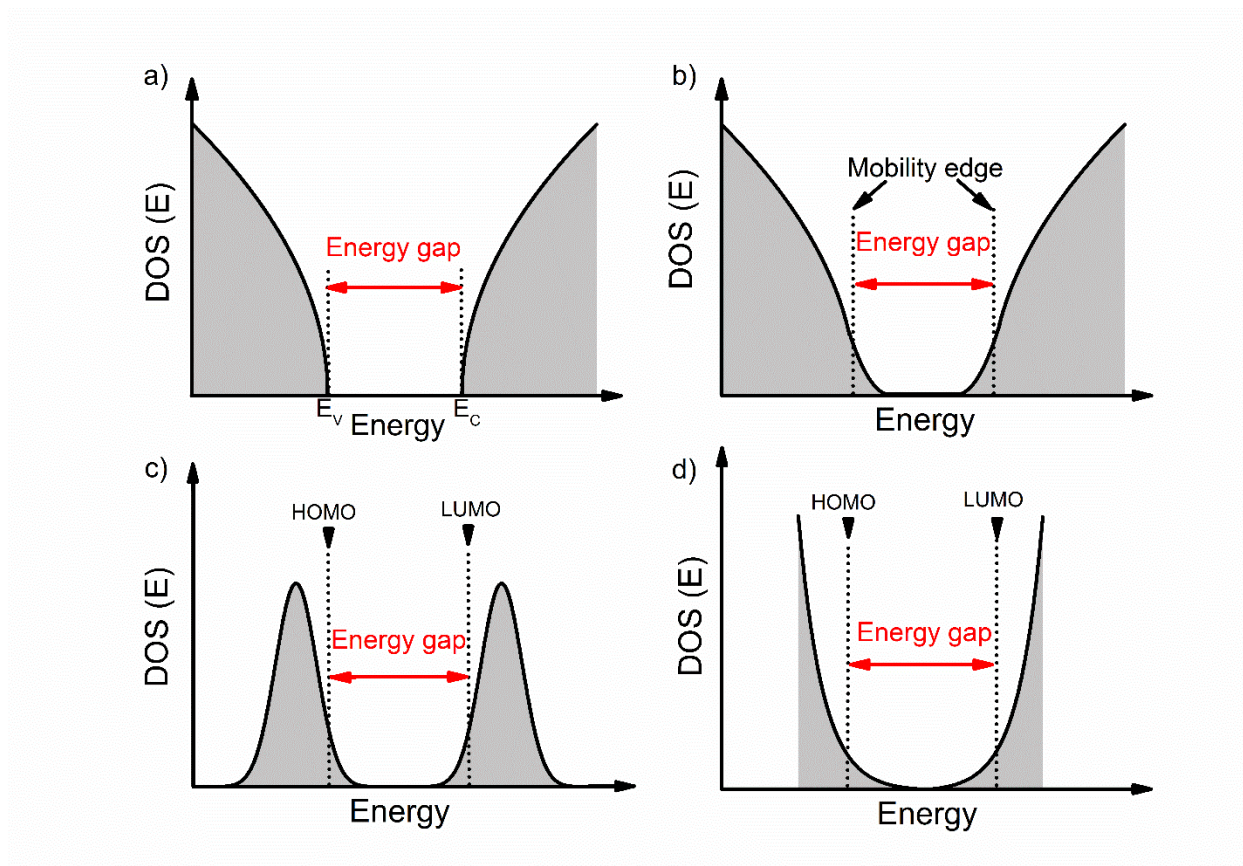
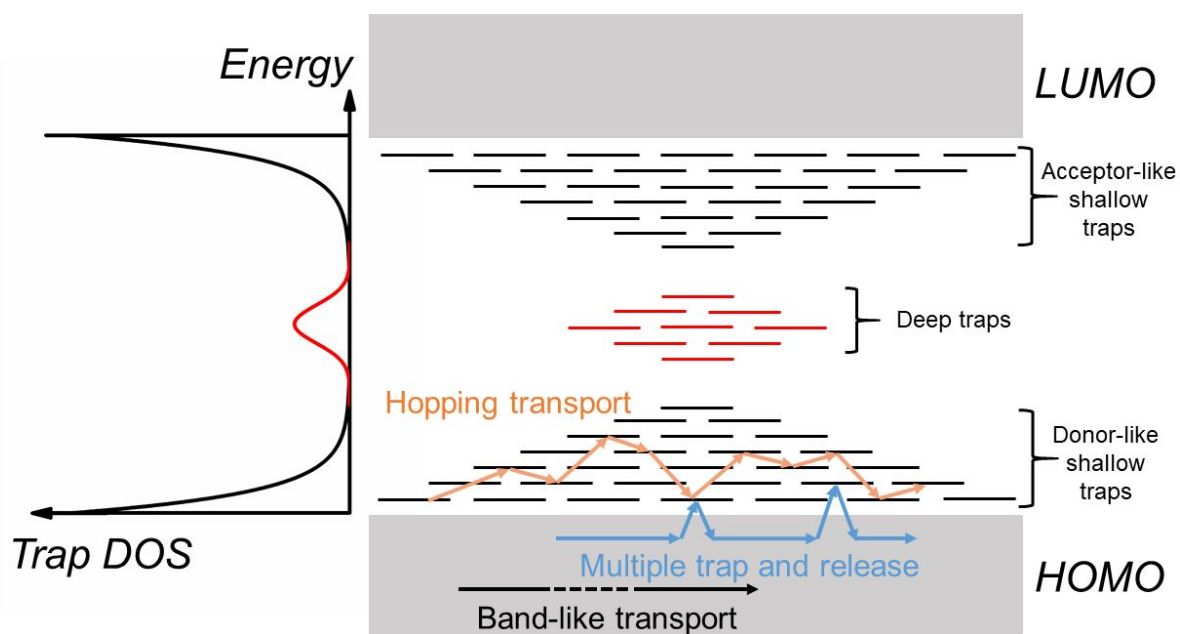


Figure 1. Extended states DOS function of a) crystalline OSCs, b) crystalline OSCs with weak localization, and c), d) polycrystalline/amorphous OSCs assuming Gaussian and exponential models, respectively.

93 and the extent of disorder, the shape of the DOS function can be approximated to one of the four  
 94 forms illustrated in Figure 1. Ideal, perfectly-ordered single crystals adopt the DOS shape in  
 95 Figure 1a; however, the disorder induced by thermal molecular motions (discussed in Section  
 96 3.1) gives rise to tail states in the band gap and therefore their DOS is better approximated by the  
 97 curve in Figure 1b.<sup>13,25–27</sup> Figure 1c and Figure 1d are typically used to represent the DOS in  
 98 polycrystalline and amorphous OSC films.<sup>11,20,23,28</sup>

99           An *electronic trap* is any imperfection in the semiconductor that creates localized  
100 electronic states spatially distributed around the site of the imperfection and energetically  
101 distributed within the band gap of the semiconductor. Depending on their relative energetic  
102 positions from the band edge (trap depth) at a given temperature, traps can be *shallow* if located  
103 in the vicinity (a few  $kT$ ) of the band edges, or *deep* if they lie further (several  $kT$ ) from the band  
104 edges as illustrated in Figure 2, where  $k$  is the Boltzmann's constant and  $T$  the temperature.  
105 Localized tail states in the band gap are generally considered shallow traps, with acceptor-like  
106 states near the LUMO edge and donor-like states near the HOMO edge representing trap states  
107 for holes and electrons, respectively. A trap can capture and restrain a charge carrier temporarily  
108 until it is released back into the band by an external stimulus such as electric field, thermal  
109 energy or a photon. For example, in the multiple-trap and release (MTR) model, charges moving  
110 within delocalized states are trapped by a localized shallow trap state in the band gap, then  
111 released back into the energy band by thermal energy as depicted by the blue arrows in Figure  
112 2.<sup>29,30</sup> A band-like motion (which occurs within delocalized states) is also illustrated in Figure 2,  
113 in black arrows, for comparison. If the trap densities are high, trapped charge carriers can  
114 participate in transport through thermally-activated hopping or tunneling from one localized state  
115 to another (orange arrows in Figure 2).<sup>31</sup> Thermal detrapping of charge carriers is possible if the  
116 trap depth is sufficiently low ( $\sim kT$ ); charge carriers residing in shallow traps at a given  
117 temperature are more likely to get thermally excited back into the band, while those in a deep  
118 trap have a negligible probability of being thermally excited.<sup>32</sup> Such deep states often act as  
119 recombination centers for charge carriers reducing their overall lifetime.

120           A DOS function to represent localized electronic states within the band gap of an OSC  
121 can be defined. Such a function is referred to as *trap DOS*. Traps can have discrete energy levels



122

Figure 2. (Left) The trap DOS function represents shallow traps resulting from tail states (black) and deep traps (red) in the band gap. (Right) Schematic spatial and energy diagram of an OSC containing localized trap states in the band gap. Tail states forming acceptor-like and donor-like shallow traps are shown in black, while deep traps are shown in red. Arrows represent different transport regimes possible in an OSC; band-like transport (black), MTR (blue) and thermally-activated hopping transport between localized states (orange).

123 or a quasi-continuous energy distribution that is often described using an exponential or a  
 124 Gaussian function.<sup>33–36</sup> The left panel of Figure 2 illustrates a Gaussian distribution of trap states  
 125 deep in the band gap (red curve) in addition to the disorder-induced tail states (black curve)  
 126 extending into the band gap, and which act as shallow traps.

127

128

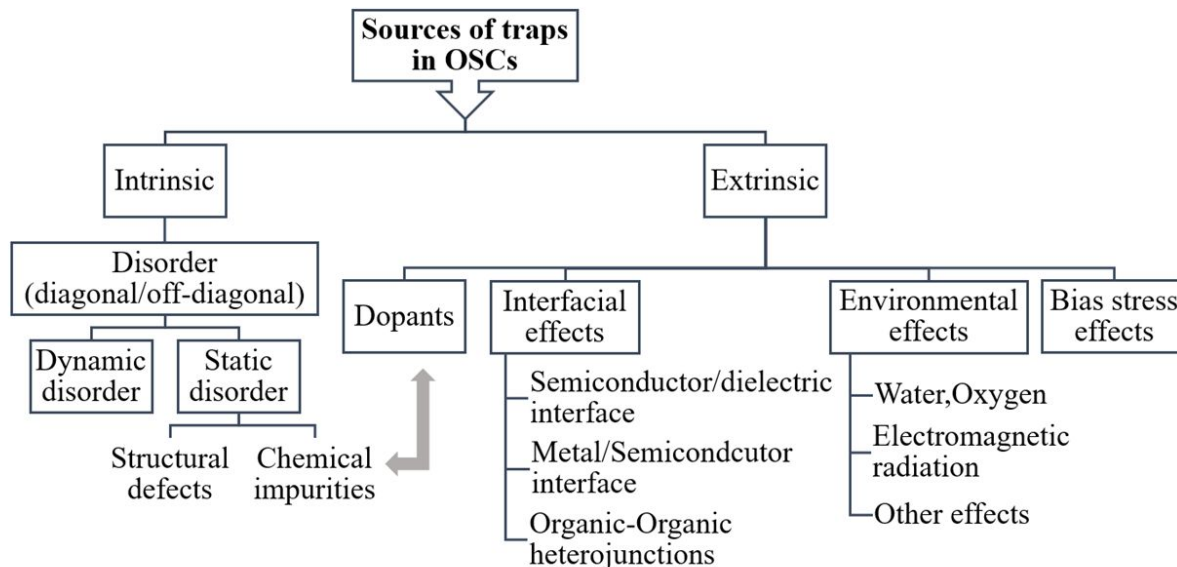


Figure 3. Sources of charge carrier traps in OSCs.

129

### 130 3. Sources of traps in organic semiconductors

131 Electronic traps in OSCs can originate from varying sources, as summarized in the  
 132 scheme in Figure 3. The main source of traps in OSCs is disorder. Structural defects and  
 133 chemical impurities cause static disorder and are considered *intrinsic* sources of traps in OSCs.  
 134 They form during or after crystal/film formation and can be minimized through careful control of  
 135 the growth process. In addition, dynamic disorder is an intrinsic source of traps. *Extrinsic* traps  
 136 can be intentionally or unintentionally introduced by either exposure to gases, electromagnetic  
 137 radiation, temperature gradients, bias stress, dopants, or by interfacing with other materials such  
 138 as a metal, dielectric or another OSCs. Since the energetic landscape involved in the presence of  
 139 inadvertent chemical impurities and deliberately added dopants is similar, dopants will be  
 140 discussed in the context of chemical impurities. In this section, we will discuss each type of traps

141 included in the scheme and will provide examples on how they impact material and device  
142 properties.

143

### 144 **3.1. Disorder**

145 Perturbations or imperfections in the crystal structure, existing either in a single unit cell  
146 or extending over several unit cells, can locally destroy the crystal and translational symmetry,  
147 thereby introducing disorder into the system. The spatial distribution of structural properties such  
148 as intermolecular electronic coupling results in *structural* disorder, also called *off-diagonal*  
149 disorder.<sup>8</sup> If the disorder translates into fluctuations in site energy (i.e., HOMO or LUMO energy  
150 level) of a molecule or molecular segment, it is referred to as *energetic* disorder or *diagonal*  
151 disorder.<sup>8</sup> Any structural disorder in the cartesian domain will inevitably give rise to energetic  
152 disorder in the energy domain.<sup>24</sup> Energetic disorder is often modelled by a Gaussian distribution  
153 of energy with a standard deviation quantifying the extent of disorder.<sup>37</sup> An exponential DOS is  
154 also used to model disorder-induced tail states in the band gap.<sup>20,21</sup>

155 The disorder can be *dynamic* or *static*: dynamic disorder is caused by thermal motions of  
156 the molecules (intermolecular and intramolecular), i.e. from electron-phonon interactions, while  
157 static disorder is caused by structural defects (Section 3.1.1.) and chemical impurities (section  
158 3.1.2.). The major difference between the two is that the former results in time-dependent  
159 variations in the site energies and transfer integrals and occurs throughout the entire crystal,  
160 while the latter is time-independent and occurs only at specific locations where the defects are  
161 present. Dynamic disorder can destroy the already narrow electronic energy bands, resulting in  
162 localization of charge carriers. However, the disorder lasts only up to the timescale of the

163 thermal motions (hence the term ‘*transient localization*’) and can be sufficiently reduced at low  
164 temperatures.<sup>13</sup> Static disorder can also result in charge carrier localization (Anderson  
165 localization) arising from the variations in electron potentials.<sup>38</sup> Both dynamic disorder and static  
166 disorder introduce localized tail states in the band gap, with the latter creating additional in-gap  
167 states due to the presence of structural inhomogeneities. Tail states induced by dynamic disorder  
168 form even in nominally perfect OSC single crystals and represents the major performance  
169 limiting factor in such materials.<sup>27,39</sup> Moreover, the density of tail states resulting from large  
170 amplitude thermal motions is much higher than those resulting from structural inhomogeneities,  
171 and hence they play a key role in determining the details of charge transport in materials in  
172 which the electronic coupling between molecules is weaker compared to the electron-phonon  
173 coupling.<sup>40</sup> A discussion on the effect of disorder on charge transport is beyond the scope of this  
174 review and the reader is directed to the rich literature existing on the subject.<sup>8,13,17,37,41–43</sup> In this  
175 review, the discussion will be limited to the disorder-induced gap states that can potentially trap  
176 charge carriers. Theoretical calculations confirmed the existence of a tail of gap states near the  
177 valence band edge resulting from thermal molecular motions.<sup>25,44–46</sup> In pentacene, for example,  
178 the states were modelled exponentially to yield a tail breadth of 6.9 meV at 100 K, increasing to  
179 12.7 meV at 300 K due to higher amplitude thermal motions at elevated temperatures.<sup>25</sup> By using  
180 a combination of temperature-dependent FET and charge modulation spectroscopy (CMS)  
181 measurements Sirringhaus and coworkers confirmed that dynamic disorder induces shallow  
182 traps.<sup>47</sup> They found that the degree of localization is sample dependent and charge carriers are  
183 highly localized in pentacene films, a phenomena that does not occur in 2,8-difluoro-5,11-  
184 bis(triethylsilylethynyl) anthradithiophene (diF-TES ADT), even at low temperatures. Band gap  
185 tail states have been experimentally observed in several materials such as single crystals of

186 rubrene and their derivatives, but their precise origin remains unclear<sup>48,49</sup>. Troisi and co-workers  
187 pointed out that they are similar to those detected in inorganic semiconductors which result from  
188 intrinsic electronic disorder.<sup>15</sup> Experimental evidence on the presence of gap-states due to static  
189 disorder and their role in charge carrier trapping will be provided in the succeeding sections  
190 (3.1.1 and 3.1.2).

191

### 192 **3.1.1. Structural defects**

193 Structural inhomogeneities within the OSC can yield intrinsic traps. Here we begin with  
194 the discussion of such defects in OSC single crystals and later extend the discussion towards thin  
195 films. Structural imperfections in the form of lattice defects exist in every real crystal and the  
196 number of such defects depends on the method as well as the rate of crystal growth.<sup>50</sup> Crystal  
197 defects can be categorized as point defects or extended defects. While the former reside at a  
198 specific lattice site (e.g. vacancy), the latter extend over several lattice sites. Extended defects  
199 can be in the form of line defects such as dislocations, or planar defects such as stacking faults.  
200 Each molecule located in the vicinity of the defect(s) is displaced from its equilibrium position  
201 and a charge carrier residing on such a molecule will experience a change in its electronic  
202 polarization energy,  $P$ . Variations in the local electronic polarization energies for charge carriers  
203 in the vicinity of such defects result in the formation of localized trapping states with energies  
204 distributed quasi-continuously in the band gap.<sup>33</sup> Localized states with higher electronic  
205 polarization energy ( $\Delta P > 0$ ) are formed in compressed regions of the lattice and act as charge  
206 carrier traps. In expanded regions of the lattice, e.g. in the vicinity of a vacancy, localized states  
207 with lower electronic polarization energy ( $\Delta P < 0$ ) can be created below/above the

208 HOMO/LUMO levels. While these states are energetically inactive for charge carrier trapping,  
209 hence called anti-traps, they can hamper transport by acting as scattering centers for charge  
210 carriers. In addition to changes in electronic polarization energies, structural defects also cause  
211 changes in electronic coupling between molecules. In compressed regions of the lattice, the  
212 electronic coupling between molecules is stronger due to the narrower spacing between them.  
213 Likewise, weaker electronic couplings exist in dilated regions of the lattice.

214 *Dislocations* in molecular crystals have been studied since the early 70's.<sup>33,51-54</sup> Thomas  
215 and Williams showed that in anthracene crystals molecules residing within ca. 400 Å radius from  
216 the site of dislocation act as traps for holes.<sup>52</sup> Dislocations in naphthalene crystals have been  
217 identified by Lohman and Wehl as electron traps.<sup>53</sup> The density of dislocations mainly depends  
218 on the growth technique; vapor-grown crystals typically have a lower dislocation density  
219 compared to crystals grown from the melt or solution.<sup>52</sup> In addition to being a charge trapping  
220 site by itself, edge dislocations readily accommodate impurities around their core, potentially  
221 creating additional trapping states.<sup>52</sup>

222 *Step edges* were identified as electron traps in single crystals of N, N'-bis-  
223 (heptafluorobutyl)-2,6-dichloro-1,4,5,8-naphthalene tetra- carboxylic diimide (Cl<sub>2</sub>-NDI) using  
224 scanning Kelvin probe microscopy (SKPM).<sup>55</sup> It was found that the OFET threshold voltages and  
225 mobilities depended strongly on the density of step edges, with the former decreasing and the  
226 latter increasing with increased step densities.

227 *Grain boundaries* (GBs) present in OSC thin films add to structural defects within the  
228 grain and hamper charge carrier transport,<sup>56-61</sup> although some exceptions exist.<sup>62</sup> The discussion  
229 of whether they act as traps or energy barriers for charge carriers has been controversial, both

230 phenomena resulting in thermally-activated transport.<sup>32,63</sup> Spatially resolved techniques were  
231 adopted to access the local nature of trapping in polycrystalline thin films. Marohn and  
232 coworkers used electron force microscopy to study the spatial distribution of traps as a function  
233 of gate-source voltage in pentacene thin-film transistors.<sup>64–66</sup> They found that the traps are not  
234 only concentrated on grain boundaries, but distributed throughout the film. On the other hand,  
235 using scanning probe microscopy measurements, Frisbie and coworkers observed that the surface  
236 electrostatic potential at GBs is lower than that in the crystallites, which indicates that holes are  
237 predominantly trapped at GBs.<sup>67</sup> This result is in agreement with the work by Horowitz et al. and  
238 Sirringhaus and coworkers.<sup>68,69</sup> Kaake et al. suggested that charge carriers are trapped within the  
239 grains, while the surrounding grain boundaries act as insulating barriers for the trapped charge  
240 carriers preventing them from crossing the grain boundaries.<sup>63</sup> Their interpretation was based on  
241 the weaker electronic coupling between molecules located in grain boundaries compared to those  
242 located inside the grains, a phenomenon that pushes the HOMO and LUMO levels into the band  
243 rather than into the band gap and hence does not cause charge carrier trapping. Teague et al.  
244 detected a pronounced potential drop at GBs,<sup>70</sup> in agreement with earlier studies which found an  
245 order of magnitude larger resistance across the grain boundaries than within the grains.<sup>71</sup> The  
246 existence of different types of GBs resulting from different processing conditions, as indicated  
247 by Lee et al. and Jimison et al., might be the cause of such different responses.<sup>72,73</sup>

248         Structural defects in the form of *stacking faults* were detected in pentacene thin-films  
249 using a combination of electronic structure calculations and scanning tunneling microscopy.<sup>74</sup> It  
250 was proposed that compressive stress during film growth causes the molecules to slide along  
251 their long-axis, leading to larger molecular overlap, which results in the formation of shallow  
252 traps with energies  $\leq 100$  meV close to the band edges. In solution deposited small molecule

253 OSCs, this type of defect was healed by introducing gentle vibrations during crystallization, and  
254 a reduction in the density of trap states was confirmed by spectral analysis of the trap density of  
255 states.<sup>75</sup> *Line dislocations* have been identified in pentacene thin films by using a combination of  
256 scanning probe microscopy and chemical etching.<sup>67</sup>

257 In polymers, conformational defects such as *kinks* in the backbone can introduce both  
258 shallow and deep trapping states.<sup>76,77</sup> The *kinks* can break the conjugation and generate energetic  
259 disorder resulting in a sequence of conjugated segments each having different HOMO and  
260 LUMO levels,. Synthesis routes to minimize the energetic disorder in amorphous polymers have  
261 been proposed. For example, the synthesis of the polymer poly(para-phenylene) (PPP) by  
262 planarization of the polymer backbone (ladder polymer) yielded well-defined conjugation length  
263 and interchain order resulting in high-performance OLEDs.<sup>77</sup> In indacenodithiophene-  
264 benzothiadiazole (IDT-BT), a donor-acceptor copolymer that has gained a lot of attention lately  
265 for its high charge carrier mobilities,<sup>78</sup> the performance is obtained in spite of its low  
266 crystallinity.<sup>79</sup> These electrical properties that are approaching a trap-free limit result from an  
267 efficient transport along the rigid backbone, with occasional hopping through  $\pi$ -stacks. In fact,  
268 even though amorphous polymers lack long-range order, they contain ordered crystalline  
269 domains that obey the Physics of crystalline polymers.<sup>80</sup> Karki et al. used solid state nuclear  
270 magnetic resonance (NMR) spectroscopy to quantify the relative densities of ordered and  
271 disordered regions of two structurally distinct polymer films highlighting the impact of the  
272 molecular structure on the degree of order.<sup>80</sup>

273

274

### 275 3.1.2. Chemical impurities/dopants

276 The presence of guest molecules in the form of inadvertently existing chemical impurities  
277 (formed upon chemical degradation, synthesis byproducts), or deliberately added dopants in a  
278 host, can introduce trapping states with a broad range of energies in the band gap. The energy  
279 levels of the guest molecule are, in general, different than that of the host and these differences is  
280 the basis for the formation of such states. On zero-order approximation, the localized trapping  
281 states can be considered to be discrete. Hence, for hole traps, the energy of the trapping state,  $E_t^h$ ,  
282 is determined by the difference between the ionization energy ( $\sim$  energy of the HOMO level) of  
283 the guest and that of the host. Similarly, for electron traps,  $E_t^e$  is the difference in electron  
284 affinity ( $\sim$  energy of the LUMO level) between the guest and the host, i.e.,

$$E_t^h = I_G - I_H \quad (1)$$

$$E_t^e = A_G - A_H \quad (2)$$

285 Where  $I$  and  $A$  are the ionization energy and the electron affinity of the respective molecules,  
286 denoted by the subscripts  $G$  and  $H$  which stand for guest and host molecules respectively, and  $e$   
287 represent electrons and  $h$  holes. In addition, a difference in the electronic polarization energy of  
288 the host and guest molecules ( $\Delta P$ ), caused by the distortion of the host lattice due to the presence  
289 of the guest molecule, can also, to some degree, impact the energy of the trapping state. Whether  
290 or not the lattice is compressed or dilated decides the sign of  $\Delta P$  as mentioned earlier.  $\Delta P$  is  
291 found to be within 0.1 eV and is generally ignored to obtain the simplified equations 1 and 2,  
292 except for the case of deep trapping caused by impurities, where  $\Delta P$  is significant.<sup>33</sup>

293 Figure 4 illustrates several hypothetical situations in which charge carrier trapping or  
294 anti-trapping states are formed by the presence of guest molecules in a host lattice. In the first

295 case (Figure 4a), the HOMO and the LUMO levels of the guest are positioned within the band

296 gap of the host, therefore generating trap states for both holes and electrons. For anthracene

297 crystals doped with tetracene guest molecules, Karl showed that hole traps formed at 0.42 eV

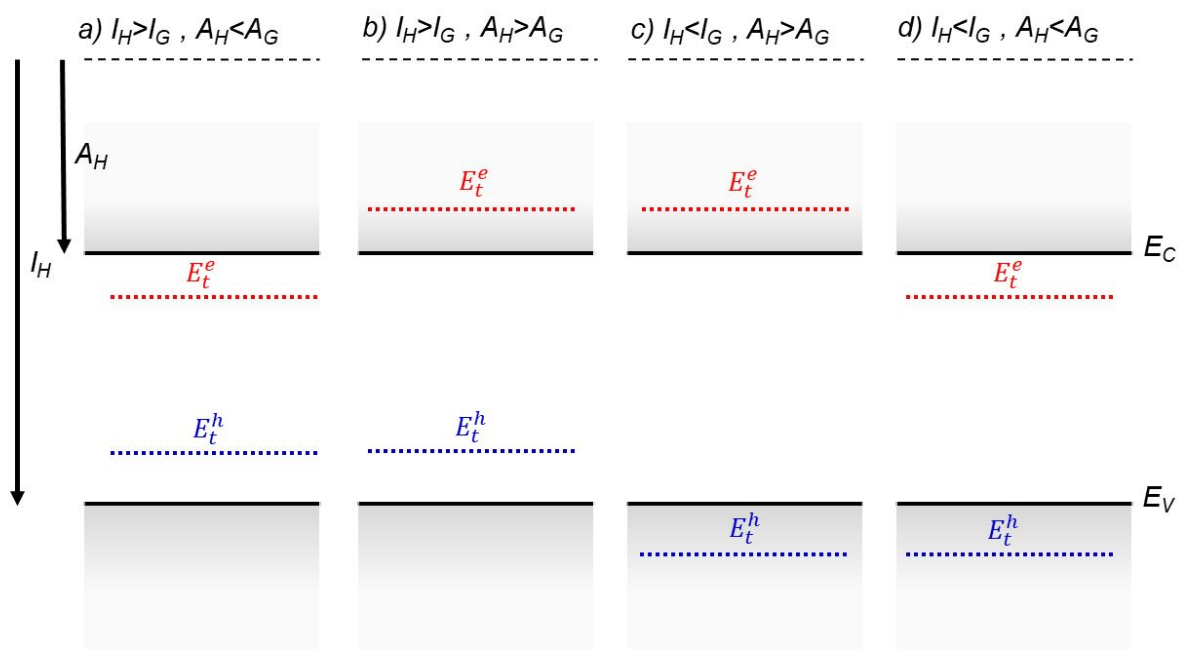


Figure 4. Charge carrier trapping and anti-trapping states resulting from the presence of a guest molecule in a host lattice. Additional in-gap states are not shown for clarity. Solid lines represent the band edges of the host molecule and broken blue lines and red lines represent discrete trapping states for holes and electrons respectively. a) trap state for both holes and electrons, b) trap state for holes and anti-trap state for electrons, c) anti-trap state for both holes and electrons and d) anti-trap state for holes and trap state for electrons.

298 form the valence band edge and electron traps at 0.12-0.17 eV from the conduction band edge.<sup>81</sup>  
 299 An order of magnitude reduction in the hole mobilities was observed even with 0.5 ppm of  
 300 tetracene as a result of the dominant hole trapping.<sup>82</sup> The transport mechanism was band-like for  
 301 the pristine crystal, as determined from time of flight measurements, and MTR for the crystal  
 302 doped with tetracene. In Figure 4b, the guest molecule introduces trap states only for holes, such  
 303 as in the case of anthracene crystals doped with phenothiazine, where the trap was detected at 0.8  
 304 eV from the HOMO level using time of flight measurements.<sup>83</sup> The example illustrated in Figure

305 4c presents a chemical impurity with ionization energy greater than, and electron affinity less  
306 than those of the host. Such an impurity is energetically inert. Even though this type of impurity  
307 is not directly associated with charge carrier trapping, it still contributes to a local distortion of  
308 the lattice and can act as a scattering center for charge carriers. The concentration of the  
309 impurities or dopants will determine the total scattering events. Tetracene molecules in an  
310 anthracene host is such an example, where anti-traps for both electron and holes are  
311 formed.<sup>33,81,83</sup> Finally, panel 4d describes the case when the guest molecule introduces trap states  
312 for electrons only. Using time of flight measurements, Karl detected electron trapping in  
313 anthracene crystals doped with acidine, phenazine and anthraquinone at energies 0.2 eV, 0.54 eV  
314 and 0.6 eV respectively from the conduction band edge.<sup>81</sup>

315 Chemical degradation can also lead to the formation of traps. Oxidation is one of the most  
316 common forms of degradation in OSCs. In the case of acene crystals, oxidation leads to the  
317 formation of quinones. In anthracene and tetracene crystals, the respective quinones form deep  
318 traps for electrons, as confirmed by photoemission measurements.<sup>33</sup> Photo-oxidation of the  
319 crystals resulted in an increased concentration of such impurities. In pentacene single crystals,  
320 pentacenequinone acts as an energetically inert impurity, similar to the example included in  
321 Figure 4c, but its presence lowers the charge carrier mobilities by locally distorting the lattice.<sup>84</sup>  
322 Reduction of the impurity content by a factor of five lead to two orders of magnitude lower trap  
323 density, and mobilities as high as  $35 \text{ cm}^2 \text{ V}^{-1} \text{ s}^{-1}$ . Environmental contaminants such as moisture  
324 ( $\text{H}_2\text{O}$ ) and  $\text{O}_2$  can also create discrete trap states. The high electron affinity of  $\text{O}_2$  gas molecules  
325 make them potential traps for electrons.<sup>85</sup> Isolated  $\text{H}_2\text{O}$  and  $\text{O}_2$  gas molecules cannot trap holes as  
326 their gaseous phase ionization energies are too high ( $\sim 12 \text{ eV}$ ).<sup>86</sup> However, clusters of water  
327 molecules have significantly lower ionization energies due to stabilization of charge from the

328 dipole moment of surrounding molecules and hence can form potential traps for holes.<sup>86,87</sup>

329 Examples of such traps will be discussed in section 3.3.

330 Dopants are often added to OSCs to enhance their conductivity. The doping efficiency is  
331 governed by several factors such as the offset of energy levels between the host and the guest and  
332 the dopant concentration. The mechanism of charge transport in doped OSCs is complex and is  
333 dominated by several competing processes that depend on the above factors. For example, the  
334 addition of a dopant can either broaden the DOS of the host thereby introducing tail states, or the  
335 dopant-induced charge carriers can fill up existent trap states to neutralize them or the presence of  
336 the dopant can annihilate the trap states.<sup>88-91</sup> For a detailed description of doping in OSCs and  
337 different types of doping such as molecular and metallic doping, we recommend the review by  
338 Lüssem et al.<sup>92</sup>

339

## 340 **3.2. Interfacial effects**

341 Organic electronic devices consist of consecutive layers of dissimilar electronic materials  
342 and their architecture has different complexity levels depending on the function that they  
343 perform. The phenomena occurring at interfaces between any two distinct layers, such as  
344 electrode/semiconductor, semiconductor/dielectric and interface with other organic layers, add to  
345 the charge carrier trapping discussed in Section 3.1, which focused on the processes occurring in  
346 the bulk of the OSC. Trapping at interfaces has a profound impact on device performance, as we  
347 will describe in this section.

348

### 349 **3.2.1. Traps at semiconductor/dielectric interface**

350 In OFETs the transistor channel forms in the vicinity of the gate dielectric and the  
351 presence of charge carrier traps at the interface between the OSC and dielectric can impact the  
352 performance of such devices.<sup>10</sup> For example, in addition to scattering of the accumulated  
353 charges due to non-uniform topology,<sup>93,94</sup> surface energy and chemistry, the roughness of the  
354 dielectric layer alters the molecular ordering of the OSC deposited on top, which results in  
355 structural defects such as dislocations. Chua et al. investigated the effect of interface roughness  
356 on the charge carrier mobility in OFETs and found that for small values the mobility did not vary  
357 significantly, but above a critical roughness of 0.7 nm, it decreased by several orders of  
358 magnitude.<sup>95</sup>

359 Another route for trap generation at the semiconductor/dielectric interface is related to the  
360 adsorption of impurities such as water, oxygen or hydroxyl groups. The passivation of dangling  
361 bonds at the surface of the SiO<sub>2</sub> gate-dielectric by adsorption of hydroxyl groups results in a high  
362 density of silanol groups at the surface that can trap electrons. This has been the main challenge  
363 in achieving electron transport in SiO<sub>2</sub>-based transistors.<sup>93,96</sup> The application of self-assembled  
364 monolayers (SAMs) such as hexamethyldisilazane (HMDS), octadecyltrichlorosilane (OTS),  
365 and decyltrichlorosilane (DTS) has proven to passivate some, (but not all) of the surface traps in  
366 SiO<sub>2</sub> to yield functional n-channel OFETs.<sup>96</sup> Stable operation of the devices was realized with  
367 the use of polyethylene as a dielectric buffer layer.<sup>96</sup> Fluorinated polymer dielectrics such as  
368 Cytop and poly[4,5-difluoro-2,2-bis(trifluoromethyl)-1,3-dioxole-co-tetrafluoroethylene]  
369 (AF2400) allow for a significantly lower interfacial trap density compared to SiO<sub>2</sub>.<sup>97,98</sup> Also, the  
370 fluorine group renders them hydrophobic and hence they can repel water molecules,<sup>99,100</sup> and  
371 when used as top gate dielectrics, they also act as encapsulants.

372           The effect of the gate dielectric type on the performance of pentacene thin film transistors  
373 has been investigated by Knipp et al.<sup>101</sup> The transfer characteristics was modelled by a trap DOS  
374 consisting of two exponential distributions of deep acceptor-like states and donor-like shallow  
375 states,<sup>20</sup> with the former accounting for the onset of drain current while the latter accounts for a  
376 non-zero threshold voltage. The nature of the dielectric affected film microstructures which, in  
377 turn, determined the density and the depth of the trap DOS. For example, films on  
378 benzocyclobutane (BCB) consisted of smaller grains than those on SiO<sub>2</sub> and yielded a more  
379 negative threshold voltage due to a broader distribution of donor-like shallow trap states, with  
380 the width increasing from 45 meV on SiO<sub>2</sub> to 90 meV on BCB. Modification of film  
381 microstructure has also been achieved by treatment of the substrate with SAMs, leading to lower  
382 trap densities and therefore high charge carrier mobilities.<sup>102</sup> SAMs such as OTS and  
383 octadecyltrichlorosilane (ODTS) provide a low-surface energy, which typically yields a better  
384 film morphology, but they are challenging to implement in solution-deposited devices.<sup>103,104</sup>

385           Mei et al. discovered that the mismatch in the coefficient of thermal expansion (CTE) of  
386 consecutive device layers induces strain at the interfaces, which results in generation of localized  
387 trapping states.<sup>105</sup> They found a crossover from a band-like transport to a temperature activated-  
388 transport upon increasing the interfacial thermal expansion mismatch, which could not be  
389 explained by polaronic effects alone,<sup>106–108</sup> and was assigned to charge trapping due to thermal  
390 strain.

391           The above effects arising at the semiconductor/dielectric interface vanish in the case of a  
392 transistor with a vacuum-gap dielectric, as demonstrated by Sundar et al. and Menard et al. using  
393 polydimethylsiloxane (PDMS) stamps as substrates.<sup>109,110</sup> However, the CTE mismatch between  
394 the PDMS substrate and the OSC can introduce microstrain in the crystal, which in turn modifies

395 its work function.<sup>111</sup> Such modifications can potentially create band tail states induced by  
396 electrostatic disorder.

397

### 398 **3.2.2. Metal/semiconductor interface**

399 Charge carrier trapping can also occur at the interface between device electrodes and  
400 OSCs, thus affecting charge carrier injection and collection. The localized states present in the  
401 band gap of an OSC can alter the mechanism of charge carrier injection from the metal into the  
402 OSC, resulting in an increased injection barrier that manifest itself as high contact resistance in  
403 electronic devices. Such states can be intrinsic to the OSC, or can be introduced by the metal.<sup>112</sup>  
404 The energetic disorder inherent in most OSCs causes some of the in-band electronic states to tail  
405 into the bandgap,<sup>113</sup> which can pin the Fermi level of the metal and prevent it from reaching the  
406 band edges resulting in non-vanishing injection barriers. The extent of disorder determines the  
407 distance from the band edge to the pinned Fermi-level. Insertion of a buffer layer, such as a thin  
408 oxide metal layer, between the metal and the OSC, can unpin the Fermi-level decreasing the  
409 injection barrier.<sup>114</sup> On the other hand, these gap states can also act as energy ladders for charge  
410 carriers to hop between these states and reach the transport energy level in OSCs.<sup>114,115</sup> For  
411 details about charge injection and contact resistance, we recommend the recent reviews by  
412 Waldrip et al.,<sup>116</sup> Caironi et al.,<sup>117</sup> and Noh et al.<sup>114</sup>

413 The surfaces of organic crystals are prone to contamination and defects and when a metal  
414 comes in contact with such a surface, localized states are induced at the interface between the  
415 two materials. These states introduce a surface potential which can subsequently increase the  
416 injection barrier. Baessler and Vaubel detected surface states in anthracene single crystals by

417 measuring the threshold energies of photoemission of charge carriers from a variety of metals  
418 into the crystal.<sup>118</sup> They found that high work function metals such as Mg and Pb did not affect  
419 the interface, while a surface potential was generated for low work function electrodes such as  
420 Ca, Na, Cs and Ba due to electron trapping. A surface trap density of  $2 \times 10^{12} \text{ cm}^{-2} \text{ eV}^{-1}$ , with a  
421 maximum trap depth of  $1.3 \pm 0.2 \text{ eV}$  was evaluated. de Boer and Morpurgo investigated this  
422 effect by comparing the results of space charge limited current (SCLC) measurements performed  
423 on tetracene single crystals in a sandwich structure, with the crystal laminated on a pre-fabricated  
424 Au contact (bottom contact), and the top Au contact deposited by electron-beam evaporation.<sup>119</sup>  
425 In spite of the nominally identical electrode/OSC interfaces, they found that the injection was  
426 more efficient from the surface of the bottom contact. They concluded that the e-beam  
427 evaporation process damages the crystal surface due to interaction with X-rays and high energy  
428 electrons during the deposition process, resulting in a larger density of traps compared to the  
429 pristine bottom surface. The trap density at the crystal surface was also larger than that in the  
430 bulk, highlighting the effect of processing on the surface traps and, consequently, charge  
431 transport. This effect was further explored by Coll et al. and they developed a non-destructive  
432 deposition method for top contacts, i.e., flip-chip lamination.<sup>120</sup> The technique was based on  
433 nano-transfer printing and involved the adhesion of ultra-smooth patterned contacts onto the  
434 organic crystal. This resulted in similar SCLC currents from both top and bottom electrodes  
435 confirming that flip-chip lamination preserves the crystal quality.

436

### 437 **3.3. Environmental effects**

438 Exposure to environment either during device fabrication, handling and/or  
439 characterization, often affects the quality of the OSC and can lead to trap formation.  
440 Temperature, moisture ( $\text{H}_2\text{O}$ ), ambient gases ( $\text{O}_2$ ) and electromagnetic radiation such as light and  
441 X-rays are some other possible sources of traps. Recent developments have led to very stable  
442 organic electronic devices, a milestone which has been realized through careful device and  
443 material design.<sup>121–124</sup>

444 Traps related to temperature manifest themselves in OFETs as shifts in turn-on voltage  
445  $V_{on}$ , subthreshold slope  $S$  and threshold voltage  $V_{th}$ .<sup>125,126</sup> The borderline between shallow and  
446 deep traps changes with temperature. i.e., at sufficiently high temperatures all traps behave as  
447 shallow traps and vice versa. Ambient moisture in pentacene films have been known to cause  
448 OFET device degradation, resulting in larger  $V_{th}$ ,  $S$ , and high on-currents.<sup>127–130</sup> Water molecules  
449 can either act as traps for charge carriers or cause redox reactions in the OSC.<sup>131</sup> Using first-  
450 principle calculations, it was predicted that water-related defects are energetically favorable in  
451 pentacene and hence are more likely to occur.<sup>132</sup> Such traps have led to bias stress instabilities in  
452 OFETs.<sup>124,133–135</sup> In pentacene single crystal transistors a discrete trap state with density up to  
453  $10^{12} \text{ cm}^{-2}$  was generated during negative bias stress as a result of water adsorbed on the  $\text{SiO}_2$   
454 dielectric.<sup>134</sup> Gomes et al. investigated this effect as a function of temperature and discovered  
455 that bias-stress effects are only present above 200 K, which corresponds to a known phase  
456 transition of supercooled water.<sup>135</sup> This was observed in several OSCs independent of deposition  
457 techniques. Bias stress effects due to water adsorbed by the dielectric can be minimized by  
458 rendering the dielectric hydrophobic either by using fluorinated polymers as dielectric,<sup>136</sup> by the  
459 application of SAMs,<sup>134</sup> by inserting interlayers between the dielectric and OSC,<sup>133</sup> or by  
460 encapsulating the devices.<sup>137</sup> Water-related traps in conjugated polymers has recently gained a

461 lot of attention.<sup>87,124,138</sup> Blom and coworkers, found that hydrated oxygen complexes form  
462 electron traps in polymeric electron-only diodes: transport is limited by traps exhibiting a  
463 Gaussian distribution centered at ca. 3.6 eV from the vacuum level with a density of  $3 \times 10^{23} \text{ m}^{-3}$   
464 and a width of  $\sim 0.1 \text{ eV}$ .<sup>138</sup> Zuo et al. used a similar approach to show that electron and hole traps  
465 created in hole-only and electron-only devices made of several OSCs were a result of water  
466 molecules enclosed in nanoscopic voids in the films.<sup>87</sup> A peak was observed in the slope of the  
467 logarithmic current-voltage curve plotted as a function of voltage, which was assigned to a  
468 transition from trap-limited to trap-filled charge transport regime. By modeling the curves using  
469 a 1-D drift-diffusion model, hole and electron trap distributions were determined to be  
470 consistently centered around 0.3-0.4 eV from the HOMO and LUMO levels respectively, for all  
471 materials. Solvent-vapor annealing in a saturated *o*-xylene environment removed majority of  
472 water in the nanovoids through molecular rearrangements, resulting in suppression of the  
473 trapping peak. The study has recently been expanded to include small molecules, proposing a  
474 universal design rule to achieve trap-free bipolar transport in organic devices.<sup>86</sup> Recently,  
475 Nikolka et al. investigated bias stress effects in conjugated polymers due to the existence of  
476 water molecules in the voids of the polymer films that act as charge carrier traps.<sup>124</sup> They showed  
477 that incorporation of solvent additives or dopants displaces the water molecules and enhances the  
478 operational stability of the device.

479 Various types of oxygen-related traps in pentacene have been studied theoretically and  
480 experimentally.<sup>48,132,139,140</sup> Northrup et al. predicted that trap states form when an H-atom is  
481 replaced with an O-atom that forms a double bond with the C-atom.<sup>139</sup> Another possible defect,  
482 where an O-atom bridges two C-atoms of neighboring pentacene molecules, was predicted to  
483 generate trap states with energies in the range 0.33-0.4 eV above the valence band edge.<sup>132</sup>

484 Batlogg and coworkers studied the effect of oxygen on the trap DOS spectrum of pentacene thin-  
485 film transistors and found that a broad peak centered at 0.28 eV from the valence band edge,  
486 with a total volume density  $\sim 10^{18} \text{ cm}^{-3}$ , was created. A similar peak was observed by Knipp et al.  
487 in pentacene films exposed to oxygen under a continuous bias stress.<sup>140</sup> Density functional  
488 theory calculations suggested the formation of an oxygen-pentacene complex, which then creates  
489 a C-O bond with a neighboring pentacene molecule. The formation of the complex is facilitated  
490 by the applied gate-bias under oxygen exposure. Discrete trap states induced upon  $\text{O}_2$  exposure  
491 have also been observed in rubrene single crystals using temperature-dependent SCLC  
492 measurements, where a hole trapping state was resolved at 0.27 eV above the valence band  
493 edge.<sup>48</sup>

494 OSCs are inevitably exposed to ionization radiation such as X-rays during structural  
495 characterization, or even during operation. Several studies involving intentional exposure of  
496 ionizing radiation to elucidate its effect on device metrics and the DOS spectrum have been  
497 reported. Exposure of rubrene single crystals to X-rays caused shifts in  $V_{th}$  of the OFETs, but  
498 surprisingly the mobilities remained unharmed, suggesting that the generated traps are located  
499 deep in the bandgap.<sup>126</sup> Rubrene crystals have also been exposed to  $\text{He}^+$  ions and their effect on  
500 the trap DOS was studied using temperature-dependent SCLC measurements.<sup>141</sup> A discrete peak  
501 at 0.35 eV from the HOMO edge was resolved with trap densities ( $\sim 10^{16} \text{ cm}^{-3}$ ) initially  
502 increasing with radiation dosage and saturating at higher dosages. The formation of the trap was  
503 attributed to C-H bond breaking and hydrogen loss.

504

#### 505 **4. Effect of charge carrier traps on electronic devices**

506 The presence of traps in OSCs has a profound impact the performance of electronic  
507 devices. In this section, we briefly discuss such effects in OFETs, OLEDs and OPV devices. In  
508 OLEDs, electrons and holes emitted from opposite sides of the OSC recombine radiatively to  
509 emit light and traps can cause non-radiative recombination, thus reducing the efficiency of the  
510 devices.<sup>6,142,143</sup> In addition to reducing the charge carrier mobilities, which also results in low  
511 efficiency, the presence of traps can cause device degradation.<sup>144,145</sup> OPVs are based on organic-  
512 organic heterojunctions where electron-hole pairs (excitons) are generated from two different  
513 OSCs upon absorption of light. The excitons dissociate into free carriers at the heterojunction  
514 and are carried out separately to the external circuit. Traps can cause non-radiative Shockley-  
515 Read-Hall recombination of the dissociated charge carriers, decreasing the quantum efficiency of  
516 the devices.<sup>146,147</sup> Traps also alter the energy level alignment at the organic-organic  
517 heterojunction.<sup>148-150</sup> In addition to impacting the fill factor, the misalignment between the  
518 energy levels will directly influence the maximum achievable open-circuit voltage.<sup>149</sup> On the  
519 other hand, traps can assist with the dissociation of excitons into free carriers.<sup>151</sup> The excitons are  
520 bound together by high Coulomb energy which acts as an energy barrier for dissociation. The  
521 electrons and holes can dissociate down to lower energy states formed by traps and finally  
522 overcome the barrier, thereby increasing the efficiency of the devices.

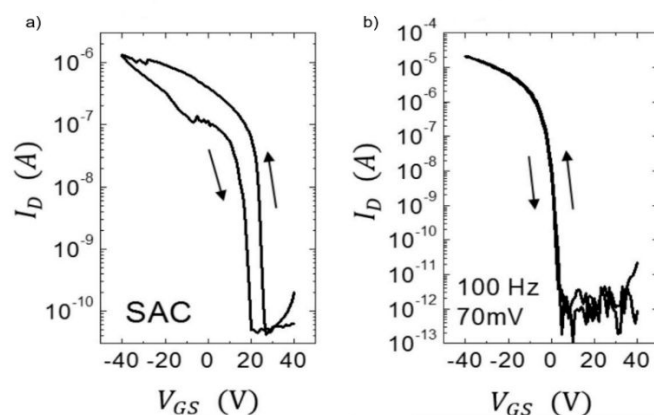
523 OFET technology holds great promise to realizing applications such as active matrix  
524 OLEDs, radio frequency identification (RFID) tags, electronic paper and sensor arrays. In  
525 addition, they offer a versatile platform for charge transport studies under different charge  
526 density regimes and an experimental tool for unambiguous determination of charge carrier  
527 mobilities. An important parameter that defines the electrical performance of OFETs is the

528 mobility of the charge carriers in the transistor channel,  $\mu$ , which represents the average speed at  
529 which the carriers move in the presence of an electric field. Trapped charge carriers reduce the  
530 effective mobility, with the density of traps and trapping timescale defining the macroscopic  
531 transport. In the presence of traps, the mobility is gate-voltage dependent.<sup>31,152,153</sup> At low gate-  
532 source voltages, the injected/accumulated charges occupy the available trap states and the drain  
533 current is the result of charge transport occurring through thermally-activated hopping/tunneling  
534 between these states. As the gate-voltage increases, the trap states are gradually filled, and at  
535 sufficiently large voltages all states are filled and the charge carriers can finally occupy the  
536 extended states and subsequently increase the mobilities. The gate-source voltage required to fill  
537 trapping states before charge accumulation is possible in the transistor channel is called the  
538 threshold voltage and hence a non-zero threshold voltage is indicative of the presence of traps.<sup>152</sup>  
539 In fact, the value of the threshold voltage provides direct access to the density of traps, as will be  
540 described in section 6.1.2. However, other effects such as contact resistance and the gate-bias  
541 dependent charge carrier concentration in the channel, can also contribute to gate-voltage  
542 dependent mobilities.<sup>102,153–156</sup> The presence of traps and contact resistance are competing effects  
543 that obscure device characteristics and it is often difficult to distinguish the effect of one from the  
544 other. Bittle et al. studied the effect of molecular ordering in regioregular poly(3-hexylthiophene)  
545 (RR P3HT) films on OFET characteristics.<sup>156</sup> A reduction in contact resistance and a shift to  
546 field-independent mobilities occurred as a result of narrowing of the density of localized states  
547 near the band edge in films with increased crystalline order. Traps can also be manifested in the  
548 subthreshold region of the transfer characteristics, where the gate-source voltage is below the  
549 threshold voltage and the drain current has an exponential dependency on the gate voltage.<sup>4</sup>  
550 Thermal de-trapping of charge carriers from shallow traps can contribute to high off currents,

551 resulting in a less steep subthreshold region and a high subthreshold swing,  $S$ .<sup>157</sup> Practical  
552 applications require very steep subthreshold swing for fast switching of devices with a  
553 theoretical limit of 60 meV at room temperature.<sup>4</sup> Another salient feature in practical OFETs,  
554 resulting from the existence of traps, is the bias stress effect, i.e. the change in the threshold  
555 voltage or turn-on voltage due to the application of either a continuous or dynamic gate-source  
556 voltage. The shift in the threshold voltage over time caused by bias stress is often modeled using  
557 a stretched exponential function.<sup>158</sup> The effect is attributed to several mechanisms and charge  
558 carrier trapping within the bulk of the semiconductor, in the dielectric or at the  
559 semiconductor/dielectric interface are some of them.<sup>159</sup> The presence of water molecules in the  
560 semiconductor or the dielectric has also been proven to cause bias stress.<sup>133,135</sup> Gate-bias stress  
561 effect is typically reversible, meaning the trapped charges can be released back into the extended  
562 states upon removal of the applied bias. The carrier trapping and release processes depend on  
563 several factors such as the materials employed, biasing conditions, device processing and  
564 temperature.<sup>160</sup> Illuminating with bandgap radiation reversed bias stress effects caused by hole  
565 trapping in polyfluorene thin film transistors.<sup>161</sup> Zschieschang et al. showed that applying a  
566 drain-source voltage during the bias stress can decrease the shift in threshold voltage by creating  
567 a pathway for the trapped charge carriers.<sup>158</sup> Kippelen and coworkers have demonstrated OFETs  
568 with remarkable bias stress stability using ultrathin bilayer gate dielectrics comprising of Cytop  
569 and  $\text{Al}_2\text{O}_3$ .<sup>122,123,162</sup> The best devices yielded threshold voltage shifts below 0.2 V during  
570 continuous gate bias stress at  $V_{GS} = -10$  V in the saturation regime ( $V_{DS} = -10$  V) for 40 hours and  
571 in the linear regime ( $V_{DS} = -2$  V) for 100 hours.<sup>123</sup>

572 Hysteresis in the current-voltage characteristics is another clear indication of the  
573 existence of traps. Charge carriers trapped in the semiconductor or at the

574 semiconductor/dielectric interface during the forward voltage sweep get released during the  
575 reverse voltage sweep and contribute to differential current. Figure 6 shows hysteresis observed  
576 in the drain current  $I_D$  vs gate-source voltage  $V_{GS}$  curves of an OFET based on diF-TES ADT  
577 films processed using two different crystallization techniques.<sup>75</sup> Films grown from solvent-  
578 assisted crystallization (SAC) are characterized by severe hysteresis (Figure 6a) compared to  
579 those grown from vibration-assisted crystallization (VAC) (Figure 6b), due to the presence of a  
580 higher density of traps at the semiconductor/dielectric interface. The vibrations applied during  
581 solvent evaporation provided additional energy to the system to crystallize in the global potential  
582 energy minimum, with superior crystalline order. Moisture related trap states also contribute to  
583 device hysteresis.<sup>163,164</sup> Noh et al. showed that hysteresis in a pentacene OFET with poly(4-  
584 vinylphenol) (PVP) dielectric caused by moisture adsorption in the polar dielectric could be  
585 eliminated by thermal annealing the device in vacuum at 120 C.<sup>164</sup> In addition, slow relaxation of  
586 the gate dielectric and charge storage in the gate dielectric are also attributed to hysteresis and  
587 therefore the effect has been exploited for memory applications which require storage of  
588 charge.<sup>165</sup>



589  
590 *Figure 6. Hysteresis in  $I_D$  vs  $V_{GS}$  curves for OFETs based on diF-TES ADT films processed from*  
591 *a) SAC and b) VAC. Adapted with permission from ref.<sup>75</sup> Copyright 2013, Wiley-VCH.*

592

593 **5. Impact of traps on charge transport mechanisms**

594 The temperature-dependence of charge carrier mobility provides insights into the  
595 mechanism of charge transport in a material. An increase in mobility upon cooling (i.e.,  $\mu \propto T^{-n}$   
596 ,  $0 < n < 3$ ) is typically observed in high quality OSC single crystals with low trap densities  
597 and was attributed to band-like transport.<sup>16,106,109,110,166–168</sup> The presence of traps (density and  
598 distribution, both energetic and spatial) alter the charge transport mechanism significantly, and  
599 therefore the dependence of  $\mu$  on  $T$ . As the trap densities increase, a transition from band-like to  
600 thermally-activated hopping regime can occur,<sup>126,169</sup> where charge carriers assume band-like  
601 motion close to room temperature and are immobilized in the shallow trapping states at low  
602 temperatures, see for example the black curve in Figure 5a obtained in rubrene single crystal  
603 OFETs.<sup>170</sup> The temperature activated transport at low temperatures was modelled by an  
604 Arrhenius relation,  $\mu \approx e^{-\frac{E_a}{kT}}$ , where  $E_a$  is the activation energy. The mobilities determined from  
605 Hall-effect measurements on the same crystal, however, increased with decreasing temperature  
606 in both the high and low temperature regimes (blue curve of Figure 5a).<sup>170</sup> Hall mobilities  
607 describe the motion of free charge carriers, since trapped charges do not respond to the Lorentz  
608 force. Therefore, Hall measurements are indicative of intrinsic transport, where charge carriers  
609 move in delocalized bands in between trapping events. Figure 5b shows  $\mu$  vs  $T$  plots for a  
610 solution processed 6,13-bis(triisopropylsilylethynyl) pentacene (TIPS-pentacene) OFET with  
611 Cytop dielectric obtained at different drain-source voltages.<sup>171</sup> At low drain-voltages, the  
612 mobility exhibits an activated behavior over a wide temperature range, with a small activation  
613 energy of  $E_A = 5.7$  meV: in this regime the transport is dominated by shallow traps. At  
614 sufficiently high fields, the traps are filled, and as a result,  $\mu$  increases with decreasing  $T$ . As

615 mentioned in Section 3.2.1, the strain induced at the interface between the semiconductor and

616 dielectric due to the CTE mismatch between consecutive device layers can also introduce traps.

617 The example in Figure 5c shows thermally-activated transport for the case of FETs fabricated at

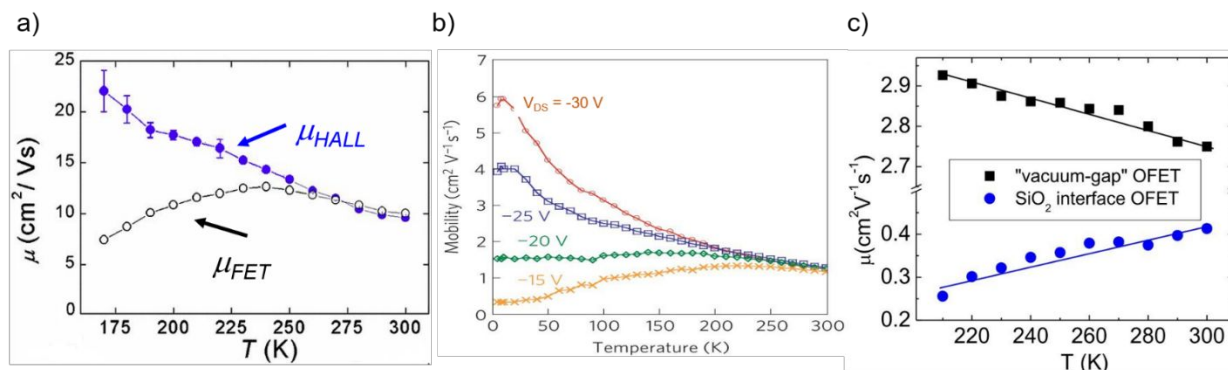


Figure 5.  $\mu$  vs  $T$  plots for a) rubrene single crystals, Adapted with permission from ref,<sup>170</sup>

Copyright 2005, American Physical Society, b) TIPS-pentacene thin films at different drain-

source voltages, Adapted with permission from ref,<sup>171</sup> Copyright 2010, Springer Nature Ltd, and

c) diF-TEG ADT crystals with  $\text{SiO}_2$  dielectric (blue circles) and vacuum dielectric (black

circles). Adapted from ref,<sup>105</sup> Copyright 2017, National Academy of Sciences.

618 the interface between 2,8-difluoro-5,11-bis(triethylgermylethynyl) anthradithiophene (diF-TEG  
 619 ADT) ( $\text{CTE} = 162 \text{ ppm K}^{-1}$ ) and  $\text{SiO}_2$  dielectric ( $\text{CTE} = 4.1 \text{ ppm K}^{-1}$ ) (blue circles).<sup>105</sup> FETs  
 620 fabricated on similar crystals, but with vacuum dielectric, where thermal strain is absent,  
 621 exhibited band-like transport (black squares). Investigation of a large number of  
 622 semiconductor/dielectric combinations confirmed that the result cannot be explained simply on  
 623 the basis of Frölich polarons, and the microstrain plays a critical role. Laudari and Guha  
 624 investigated charge transport in TIPS pentacene FETs with ferroelectric polymer dielectrics.<sup>172</sup>  
 625 While the reference FETs consisting of non-ferroelectric dielectric ( $\text{SiO}_2$ ) showed activated  
 626 transport, a band-like temperature dependence of the mobility was observed within the  
 627 ferroelectric temperature window in devices with poly(vinylidene fluoride-trifluoroethylene)  
 628 (PVDF-TrFE) dielectric due to de-trapping of charge carriers from shallow traps arising from  
 629 changes in the electric polarization of the dielectric. Merlo and Frisbie observed two distinct

630 thermally-activated transport regimes in FETs based on RR P3HT nanofibers due to the presence  
631 of a double distribution of traps.<sup>125</sup> The high activation energy in the high-temperature regime  
632 was attributed to the presence of deep donor-like traps, while the low-temperature regime  
633 exhibited a low activation energy resulting from acceptor-like shallow traps. A transition  
634 between the two regimes was observed, with the transition temperature depending on the gate  
635 voltage (195 K for  $V_{GS} = -12$  V and 250 K for  $V_{GS} = -32$  V). At larger gate voltages, since all  
636 deep traps are filled, the distinction between the two regions disappeared and only the effect of  
637 shallow traps was manifested in the Arrhenius plot. Nelson et al, observed both a temperature-  
638 independent mobility, and an activated charge transport in thin-film pentacene OFETs depending  
639 on the quality of the films (i.e. trap densities).<sup>173</sup> A similar trend was found in solution deposited  
640 OSCs, where the activation energy was proportional to the trap densities.<sup>102</sup>

## 641 **6. Experimental techniques to detect and characterize traps**

642 Determining the origin, concentration and composition of charge carrier traps in OSCs, as  
643 well as their spatial and energetic distribution, is not trivial and remains a challenge, in spite of  
644 the tremendous efforts dedicated on this topic. Nevertheless, progress has been remarkable and  
645 access to the density of trap states spectra has led to significant improvements over the years in  
646 device performance and reliability. Several experimental techniques have been developed to  
647 access traps, but since each of them includes different levels of approximations, have varying  
648 sensitivities, and cover different ranges of energy distributions, the results are not always  
649 consistent. This section aims to cover the most popular experimental techniques employed in the  
650 detection and characterization of traps. The benefits and limitations of each technique, along  
651 with a few examples where they have been adopted will be outlined.

652

## 653        **6.1. Electrical Measurements**

### 654            **6.1.1. Space-charge limited current (SCLC) measurements**

655            SCLC measurements are based on the concept of unipolar injection of charge carriers  
 656 from an ohmic contact into the bulk of the semiconductor. Here we will discuss this technique in  
 657 the context of trap densities and energy spectra. When a high density of charge carriers is  
 658 injected from a contact into the semiconductor, a space charge region is formed within the  
 659 semiconductor, which subsequently alters the flow of charge carriers. The presence of traps  
 660 influences the current flow, hence measurements of the current density,  $J$ , as a function of the  
 661 applied voltage  $J = f(V)$ , provide insights into the localized trapping states. The experimental set  
 662 up for SCLC measurements is simple and involves sandwiching of a semiconductor in between  
 663 two electrodes in a parallel plate geometry. The simplified phenomenological SCLC theory is  
 664 based on an idealized model which assumes ohmic contacts and diffusion-free currents from  
 665 unipolar charge carriers for a single discrete distribution of shallow traps. The current-voltage  
 666 relation is given by,<sup>35</sup>

$$J_{SCLC} = \frac{9\mu\varepsilon_s\varepsilon_0\theta}{8L^3}V^2 \quad (3)$$

667 where  $\mu$  is the charge carrier drift mobility,  $\varepsilon_s$  is the relative permittivity of the semiconductor,  
 668  $\varepsilon_0$ , the permittivity of free space,  $L$  is the spacing between the electrodes, and  $\theta$ , the ratio of free  
 669 charge carriers ( $n_{free}$ ) to total charge carriers ( $n_{total}$ ) defined by:

$$\theta = \frac{n_{free}}{n_{total}} = \frac{N}{N_t} \exp\left(\frac{E_t}{kT}\right) \quad (4)$$

670 Here  $N_t$  is the total trap density,  $N$  is density of transport sites available for conduction (for  
 671 electron only and hole only transport,  $N$  is the effective density of states in the conduction band

672 ( $N_C$ ) and valence band ( $N_V$ ), respectively), and  $E_t$  is the energy of the shallow trap with respect to  
673 the band edge.  $\theta \leq 1$  and is independent of the applied voltage. When  $\theta = 1$ , Equation 4 reduces to  
674 the Mott-Gurney law for trap-free insulators, referred to as Child's law for solid-state.

675 Figure 6a illustrates a SCLC current-voltage curve for the case of a discrete shallow

676 trapping state. The graph is characterized by the Ohmic region at low voltages, where the current

677 increases linearly with voltage, then the SCLC regime at intermediate bias, followed by the

678 SCLC trap-free regime at high voltages. The current in the latter two regimes follow a quadratic

679 dependency on the applied voltage. The equations governing the current in each region are

680 provided as inset.<sup>174</sup> For a semiconductor with traps, a fraction of the injected charges will not

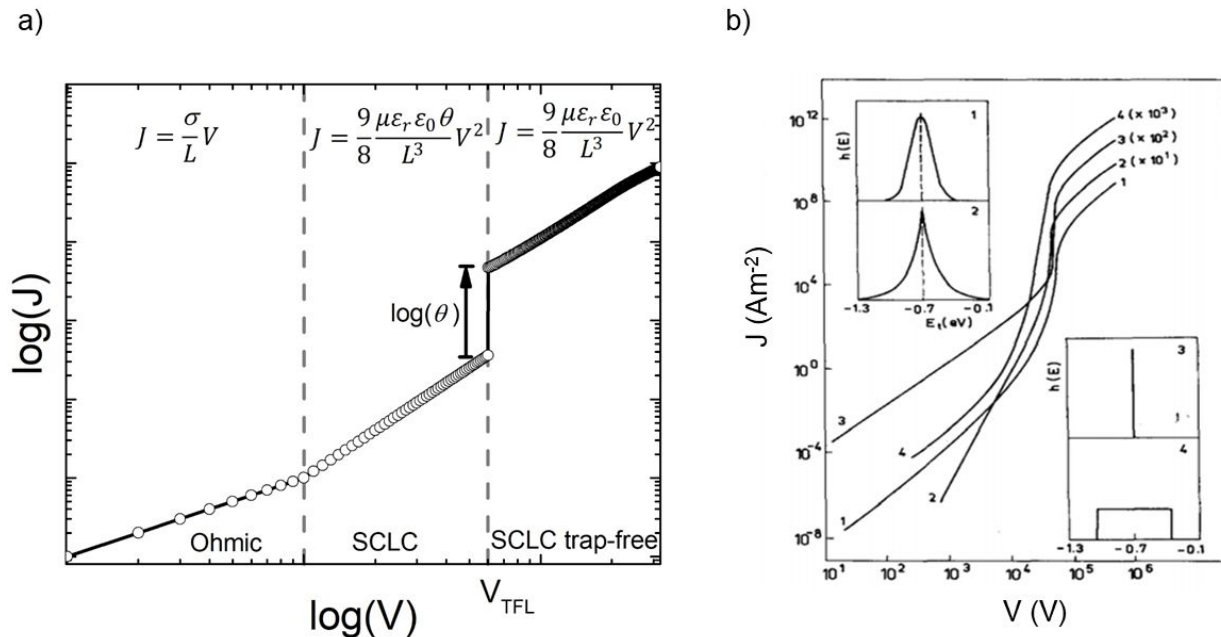


Figure 6. a) Typical current-voltage characteristics from SCLC measurements for a discrete distribution of shallow traps characterized by the Ohmic, SCLC and SCLC trap-free regimes. Inset presents the equations governing  $J$  and  $V$  in the respective regimes. b) Calculated current-voltage characteristics for various distributions of trapping states as shown in the insets 1. Gaussian distribution, 2. double exponential distribution, 3. discrete distribution and 4. uniform distribution, all centered at 0.7 eV from the valence band edge. Adapted with permission from reference <sup>182</sup>. Copyright 1990, Elsevier Ltd.

681 participate in transport because they are captured by the traps. This results in a reduction in  
 682 current by a factor of  $\theta$ . Assuming one dominant trap state, at higher voltages, an abrupt  
 683 transition from the space charge limited regime to the trap filled limit occurs when the quasi-  
 684 Fermi level crosses the discrete trap level. This process is evident in the  $J$ - $V$  curves as a sudden  
 685 increase in the current at a voltage called the trap-filled limit voltage ( $V_{TFL}$ ) which is used to  
 686 estimate  $N_t$  (per unit volume per unit energy):

$$N_t = \frac{\epsilon_r \epsilon_0}{eL^2} V_{TFL} \quad (5)$$

687 At voltages higher than  $V_{TFL}$ , all traps are filled and the semiconductor is trap-free. The current  
 688 after this point follows the Mott-Gurney law for a trap-free insulator. SCLC measurements have  
 689 been used to estimate  $N_t$  in single crystals such as rubrene ( $N_t \sim 10^{15} \text{ cm}^{-3}$ ),<sup>175</sup> pentacene ( $N_t \sim 10^{11}$   
 690  $\text{cm}^{-3}$ ),<sup>84</sup> tetracene ( $N_t \sim 5 \times 10^{13} \text{ cm}^{-3}$ ),<sup>176</sup> and hydroxycyanobenzene ( $N_t \sim 10^{13} \text{ cm}^{-3}$ ).<sup>177</sup>

691 For the case of multiple discrete trap states, the  $J$ - $V$  curves exhibits several sharp  
 692 increases in the current as the quasi-Fermi level crosses through each trap state. Reaching the  
 693 trap-free limit is experimentally difficult, especially when the trap states are broadly distributed  
 694 in energy, as it is the case in most OSCs. The oversimplified assumption of a single discrete  
 695 distribution of shallow traps may be justified for ultra-pure single crystals, which are known to  
 696 have very low density of traps, but it is not accurate for polycrystalline films. Further, the  
 697 difficulty in interpreting the experimental  $J$ - $V$  curves as they deviate from the  $J \propto V^2$  dependency  
 698 to other forms such as  $J \propto V^n$  with  $n > 2$  required that other types of distribution functions  
 699 representing a quasi-continuous energy distribution of traps states be considered. A typical  
 700 distribution is an exponential distribution of traps of the form:<sup>178</sup>

$$N(E_t) = \frac{N_t}{kT_c} \exp\left(-\frac{E_t}{kT_c}\right) \quad (6)$$

701 where  $T_c$  is the characteristic temperature of the exponential trap DOS. The  $J$ - $V$  relation for such  
 702 a distribution follows,<sup>178,179</sup>

$$J_{SCLC} = Ne\mu \left( \frac{\epsilon_s \epsilon_0}{eN_t \exp\left(\frac{T_c}{T}\right)} \right)^m \left( \frac{m}{m+1} \right)^m \left( \frac{2m+1}{m+1} \right)^{m+1} \frac{V^{m+1}}{L^{2m+1}} \quad (7)$$

703 where  $m=T_c/T$  and is related to the width of the distribution. Typically, it is assumed that  $T_c > T$ ,  
704 which implies  $m>1$ . For  $T_c<T$ , this expression reduces to the case of shallow traps (Equation 3)  
705 with  $m=1$ . Comparing equations 3 and 7, it can be deduced that the SCLC current in a trap-  
706 limited semiconductor scales as  $N/(N_t)^m$ . Therefore, for  $m>1$ , by simultaneously reducing  $N$  and  
707  $N_t$ , it is possible to reduce trapping effects by a great extent. Indeed, Blom and coworkers  
708 adopted a method called trap dilution through blending the polymers with a high-bandgap  
709 semiconductor<sup>76,180</sup> and eliminated the dominant electron trapping in conjugated polymer blends  
710 with 10% active semiconductor and 90% high-bandgap host.<sup>180</sup> This led to the fabrication of  
711 OLEDs with balanced electron and hole transport and reduced non-radiative trap-assisted  
712 recombination, resulting in a doubling of efficiency at a ten-fold reduction in material costs.

713         While an exponential distribution explains  $n>2$  exponent values, with  $n$  being a constant,  
714 it cannot resolve curves with  $n$  monotonously increasing with applied voltage.<sup>178,181</sup> Other types  
715 of energy distributions have also been considered for the analysis of the  $J$ - $V$  curves. The  
716 Gaussian distribution function proposed by Silinsh is an example.<sup>33</sup> An S-shaped dependence  
717 observed in the logarithmic  $J$ - $V$  plot at voltages above  $V_{TFL}$  was attributed to Gaussian traps and  
718 in the case of several such distributions, a step-like  $J$ - $V$  characteristics is evident.<sup>33</sup> The analytical  
719 expression for  $J$ - $V$  relation varies with the applied voltage range as the quasi-Fermi level  
720 coincides with different regions of the Gaussian (for example, tail or peak), depending on the  
721 voltage applied. Therefore, different analytical expressions have been proposed for different  
722 voltage ranges and slopes  $n$ .<sup>33</sup> Figure 6b illustrates the  $J$ - $V$  curves predicted for several trap  
723 distributions such as Gaussian, exponential and uniform. An important outcome of assuming  
724 quasi-continuous distributions is that it allows the determination of the trap DOS as a function of  
725 energy in the band gap. Such a deduction however requires modelling experimental  $J$ - $V$  curves to

726 expressions analytically or numerically derived from theoretical models which requires *a priori*  
727 assumptions on the energetic profile of traps. Since experimental curves are often interpreted  
728 using integrating techniques involving asymptotic equations, details of the energetic distributions  
729 can be lost, leading to incorrect results.<sup>182</sup> Therefore, several efforts focused on developing  
730 methods for extraction of trap parameters from the experimental  $J$ - $V$  curves for an arbitrary  
731 distribution of trap i.e., without making an *a priori* assumption on the energetic distribution.  
732 Nespurek and Sworakowski developed the differential method which took the first derivatives of  
733 the experimental  $J$ - $V$  curves to extract trap parameters.<sup>183</sup> Later, Schauer et al put forward the  
734 thermally modulated SCLC method (TM-SCLC), also called temperature dependent SCLC (TD-  
735 SCLC), in which the energy of the trapping state is determined separately from the experimental  
736 activation energy,  $E_a$  of the conductivity  $\sigma$ , in addition to the differential evaluation of the  $J$ - $V$   
737 curves.<sup>183–185</sup> The  $J$ - $V$  curves are measured at different temperatures in order to determine  $E_a(V)$   
738 from the slope of the Arrhenius plot  $\ln \sigma$  Vs  $1/T$ . TD-SCLC measurements performed on high-  
739 purity single crystals of rubrene identified the presence of two exponential trap DOS: one with a  
740 steep distribution close to the band edge and another with a shallower distribution in the band  
741 gap.<sup>48</sup> The breadth of the distribution, as well as the trap densities, varied from sample to sample  
742 due to the fact that the crystals are sensitive to growth conditions and atmospheric contaminants.  
743 The purest sample yielded deep trap densities as low as  $10^{15} \text{ cm}^{-3}$ , while densities as high as  $10^{17}$   
744  $\text{cm}^{-3}$  were measured in other crystals. In addition, traps created by means of a controlled  
745 exposure to activated oxygen were detected as a discrete peak in the DOS spectra at 0.27 eV  
746 above the mobility edge. More recently, Nikolka et al., characterized water-related traps in the  
747 bulk of a polymer films using TD-SCLC.<sup>186</sup> The addition of small molecular species displaced

748 the water-induced traps to yield a narrow density of tail states (in the order of  $kT$ ) near the band  
749 edge akin to that of molecular single crystals.

750         Effects such as diffusion currents, non-homogeneity of the sample, spatial distribution of  
751 traps and the existence of an energy barrier at the metal/semiconductor interface are neglected in  
752 SCLC theory. This poses difficulties in accurately interpreting the experimental  $J$ - $V$  curves and  
753 several new models have been proposed to refine SCLC analysis.<sup>183–185,187–192</sup> The effect of the  
754 diffusion component on the current has been introduced by Bonham.<sup>187,188</sup> Dacuña and Salleo  
755 included contact asymmetry and diffusion currents to characterize the trap distribution.<sup>190</sup> They  
756 assumed a mobility edge model with a Gaussian distribution of traps centered around 0.2 eV to  
757 obtain numerical solutions to the drift-diffusion equation, but the model could only reproduce  
758 data within the energy range of 0.1–0.3 eV. Diffusion currents caused by contact asymmetry  
759 masked the states shallower than 0.1 eV and deeper than 0.3 eV and a work function offset of  
760 0.58 eV for both contacts was necessary to match the experimental data. Khan and Xun later  
761 extended this model to include a DOS with an exponential tail in addition to the Gaussian.<sup>191</sup>  
762 Dacuña and Salleo also showed that the assumption of a homogeneous trap distribution is invalid  
763 and that an asymmetric distribution of traps exists in the semiconductor.<sup>193</sup> A spatial distribution  
764 of traps near the top contact (with a trap density of  $1.2 \times 10^{12} \text{ cm}^{-3}$  and a characteristic width of  
765 32.3 nm from the semiconductor/metal interface) was needed to model the experimental curves  
766 of a rubrene crystal under both forward and reverse conditions over different temperatures.

767         While SCLC measurements are experimentally easy to perform as they only require two-  
768 terminal current-voltage measurements, careful analysis, often involving advanced numerical  
769 modelling, is required for the accurate determination of trap parameters. For this reason, OFET  
770 measurements take preference in the extraction of trap DOS spectrum. In addition, as the charge

771 carrier density, and hence the quasi-Fermi level, is modulated by the gate voltage independently  
772 of the current in the transistor channel, OFET measurements are more versatile in the extraction  
773 of trap parameters as will be discussed in the following section.

### 774 **6.1.2 OFET measurements**

775 In OFETs, the application of gate voltage causes the quasi-Fermi level of the OSC to  
776 move towards the band edges, sweeping through any trap states present in this energy interval.  
777 Therefore, OFETs provide an excellent tool for probing the density of trap states in OSCs. Here,  
778 charge carriers accumulated from the gate voltage move in the vicinity of the  
779 semiconductor/dielectric interface and therefore, OFET measurements probe the density of  
780 interfacial traps, in contrast to SCLC measurements which accesses traps within the bulk of the  
781 semiconductor. The two methods are thus complementary.

782 The simplest methods for extracting information about traps using OFETs involve the  
783 threshold voltage  $V_{th}$  and subthreshold swing  $S$ . Details on the determination of  $V_{th}$ , and  $S$  and are  
784 provided in a recent tutorial focused on OFETs.<sup>10</sup> Since  $V_{th}$  is the gate-source voltage required to  
785 fill traps at the organic/semiconductor interface before mobile charge carriers are accumulated in  
786 the transistor channel, it can be used to estimate the concentration of traps that are filled per unit  
787 area,  $N_{it}^s$ ,

$$N_{it}^s \approx \frac{C_i V_{th}}{e} \quad (8)$$

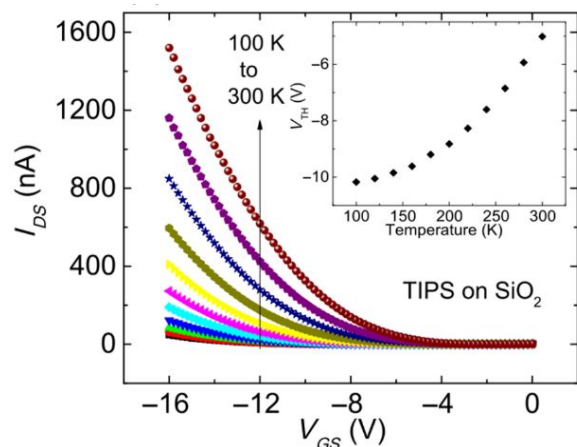


Figure 7. Transfer characteristics of a TIPS pentacene OFET with SiO<sub>2</sub> dielectric measured at different temperatures. Inset shows the threshold voltage as a function of temperature.

Reproduced with permission from ref.<sup>172</sup> Copyright 2016, American Physical Society.

788 where  $C_i$  is the areal capacitance of the dielectric and  $e$  the elementary charge. As the  
 789 temperature decreases, the injected charge carriers have less energy to be thermally activated into  
 790 the transport level and hence a larger gate-source voltage is needed to accumulate mobile charges  
 791 in the channel, leading to an increase in  $V_{th}$ . Figure 7 shows the transfer characteristics of a TIPS  
 792 pentacene OFET with SiO<sub>2</sub> dielectric obtained at several different temperatures.<sup>172</sup> The inset  
 793 shows an increase in  $V_{th}$  as the temperature is reduced. With the decrease of temperature, the  
 794 quasi-Fermi level moves further down towards the HOMO level filling up more traps. The  
 795 change in  $V_{th}$  caused by cooling is therefore a measure of the surface density of traps lying within  
 796 a few  $kT$  from the band edge.<sup>126</sup>

$$\frac{\partial V_{th}}{\partial T} \approx \frac{e}{C_i} \frac{\partial N_t^s}{\partial T} \quad (9)$$

797 The density of traps per unit area per unit energy,  $D_t^s$  is determined from the following:

$$D_t^s = \frac{\partial N_t^s}{\partial E} = \frac{C_i \partial V_{th}}{ek \partial T} \quad (10)$$

798 Here  $k$  is Boltzmann's constant.

799 Equation 10 was used to determine the areal trap density close to the HOMO band edge in  
 800 rubrene single crystals with an air-gap dielectric.<sup>126</sup>  $V_{th}$  increased quasi-linearly upon cooling and  
 801 a density of  $10^{12} \text{ cm}^{-2} \text{ eV}^{-1}$  was evaluated from the slope of the  $V_{th}$  vs  $T$  plot.

802 Another method to evaluate the trap density is by measuring  $S$ . The following expression  
 803 for the subthreshold swing can be used to estimate the density of interfacial trap states.<sup>194</sup>

$$S = \frac{kT \ln(10)}{e} \left( 1 + \frac{e \sqrt{\epsilon_s N_{bulk}^v} + e^2 N_{it}^s}{C_i} \right) \quad (11)$$

804 where,  $N_{bulk}^v$  is the bulk trap density per unit volume per unit energy,  $N_{it}^s$  is the interfacial trap  
 805 density per unit area per unit energy and  $\epsilon_s$  is the dielectric constant of the semiconductor. It is  
 806 hard to separate the contribution of bulk traps and surface traps to the subthreshold swing, but by  
 807 setting  $N_{bulk}^v = 0$  an upper limit for  $N_{it}^s$  can be determined and vice versa. Since the subthreshold  
 808 region is defined by  $V_{GS} < V_{th}$ , the quasi-Fermi level is located far from the band edges and hence  
 809 the  $S$  method probes deeper band gap states than the  $V_{th}$  method. However, the presence of any  
 810 shallow trap states can result in high off-currents which can impact  $S$  and therefore the accurate  
 811 determination of deep trap densities.<sup>157</sup> Smith et al. used the above two methods to determine the  
 812 total trap density of small molecule/polymer blended OFETs.<sup>157</sup> Different processing conditions  
 813 resulted in two distinct film microstructures characterized by small grains (SG) and large grains  
 814 (LG). Areal trap densities determined using equation 11 yielded values of  $1.8 \times 10^{12} \text{ cm}^{-2} \text{ eV}^{-1}$   
 815 for SG films and  $1.4 \times 10^{12} \text{ cm}^{-2} \text{ eV}^{-1}$  for LG films at 110 K. The difference was more  
 816 significant at 200 K, indicating that a higher density of trapped charges resides in the SG films.

817 A shallow trap density of  $\sim 1.5 \times 10^{13} \text{ cm}^{-2} \text{ eV}^{-1}$  was obtained for both films using equation 10.  
818 An order of magnitude difference in the trap densities evaluated from  $V_{th}$  and  $S$  was attributed to  
819 the different regions of traps probed by each method.

820 Podzorov and coworkers used photo-induced charge carriers in the channel of a single  
821 crystal tetracene OFET with parylene dielectric to extract information about shallow traps.<sup>195</sup>  
822 Application of a gate bias under illumination ( $V_{GS}^{illum}$ ) caused charge carriers to move across the  
823 dielectric/OSC interface and into the dielectric, resulting in a shift in the turn-on voltage,  $V_{on}$ . A  
824 monotonic decrease in mobility was observed when electrons were transferred, and no change  
825 was detected upon transfer of holes due to the fact that electrons immobilized in the dielectric  
826 create potential wells that act as shallow traps while the holes create potential bumps that only  
827 scatter them. The density of photo-induced charges was estimated from the shift in  $V_{on}$  using  
828  $\Delta N = C_i \Delta V_{on}/e$ . By measuring the mobility as a function of the photo-induced density of  
829 shallow traps,  $\mu(N)$ , a trap density of  $(3 \pm 0.5) \times 10^{11} \text{ cm}^{-2}$  (prior to illumination) and an average  
830 trapping lifetime of  $50 \pm 10 \text{ ps}$  was evaluated.

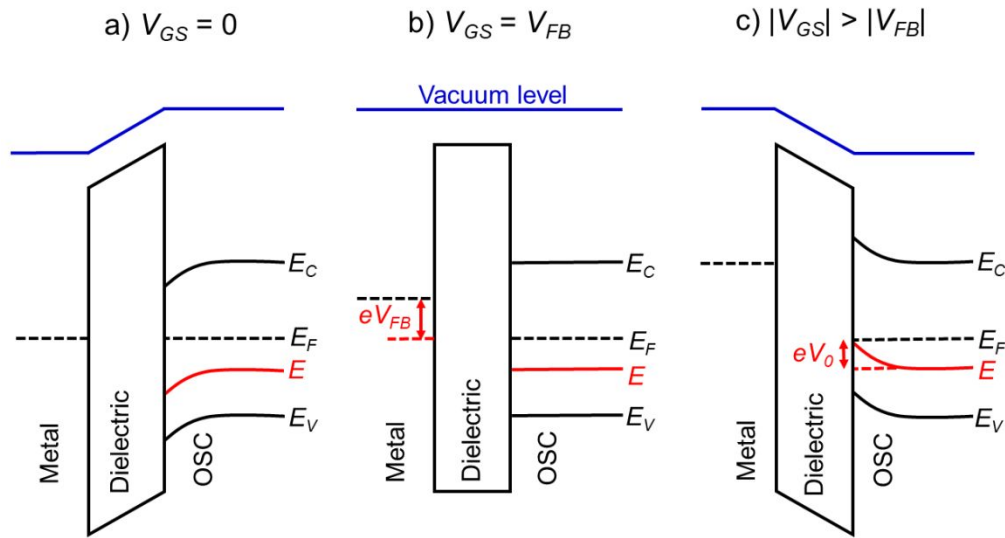
831 The above methods provide a useful comparison of shallow and deep trap densities, but  
832 they do not provide details on the energy distribution of the trapping states within the band gap,  
833 i.e., the trap DOS function. In order to quantitatively determine the trap DOS, several analytical  
834 methods and numerical methods have been developed. In the following, a few methods will be  
835 discussed to varying extents. Determination of the trap DOS spectrum exploits the fact that the  
836 gate bias induces band bending at the interface between the semiconductor and the dielectric.  
837 Figure 8 depicts the energy diagram for gate/dielectric/semiconductor interface in three voltage  
838 regimes. A p-channel transistor is considered here and the extension to n-channel transistors can  
839 be obtained by changing the sign of the gate voltage and considering states in the upper half of

840 the band gap. An initial band bending occurs even under zero bias due to energy level mismatch  
 841 between the adjacent layers (Figure 8a). In order to achieve flat bands, a gate-source voltage  
 842 called the flat band voltage ( $V_{FB}$ ) is necessary (Figure 8b). Increasing the voltage beyond  $V_{FB}$   
 843 causes band bending, as illustrated in Figure 8c, and an arbitrary trap state with energy  $E$   
 844 (represented by red solid lines) is now elevated at the interface to coincide with the quasi-Fermi  
 845 level.  $E$  corresponds to the shift in the energy bands relative to the quasi-Fermi-level at the  
 846 interface ( $x=0$ ), i.e.,  $E=E_V-E_F-eV_0$ , where  $E_V$  and  $E_F$  are the energy of the valence band edge and  
 847 the Fermi energy respectively, and  $V(x=0) = V_0$  is the interface potential. The dependence of  $V_0$   
 848 on  $V_{GS}$ , i.e. the function  $V_0(V_{GS})$ , is the key to obtaining the DOS spectrum and several models  
 849 have been developed to extract DOS from this function. The method by Grunewald et al.,  
 850 developed for a-Si transistors and later adopted for OFETs by Kalb et al.,<sup>196,197</sup> is based on the  
 851 gate voltage dependence of the field-effect conductivity. The model assumes that the  
 852 semiconductor layer is homogeneous and accounts for the initial band bending by calculating the  
 853 gate-source voltage above the flat band voltage, i.e.,  $U_{GS} = |V_{GS} - V_{FB}|$ .<sup>196</sup>  $V_{FB}$  is assumed to be  
 854 the turn-on voltage estimated from the transfer curve. The function  $V_0(V_{GS})$  is then obtained by  
 855 numerically solving the following equation (See ref <sup>196</sup> for a complete derivation):

$$\exp\left(\frac{eV_0}{kT}\right) - \frac{eV_0}{kT} - 1 = \frac{e}{kT} \frac{\varepsilon_i d}{\varepsilon_S l \sigma_0} [U_{GS} \sigma(U_{GS}) - \int_0^{U_{GS}} \sigma(\tilde{U}_{GS}) d\tilde{U}_{GS}] \quad (12)$$

856 where  $\varepsilon_i$  and  $l$  are the relative permittivity and the thickness of the dielectric, respectively,  $\sigma(U_{GS})$   
 857 is the field-effect conductivity evaluated from the linear regime transfer characteristics ( $I_D$  vs  $V_{GS}$   
 858 curve) using equation 13 and  $\sigma_0$  is the conductivity at flat band.

$$\sigma(U_{GS}) = \frac{L I_D}{W V_{DS}} \quad (13)$$



859 Here  $W$  and  $L$  are the channel width and length of the transistor respectively. Then  $V_0(V_{GS})$  is  
 860 used to determine the total hole density from,

*Figure 8. Energy level diagram at the gate/dielectric/semiconductor interface of an OFET at different gate bias, a) at  $V_{GS} = 0$  showing initial band bending at the dielectric/semiconductor interface, b) at  $V_{GS} = V_{FB}$  illustrating flat bands and c) at  $|V_{GS}| > |V_{FB}|$  depicting gate-induced band bending. Solid red lines represent an arbitrary trap state for holes, solid black lines the band edges and the broken black lines the fermi level of the respective material.*

861

$$p(V_0) = \frac{\varepsilon_0 \varepsilon_t^2}{\varepsilon_s l^2 e} U_{GS} \left( \frac{dV_0}{dU_{GS}} \right)^{-1} \quad (14)$$

862 The hole density is the convolution of the DOS with the Fermi function and hence a  
 863 deconvolution of the hole density is required in order to evaluate the DOS function. For  
 864 slowly varying trap densities, the zero-temperature approximation for the Fermi function

865 can be made. The trap DOS is then obtained by numerically differentiating the total hole  
866 density with respect to  $V_0$ . i.e.,

$$N(E) \approx \frac{1}{e} \frac{dp(V_0)}{dV_0} \quad (15)$$

867 Therefore, the trap density (per unit volume per unit energy) is plotted as a function of the  
868 interface potential which corresponds to the energy of the trap state relative to the quasi-Fermi  
869 level.

870 Grünewald's method has been widely explored by the scientific community to determine  
871 the trap DOS spectrum. Diemer et al. compared the trap DOS at two different  
872 semiconductor/dielectric interfaces, namely the interface of diF-TES ADT thin films with the  
873 fluorinated polymer dielectric Cytop and the SiO<sub>2</sub> dielectric.<sup>97</sup> Devices with Cytop dielectric  
874 yielded two orders of magnitude lower trap densities (see Figure 9a), which resulted in an order  
875 of magnitude higher charge carrier mobilities compared to the devices with SiO<sub>2</sub> dielectric (an  
876 average of  $0.17 \pm 0.19 \text{ cm}^2 \text{ V}^{-1} \text{ s}^{-1}$  and  $1.5 \pm 0.70 \text{ cm}^2 \text{ V}^{-1} \text{ s}^{-1}$  for SiO<sub>2</sub> and Cytop, respectively).  
877 Paterson et al. investigated the impact of charge carrier trapping at the semiconductor/dielectric  
878 interface on contact resistance by comparing small-molecule/polymer-blend OFETs with two  
879 polymer dielectrics, Cytop and AF2400.<sup>98</sup> The trap DOS spectrum, evaluated as a function of  
880 energy from the quasi Fermi level, indicated similar trap densities deep in the band gap, but  
881 increasing much more rapidly for devices with AF2400 as the energy approached the band edge.  
882 Devices with AF2400 yielded lower total trap densities and lower contact resistance. In the same  
883 study, the DOS analysis was performed on bias-stressed devices and was found that no  
884 trapping/detrapping occurs during operation of AF2400 devices. Grünewald's method has also

885 been employed to investigate the effect of p-doping an OSC blend containing the small molecule  
886 2,7-Dioctyl [1]benzothieno[3,2-b][1]benzothiophene (C8-BTBT) and the co-polymer IDT-BT  
887 (see Figure 9b).<sup>198</sup> A shift in trap DOS was observed only for dopant concentrations higher than  
888 1% mol, with pinning of the quasi-Fermi level dominating at lower dopant concentration.

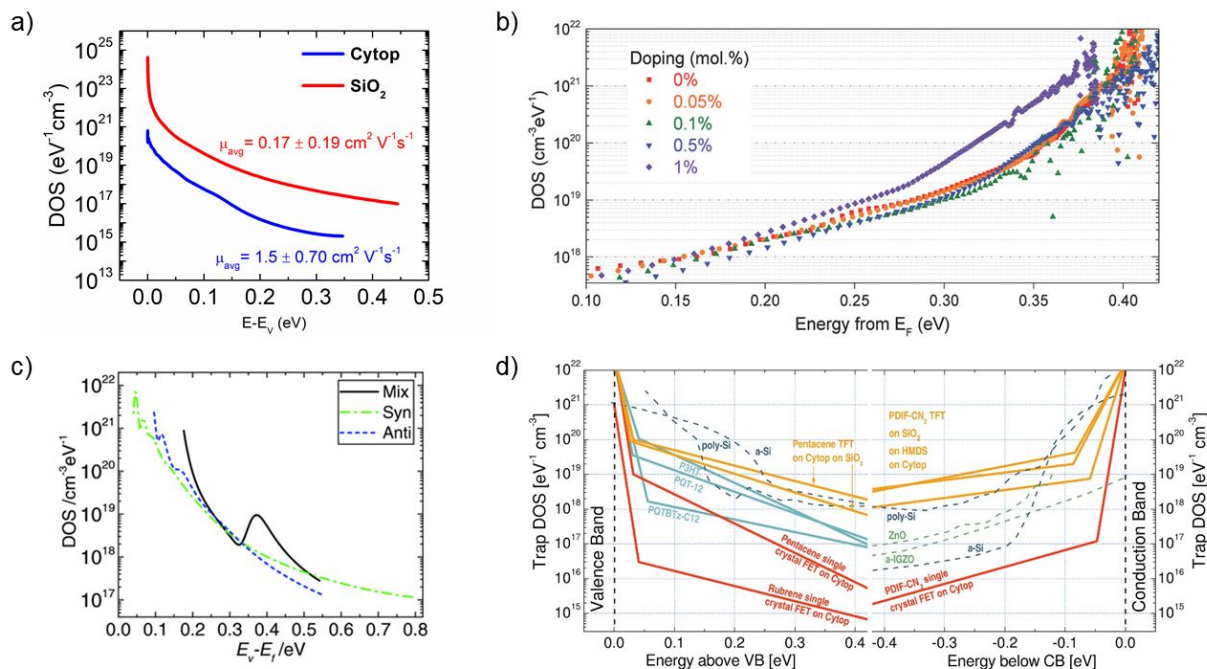


Figure 2 Figure 9. a) Comparison of the interfacial trap DOS spectrum for diF-TES ADT films with Cytop (blue) and SiO<sub>2</sub> (red) dielectrics evaluated using Grünewald's model. The value of mobility is listed in the inset. Adapted with permission from ref,<sup>97</sup> Copyright 2015, AIP Publishing LLC. b) Effect of p-doping on the trap DOS of OSC/polymer blend OFETs evaluated using Grünewald's model. Reproduced with permission form ref,<sup>198</sup> Copyright 2017, Wiley-VCH. c) Effect of isomer purity of diF-TES ADT on the trap DOS spectrum determined using Method II by Kalb et al. Broken green and blue curves represent trap DOS of pure syn- and anti- isomers respectively while the solid black lines represent that of the mix sample for reference. Reproduced with permission form ref,<sup>205</sup> Copyright 2017, Wiley-VCH. d) Comparison of the interfacial trap DOS for several organic and inorganic FETs calculated using the numerical method by Oberhoff et al. Reproduced with permission from ref,<sup>208</sup> Copyright 2010, American Physical Society.

890 Grunewald's method considers only the potential drop at the dielectric layer caused by  
891 the gate-source voltage and does not account for the potential drop across the interface. i.e.,  $V_{GS}$   
892  $-V_{FB} = V_{dielectric}$ . Such an assumption is justified for devices with thick dielectrics operating at  
893 high voltages. In the case of devices operating at low-voltage and with thin dielectrics, however,  
894 the potential drop across the semiconductor can be comparable to that across the dielectric and  
895 hence cannot be ignored. Recently Geiger et al. addressed this issue and extended the  
896 Grunewald's method for low-voltage devices by accounting for the potential drop at the  
897 interface, i.e.,  $V_{GS} - V_{FB} = V_{dielectric} + V_0$ .<sup>199</sup> The model was used to calculate the DOS spectrum  
898 of two different thin film transistors consisting of a thick and a thin gate dielectric. Devices with  
899 thick dielectric yielded similar results using both the original and extended methods. However, a  
900 significant difference in trap DOS was observed for devices with thin dielectric, with the newly  
901 proposed method being more accurate.

902 Several other analytical methods such as those by Horowitz et al.,<sup>200</sup> Lang et al.,<sup>201</sup>  
903 Fortunato et al.,<sup>202</sup> and Kalb et al.,<sup>203,204</sup> exist to extract the trap DOS spectrum. These methods  
904 are based on the temperature dependence of the field-effect conductivity and therefore require  
905 temperature dependent measurements. These methods rely on the concept of the quasi-Fermi  
906 level shift induced by a change in the gate-source voltage that, in turn, corresponds to a shift in  
907 the activation energy of the conductivity. The activation energy  $E_a$  of the field-effect  
908 conductivity is evaluated as a function of gate-source voltage, i.e.,  $E_a(V_{GS})$ , in order to determine  
909 the energy  $E$  of the trapping state ( $E \approx E_a = E_V - E_F - eV_0$ ). The field-effect conductivity is related  
910 to the temperature by an Arrhenius relation and therefore by measuring the transfer  
911 characteristics at different temperatures, the activation energy at each gate-source voltage can be  
912 determined with a linear regression analysis of  $\ln \sigma$  vs  $1/T$ . Several approximations differentiate

913 the methods. For example, Lang et al. consider the charge accumulation thickness ' $a$ ' to be  
914 independent of the gate-source voltage,<sup>201</sup> while Horowitz et al. include the gate voltage  
915 dependency in their calculations.<sup>200</sup> Fortunato et al. calculate the activation energy of the first  
916 derivative of the normalized field-effect conductivity.<sup>202</sup> Kalb et al. proposed two methods with  
917 method II an extension of method I, which follows equations 14 and 15, but with the interface  
918 potential evaluated from the activation energy of the conductivity. Method II by Kalb et al. was  
919 formulated following Fortunato et al., who considered a normalized field-effect conductivity in  
920 order to account for the temperature dependence of the band mobility  $\mu_0$ .<sup>202,204</sup> This method  
921 revealed a discrete trapping state in the band gap of in diF-TES ADT originating from the co-  
922 existence of *anti* and *syn* isomers, as illustrated in Figure 9c.<sup>205</sup> Ha et al. calculated the trap DOS  
923 spectrum for both holes and electrons in an ambipolar transistor based on diketopyrrolopyrrole-  
924 benzothiadiazole (PDPP-TBT) copolymer using the method by Lang et al. and method II by  
925 Kalb et al.<sup>206</sup> Both methods yielded similar results with symmetric trap distributions for both  
926 holes and electrons.

927         The analytic methods discussed so far approximate the Fermi-function to that at zero  
928 temperature and neglect the temperature dependence of the Fermi energy  $E_F$  and interface  
929 potential  $V_0$ . The numerical method developed by Oberhoff et al. incorporates Fermi-Dirac  
930 statistics into the calculations for the determination of the trap DOS function.<sup>207</sup> In this method, a  
931 computer program simulates the linear regime transfer characteristics at any temperature for a  
932 given distribution of traps and band mobility  $\mu_0$ . The parameters describing the DOS are varied  
933 until the generated transfer characteristics are a good fit to the experimentally measured curves.  
934 A constant DOS at the band edges, with exponential tail states decaying into the band gap, is  
935 assumed. The program allows the introduction of an additional Gaussian distribution to account

936 for any discrete trap states. Figure 9d compares the trap DOS spectrum of several p-channel and  
937 n-channel OFETs, as well as some inorganic FETs, calculated using the numerical model by  
938 Oberhoff et al.<sup>208</sup> This plot reveals similar trap DOS in OSCs and inorganic semiconductor thin  
939 films despite significant differences in charge carrier mobility. Single crystal FETs occupy the  
940 lowest part of the graph, with trap densities several orders of magnitude lower than their thin  
941 film counterparts. This highlights the effect of both disorder and morphology on the trap DOS  
942 spectrum. In a recent study, Anand et al. found that for devices with similar film morphologies,  
943 the nature of the dielectric is the main factor that determines the overall trap densities.<sup>102</sup>

944 Figure 10 compares the trap DOS spectrum calculated using all the methods described in  
945 this section applied for the same device, a pentacene thin-film transistor.<sup>204</sup> It is clear that both  
946 the choice of the method and the parameters assumed *a priori* impact the final results.<sup>204</sup> The  
947 trap density estimated from the subthreshold swing using Equation 9 is independent of energy  
948 and provides only a rough estimate for traps in the vicinity of the quasi-Fermi level located in the  
949 mid gap ( $\sim 0.5$  eV from  $E_V$ ). To be noted that the curve obtained from the simulation program  
950 accounts for complete Fermi-Dirac statistics and therefore the accuracy of all other curves are  
951 evaluated with respect to this. The method by Lang et al. underestimates the trap densities, as  
952 evident from the slope of the curve near the band edge, which was attributed to the fact that the  
953 dependence of the accumulation layer thickness on the gate-voltage was neglected. Method II by  
954 Kalb et al. and Fortunato et al. have better agreement with the results from simulation as they  
955 allow for the temperature dependence of band mobility.

956 Takeya and coworkers developed a new technique to extract the trap DOS spectrum by  
957 employing McWhorter's model for the measured flicker noise ( $1/f$  noise).<sup>209</sup> The noise arising  
958 from current fluctuations hamper OFET stability and can originate from different sources, with

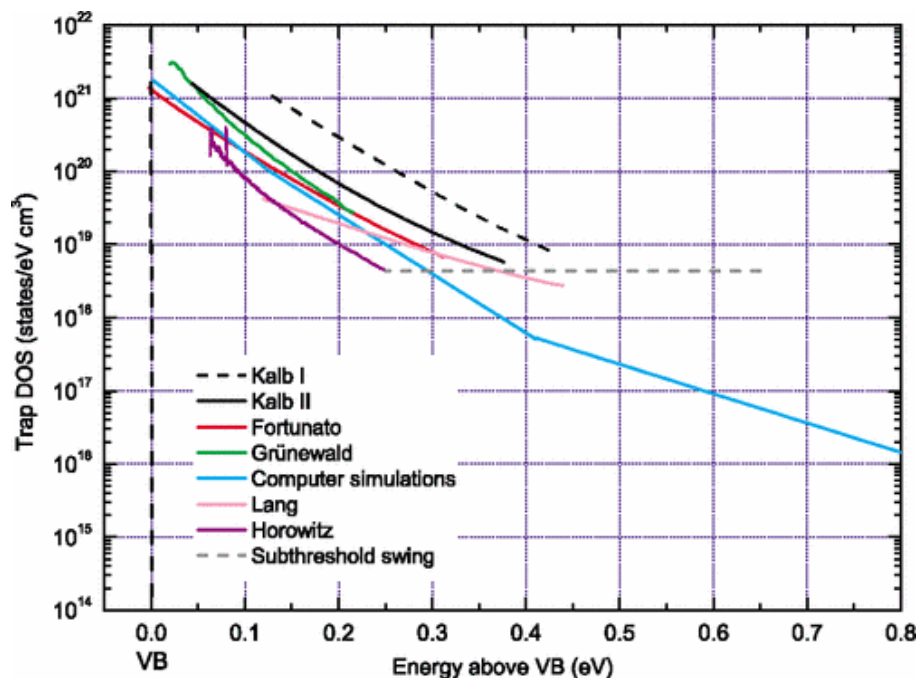


Figure 10. A comparison of the interfacial trap DOS obtained for pentacene thin-film transistors using several analytical and numerical methods. Adapted with permission from ref.<sup>204</sup> Copyright 2010, American Physical Society.

959 contact effects and charge carrier trapping being the most common.<sup>58</sup> In this study, the authors  
 960 assumed that charge trapping is the main noise source and evaluated the trap DOS spectrum from  
 961 the spectral density in the current noise. The results agree well with those from the numerical  
 962 model by Oberhoff discussed earlier. By drastically reducing the structural disorder, they  
 963 obtained charge carrier mobilities as high as  $15 \text{ cm}^2 \text{ V}^{-1} \text{ s}^{-1}$ , band-like transport and record low  
 964 flicker noise.

965

### 966 6.1.3. Impedance Spectroscopy

967 Impedance spectroscopy (IS) involves the measurement of the electrical response of a  
 968 material as a function of frequency upon applying an AC voltage. The AC voltage oscillates the

969 quasi-Fermi level of the material and when this coincides with the localized band gap states, the  
970 electrical response is altered as a result of trapping/detrapping of charge carriers in these states.  
971 Exploiting this phenomenon can provide insights into trapping mechanisms. Analysis and  
972 interpretation of the response, however, is not straightforward and several approaches such as  
973 capacitance - voltage ( $C-V$ ) analysis,<sup>210,211</sup> equivalent circuit modelling of the impedance  
974 spectrum,<sup>212,213</sup> and capacitance - frequency ( $C-f$ ) analysis,<sup>214,215</sup> are employed for this purpose.  
975 Each approach comes with several assumptions, requirements and drawbacks, limiting its  
976 general applicability. It is beyond the scope of this review to go into an in-depth discussion on  
977 the above factors, but the reader is directed to a recent exhaustive review by von Hauff on the  
978 subject.<sup>216</sup> This section will provide a brief comparison between the methods, with emphasis on  
979 trap evaluation, along with a few examples.

980  $C-V$  measurements at different frequencies provide estimates for the trap densities, but  
981 cannot determine the energy distributions, for which equivalent circuit and  $C-f$  modelling is  
982 needed. Equivalent circuit modelling has been employed to determine trap distributions in  
983 organic metal-insulator-semiconductor (MIS) capacitors based on (P3HT) and various polymer-  
984 based gate insulators.<sup>212,213</sup> Although it is a simple technique that allows for fast analysis of the  
985 impedance spectra, the challenge lies in determining an appropriate model that correlates with  
986 the frequency response of real devices.  $C-f$  eliminates the above problem and hence is more often  
987 used to characterize traps. During  $C-f$  modelling, the frequency of the applied voltage is swept  
988 until a characteristic frequency at which charges are thermally excited out of trap states is  
989 recorded. This frequency is used to determine the trapping timescale (i.e.  $\omega=2\pi f$ ). Walter et al.  
990 proposed a model for Cu In (Ga)<sub>2</sub> Se solar cells, which was later adopted for OPVs, in order to  
991 extract the trap distribution using the following equation:<sup>217</sup>

$$N(E_\omega) = -\frac{V_{FB}\omega}{de kT} \frac{\partial C(\omega)}{\partial \omega} \quad (16)$$

992 where  $E_\omega$  is the energy of the trap state w.r.t the band edge,  $C(\omega)$  is the frequency-dependent  
993 capacitance,  $d$  is the thickness of the OSC. In a bulk-heterojunction OPV based on a blend of  
994 P3HT and [6,6]-phenyl-C61 butyric acid methyl ester (PCBM), a Gaussian-like distribution of  
995 traps was determined using this method.<sup>215</sup>  $C$ - $f$  modelling assumes that changes in the  
996 capacitance results only from trapping/detrapping of charge carriers. Nevertheless, other  
997 contributions to the capacitance are possible and can give rise to artifacts in the trap spectrum.  
998 For example, due to the low charge carrier mobility, hence large transit times, the charge carriers  
999 can freeze-out at high frequencies as they no longer respond to the modulation of the applied  
1000 voltage. Therefore, the artifact, in the guise of shallow trap states, is a result of the contribution  
1001 from the geometric capacitance at high frequencies. Numerical simulations indicated that trap  
1002 distributions can be reliably extracted for thicknesses of  $\sim 100$  nm and mobilities exceeding  $10^{-4}$   
1003  $\text{cm}^2 \text{V}^{-1} \text{s}^{-1}$ .<sup>214</sup> This was further confirmed by Kirchartz and coworkers when they showed for an  
1004 OLED based on P3HT that shallow traps manifested in the trap spectrum were the result of  
1005 dielectric relaxation occurring in low mobility OSC with low trap densities.<sup>218</sup> On the other hand,  
1006 deep states with high density of states were accurately determined.  $C$ - $f$  analysis can also  
1007 determine the energetic distribution of traps when combined with other measurements. For  
1008 example, temperature dependent measurements allow the determination of the activation energy  
1009 of the trap states.<sup>219,220</sup>  $C$ - $f$  analysis has also been used in conjunction with small signal SCLC  
1010 theory, initially developed by Dascalu,<sup>221,222</sup> to extract trap DOS spectrum. Naito and coworkers  
1011 exploited this approach to determine the lifetime and energy distribution of traps in several OSCs  
1012 in an OLED configuration.<sup>220,223,224</sup> Shallow trap distributions were determined using electron-  
1013 only and hole only OLEDs, respectively, based on a polyfluorene-based light-emitting

1014 polymer.<sup>220</sup> Higher temperature measurements yielded distributions of deep states as well.  
1015 Further modification to this method was proposed to improve the energy resolution of the  
1016 measurements by reforming the analytical expression that relate the impedance spectra to the  
1017 trap distribution.<sup>224</sup>

1018

## 1019 **6.2. Optical and Thermal Methods**

1020 Optical and thermal methods are based on the photo-induced (radiative) and thermally  
1021 induced (non-radiative) transitions among electronic states, respectively. The presence of charge  
1022 carrier trapping states in the band gap will inevitably impact such measurements, and this can be  
1023 exploited in determining the nature and energetic distribution of traps.

1024 One optical method is photoemission spectroscopy (PES), also known as photoelectron  
1025 spectroscopy (PS), which is based on the principle of photoelectric effect. The energy of the  
1026 emitted electrons is measured in order to determine their binding energy. The ionization energy  
1027 needed for photoelectric effect is provided by various sources such as X-ray (XPS) or UV (UPS)  
1028 photons. This method has been used to observe directly the band gap states of single crystals of  
1029 rubrene and C<sub>60</sub>.<sup>225,226</sup> UPS measurements have been employed to detect Au-induced<sup>112</sup> and  
1030 disorder/defect-induced<sup>227</sup> band gap states in thin polycrystalline films of pentacene. In C<sub>60</sub>, a  
1031 higher density of states was detected near the valence band edge ( $10^{19}$ - $10^{21}$  eV<sup>-1</sup> cm<sup>-3</sup>) which  
1032 originated from exposure to atmospheric gases with a negligible contribution from structural  
1033 defects such as grain boundaries.<sup>225</sup>

1034 Light absorbed by the semiconductor excites the charge carriers residing in the trap states  
1035 into the conduction states, thereby generating free charge carriers and subsequently increasing

1036 the electrical conductivity of the sample, a phenomenon called photoconductivity. Thus by  
1037 measuring the changes in the current caused by changes in the conductivity, information on the  
1038 distribution of traps can be obtained. This method has been used for example, to extract the  
1039 interfacial trap DOS spectrum in thin film pentacene-based transistors.<sup>228</sup>

1040 Charge modulation spectroscopy, which probes changes in the optical absorption of the  
1041 OSC caused by the loss/acquisition of electrons from molecular orbitals, is another powerful  
1042 spectroscopic technique that has been used in characterizing traps. When combined with  
1043 temperature-dependent electrical measurements, such as FET or two-point measurements in a  
1044 diode configuration, CMS can provide insights into trapping mechanisms.<sup>47,171</sup> The applied  
1045 voltage modulates the charge carrier concentration during which shallow trap states are filled and  
1046 emptied, subsequently causing changes in the absorption (CMS) spectrum. Sakanoue et al.  
1047 observed a sharpening of the absorption peak in the CMS spectra of TIPS-pentacene OFETs at  
1048 low temperature (150-200 K) and correlated it to the temperature dependence of mobility.<sup>171</sup> The  
1049 sharpening was observed in the temperature regime where mobility was thermally activated and  
1050 hence was attributed to shallow traps. The absorption peak broadened as the lateral electric field  
1051 (drain-source voltage) was increased, implying that charges residing in shallow trap states can be  
1052 de-trapped into mobile states by application of the drain-source voltage. Charge modulation  
1053 spectroscopy has also been used to observe dynamic disorder induced tail states in various  
1054 solution-processed small molecules.<sup>47</sup>

1055 Optical methods are useful to characterize shallow traps, but cannot resolve deep non-  
1056 radiative traps, where methods that also require thermal excitations are adopted. One such  
1057 technique is the thermally-stimulated current (TSC) measurement, which involves the filling of  
1058 band gap states using charges from injection or light absorption followed by thermal excitation

1059 of the trapped charges. The filling of traps is typically done at low temperature ( $\sim 70$  K) to ensure  
1060 they are not released immediately.<sup>32</sup> The sample is then gradually heated until the trapped  
1061 charges gain enough thermal energy to get excited out of the trap states, subsequently increasing  
1062 the current. The current is recorded as function of temperature to obtain trap density and depth.  
1063 The resolution of this technique depends on the rate of sample heating. Trapping states with  
1064 depths of 0.03-0.06 eV and 0.13-0.18 eV have been identified using the TSC spectra of OLEDs  
1065 based on the polymer poly(p-phenylenevinylene) (PPV).<sup>229</sup> The shallow trap was eliminated by  
1066 replacing the ITO electrode with Au, depicting that the reaction of ITO with products eliminated  
1067 during conversion of the PPV precursor (such as HCl) lead to the formation of the trap. The deep  
1068 trap, on the other hand, appeared regardless of the electrode material and was attributed to  
1069 interaction with the environment. Tsang et al investigated the effect of introducing interlayers  
1070 of 8-hydroxyquinolino lithium between the hole blocking and electron transporting layers in  
1071 OLEDs based on a green emitter (4s,6s)-2,4,5,6-tetra(9H-carbazol-9-yl) isophthalonitrile  
1072 (4CzIPN).<sup>230</sup> The measurements indicated the reduction in the deep charge carrier trap density  
1073 upon insertion of the interlayer that subsequently enhanced the operational stability of the  
1074 devices.

1075         Deep level transient spectroscopy (DLTS) is another useful technique for the  
1076 characterization of traps. The standard technique, originally developed for inorganic materials, is  
1077 based on measuring the transient capacitance of a device during a thermal scan as a function of  
1078 time upon applying a voltage pulse.<sup>231</sup> When the voltage pulse is turned on, the quasi-Fermi level  
1079 moves in the band gap filling up trap states as it crosses them and when turned-off, the trapped  
1080 charges are thermally excited into the bands. Hence, variations in the transient capacitance due  
1081 to the discharge of excited charge carriers provide information on trap parameters. However,

1082 since OSCs generally have longer relaxation times compared to conventional semiconductors,  
1083 only small variations in capacitance are evident, making it challenging to accurately extract trap  
1084 parameters. A modified DLTS technique based on the measurement of charges released from  
1085 trapping centers instead of variations in capacitance, hence called charge-based DLTS (Q-  
1086 DLTS), yielded better accuracy.<sup>232</sup> In addition, this technique distinguishes between majority and  
1087 minority carrier traps. This method has been used to obtain the density, depth and capture cross  
1088 section in OLEDs based on PPV,<sup>232,233</sup> its derivatives,<sup>234</sup> and 4, 4'-bis(4-dimethylaminostryryl)  
1089 (DMASB).<sup>233</sup> Electronic trap distributions in OPV materials PCBM, P3HT and blends of  
1090 PCBM/P3HT have been obtained using this method.<sup>235</sup> Trap activation energies of 87 meV and  
1091 21 meV were evaluated for pure P3HT and PCBM, respectively. The blends yielded activation  
1092 energies ranging from 30-160 meV due to differences in the rate of emission of charge carriers  
1093 from the trap states.

1094 Photothermal deflection spectroscopy (PDS) is based on the photothermal deflection of a  
1095 laser beam while measuring changes in the thermal properties of a material upon absorption of  
1096 light. In this technique, the sample is immersed in a fluid of refractive index that is sensitive to  
1097 changes in temperature. A monochromatic beam of light is shone on the sample to excite the  
1098 charge carriers into the gap states. The excited charges then decay non-radiatively, emitting heat  
1099 in the process, which subsequently changes the temperature of the liquid immersed in. A probe  
1100 laser beam grazing the surface of the substrate deflects upon detecting this photo-thermally  
1101 induced change. The measurement is repeated at each wavelength of the incident beam.<sup>236</sup> PDS  
1102 spans from near-IR to the UV spectral range (~0.1- 4 eV).<sup>32</sup> Higher sensitivities can be achieved  
1103 by increasing the light exposure time at each wavelength, but this can result in long measurement  
1104 times.<sup>32</sup> Figure 11a show the PDS spectra obtained for rubrene single crystals.<sup>32</sup> The trap DOS

1105 was characterized using three exponential functions (indicated as offset broken lines) with a  
1106 steep slope of  $\sim 36$  meV close to band edge and increasing to  $\sim 61$  meV at intermediate energies  
1107 and finally to  $\sim 170$  meV deep in the band gap. In addition, a broadening of the DOS was  
1108 observed for X-ray irradiated crystals (open circles) in comparison to the pristine crystals (open  
1109 squares). The high sensitivity of this method lead to detection of molecular vibrational modes in  
1110 the PDS spectrum, as indicated by arrows in Figure 11a. However, this can be problematic as the  
1111 absorption from vibrations could mask the features obtained from electronic transitions.<sup>32</sup> PDS  
1112 has also been used to probe band gap tail states in conjugated polymers resulting from energetic  
1113 disorder.<sup>79,186</sup> Besides, the width of the density of the tail states have been estimated in terms of  
1114 the Urbach energy. Urbach energy of several high-mobility conjugated polymers with varying  
1115 crystallinity has been determined and correlated with the extent of energetic disorder.<sup>79</sup> Figure  
1116 11b shows the PDS spectra for four polymers, namely IDT-BT (black), poly(2,5-bis(3-  
1117 alkylthiophen-2-yl)thieno(3,2-b)thiophene) PBTTT (red) and diketopyrrolopyrrole (DPP) based  
1118 polymers, DPPTTT (green), PSeDPPBT (blue).<sup>79</sup> Exponential tail fits (solid lines) are included  
1119 to determine Urbach energies, which are indicated in the inset. IDT-BT yielded the sharpest  
1120 absorption onset translating into the lowest Urbach energy of 24 meV, a value which is less than  
1121  $kT$  at room temperature, in agreement with its excellent performance in OFETs.<sup>78</sup>

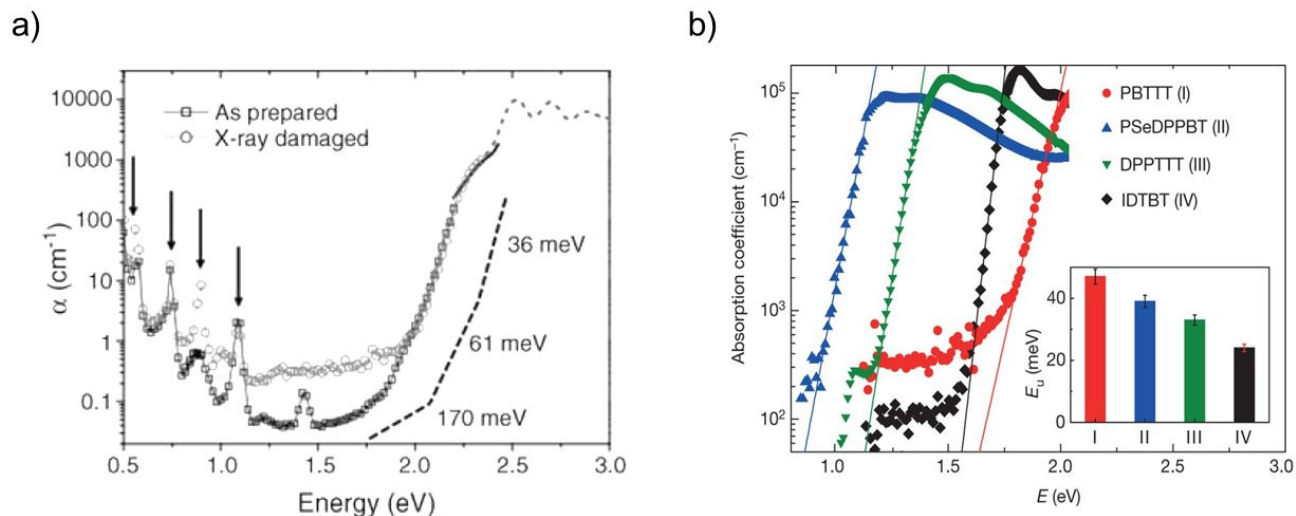


Figure 11. a) PDS spectrum of as-prepared (open squares) and X-ray exposed (open circles) rubrene single crystal. Broken lines represent exponential fits for different spectral regions and are offset for clarity. Arrows represent absorption peaks resulting from molecular vibrations. Reproduced with permission from ref<sup>32</sup>. Copyright 2013 Wiley-VCH. b) PDS spectra of several high-mobility polymers. Solid lines in inset represent exponential fits to determine the Urbach energy. Reproduced with permission from ref<sup>9</sup>. Copyright 2014, Springer Nature Ltd.

1122

### 1123 6.3. Scanning Probe Methods

1124 Scanning probe techniques such as electric force microscopy (EFM) and Kelvin probe  
 1125 force microscopy (KPFM) provide high spatial resolution imaging and map the topography of a  
 1126 surface by detecting changes in the local contact potential.<sup>237</sup> Trapped charge carriers modify the  
 1127 local contact potential and hence these techniques provide an excellent tool to determine the  
 1128 origin of traps as well as their spatial distribution. Both KPFM and EFM have been widely used  
 1129 to investigate the role of grain boundaries on charge carrier trapping in organic thin films.<sup>64,65,67</sup>  
 1130 Recently, KPFM was used to identify crystal step edges as sources of traps for electrons in single

1131 crystals of n-type semiconductor Cl<sub>2</sub>-NDI.<sup>55</sup> KPFM performed on a rubrene derivative revealed  
1132 planar defects resulting from a solid-solid phase transition during cooling.<sup>238</sup> Such defects cause  
1133 electronic disorder that could potentially introduce charge carrier traps. Mathijssen et al. studied  
1134 the dynamics of trap formation in OFETs upon exposure to ambient conditions. They found that  
1135 bias-stress effects were caused by water-related traps originating at the SiO<sub>2</sub> dielectric surface  
1136 rather than in the OSC.<sup>133</sup> Dougherty and coworkers used KPFM images to map the fluctuations  
1137 in surface potential in the transistor channel of an ultrathin  $\alpha$ -sexithiophene ( $\alpha$ -6T) OFET arising  
1138 from trapping and de-trapping of charge carrier from shallow traps.<sup>239</sup> They showed that the  
1139 spatial distribution of these fluctuations is uniform throughout the active channel.

1140 Various other techniques can be useful in the detection of traps. For example, micro  
1141 Raman imaging has been adopted to detect the coexistence of isomers in diF-TES ADT films,<sup>240</sup>  
1142 which has been previously reported to create a discrete trap state in the same material.<sup>205</sup> X-ray  
1143 based techniques such as wide angle X-ray scattering (WAXS), small angle X-ray scattering  
1144 (SAXS) and resonant soft X-ray scattering and reflectivity (r-SoXS/R) have been used to identify  
1145 structural defects, grain boundaries, interface roughness in several OSCs which also serve as  
1146 potential charge carrier traps.<sup>241</sup> Evidence for electrochemical trapping of electrons by silanol  
1147 groups in the SiO<sub>2</sub> dielectric has been acquired using multiple-reflection attenuated-total-  
1148 reflection Fourier transformed infrared (ATR-FTIR) spectrometry.<sup>96</sup>

1149

## 1150 7. Exploitation of charge carrier traps for organic sensing devices

1151 While traps are typically regarded as an obstacle to achieving high performance in  
1152 organic electronic devices, they can also be exploited towards sensing any factors that can

1153 modulate the trap DOS spectra, e.g. impurities (chemical and biological), temperature, light, or  
1154 radiation. The generation or passivation of charge carrier traps in OFET causes a measurable  
1155 change in the device performance and hence imparts the sensing mechanism. These changes may  
1156 be harnessed to detect chemical, biological or physical agents. Sensors based on OFETs have  
1157 several advantages, including biocompatibility, ease of processing, and versatility in molecular  
1158 design to address the sensitivity and selectivity challenges well beyond the capabilities of sensors  
1159 made from inorganic materials.<sup>242–246</sup> This section will provide a review of chemical, thermal and  
1160 radiation sensors that take advantage of charge trapping/de-trapping to perform sensing  
1161 operations.

1162

### 1163 **7.1. Chemical sensors**

1164 The sensitivity of OSCs to environmental molecules, i.e. ‘analytes’, make them excellent  
1165 candidates for gas sensing and odor analysis. These analytes can interact with an OSC through  
1166 hydrogen bonding and  $\pi$  interactions, or through reversible and irreversible chemical  
1167 reactions.<sup>247</sup> These interactions may occur within the bulk of the material, at grain boundaries, or  
1168 at device interfaces (metal/semiconductor, or semiconductor/dielectric).<sup>248</sup> Chemical sensing  
1169 with OFETs can be quite complicated, as there are diverse mechanisms by which the OSC  
1170 interacts with chemicals. This section will focus on sensing mechanisms which depend on trap  
1171 formation, but there can be other, non-trap related effects that have been exploited for sensing  
1172 with OFETs. For an in-depth description of chemical sensing with OFETs, we refer the reader to  
1173 several thorough reviews on the subject.<sup>242,243,249,250</sup>

1174 Using OFETs as the active element in chemical sensors allows for a greater range of  
1175 response than equivalent two-terminal devices, since chemical changes can affect the mobility,  
1176 threshold voltage, or the on/off current ratio.<sup>251</sup> One method of sensing relies on the interaction  
1177 of polar analytes with the OSC. When the OFET is exposed to a polar analyte, the dipolar  
1178 molecules induce local variations in the electric fields in the OSC. Depending on the energy  
1179 levels of the analyte with respect to the OSC, trap states can be introduced causing mobile  
1180 charges to be localized on the analyte, resulting in a lowering of the drain current or a shift in the  
1181 threshold voltage.<sup>242</sup> These effects are mediated by the processes occurring at the grain  
1182 boundaries, where the disorder leads to an increased polarizability of charge carriers. The density  
1183 of grain boundaries is related to the sensitivity of devices to analytes; polar analytes trap charges  
1184 at the grain boundaries, localizing charges in tail states, resulting in a lower overall current, and  
1185 the response is greater upon increasing the polarity of molecules.<sup>252,253</sup> The seemingly unlimited  
1186 choices of OSCs offer excellent tunability to different analytes,<sup>253,254</sup> and could be integrated into  
1187 electronic noses,<sup>255</sup> which can be used to detect, analyze, and identify odors in many  
1188 applications. Assuming that each analyte interacts with a given OSC in a distinct way, its  
1189 presence and concentration may be identified by measuring the change in operation of the  
1190 device, allowing circuits composed of multiple different OSCs to detect specific analytes. These  
1191 devices could be implemented in analyzing food freshness by sensing propanol and acetic  
1192 acid,<sup>255</sup> in identifying traces of explosives<sup>256</sup> and nerve gas,<sup>257</sup> and detecting hazardous chemicals  
1193 in work environments, at parts per million level, or below.<sup>258,259</sup>

1194 Depending on the nature of the analyte, changes to the OSC film can be reversible or  
1195 irreversible: highly reactive gases, such as NO<sub>2</sub>, cause irreversible changes to films through  
1196 chemisorption, but this can be healed via a high temperature annealing step, as shown in a copper

1197 phthalocyanine device.<sup>247</sup> Ammonia gas (NH<sub>3</sub>) is an example of a polar analyte which can be  
1198 reversibly sensed using OFETs, since it desorbs from the surface once the gas is removed from  
1199 the environment. Ammonia sensing is also in high demand as it is a highly toxic and corrosive  
1200 agent, and due to its ubiquitous use in industrial and agricultural settings. Katz and coworkers  
1201 demonstrated an OFET based on poly (3,3''-didodecylquaterthiophene) (PQT-12) with a  
1202 sensitivity of 0.5 ppm when exposed to ammonia, and more recently showed that this effect is  
1203 exhibited in both n-type and p-type OSCs, 2,20 - [(2,5-dihexadecyl-3,6-dioxo-2,3,5,6-  
1204 tetrahydropyrrolo- [3,4-c] pyrrole-1,4-diylidene) dithiene-5,2-diylidene] dimalononitrile  
1205 (DPPCN) and P3HT, respectively.<sup>260,261</sup> In addition to a high sensitivity, these devices exhibited  
1206 a high selectivity to ammonia, and a memory effect when cooled. Adsorption of ammonia onto  
1207 the surface of the semiconductor induced energetic disorder and charge - dipole interactions,  
1208 which resulted in a decrease in the drain current of the device. By a similar route, adsorption of  
1209 ammonia onto spray-coated TIPS pentacene caused a threshold voltage shift, and a decrease in  
1210 mobility and drain current.<sup>248</sup> Ethanol was detected using pentacene OFETs by studying the  
1211 temperature dependence of mobility; the authors showed that exposure to ethanol vapors  
1212 increases the activation energy, indicating that charges are deeply trapped when the vapor is  
1213 introduced.<sup>262</sup>

1214

## 1215 **7.2. Temperature Sensors**

1216 The development of small, light-weight, and biocompatible temperature sensors has the  
1217 potential to revolutionize the medical field. Temperature and pressure sensing has been achieved  
1218 through the use of OFETs coupled with capacitive elements, such as a microstructured PDMS,<sup>263</sup>  
1219 or by using piezoelectrics as sensing elements, in series with the gate of an OFET.<sup>264,265</sup> More

1220 recently, temperature sensing relying on trapping allowed for the entire sensor to be contained  
1221 within a single OFET device, without additional hardware or processing, offering a clear  
1222 advantage over the more complicated and bulky capacitance-based devices.

1223         As discussed in Section 5, the temperature dependence of mobility is strongly related to  
1224 the density and distribution (both energetic and spatial) of traps. Strategic choices of dielectric  
1225 materials can be used to impart a greater range of thermal sensitivity and expand the sensor use.  
1226 For example, OFETs based on dielectrics with strong polar groups, such as polyactide (PLA),  
1227 have a high trap density (both deep and shallow) at the semiconductor/dielectric interface.<sup>245</sup> By  
1228 adding heat into the system, carriers are released from traps, and the threshold voltage showed a  
1229 sensitivity of  $\sim 0.25$  V/K, with a nearly linear response, making this is a viable method to  
1230 creating temperature sensors. In addition to imparting temperature sensitivity beyond room  
1231 temperature, PLA is biocompatible, making it an appealing material for use in medical  
1232 applications. This strategy has also been employed using other polar dielectrics, such as poly-  
1233 (vinyl alcohol) with a copper phthalocyanine (CuPc) semiconductor, which exhibited a similar  
1234 temperature response above room temperature, with reversible changes in device operation.<sup>266</sup>  
1235 More recent work has shown that different metal atoms can impart metal phthalocyanines with  
1236 an increased response to temperature, such as Mg and Fe, without the use of a polar dielectric  
1237 layer, which could lead to simpler fabrication techniques than dielectric modification.<sup>267</sup>

1238

### 1239         **7.3. Light/Radiation sensors**

1240         Photodetectors and radiation detectors based on OSCs are very appealing; their  
1241 biocompatibility and conformability make them useful in applications ranging from medical

1242 research, such as sensors attached to the skin,<sup>246,268</sup> to industrial applications.<sup>269</sup> This section will  
1243 focus on near-infrared (NIR), visible light, ultra-violet (UV), and high-energy radiation sensors  
1244 which rely on charge trapping.

1245         When incident photons are absorbed into the OSC, an exciton is created, which then  
1246 diffuses through the OSC until reaching a trap (e.g. defect, impurity, or surface state) where it  
1247 dissociates into a free electron and a hole. Holes and electrons may encounter donor or acceptor-  
1248 like traps, respectively, causing an increase in the current density in the channel as well as a shift  
1249 in the threshold voltage.<sup>270</sup> The sensing mechanism relies on trapping and de-trapping of the  
1250 majority or minority carriers, which reduces the recombination rate, thus enhancing the  
1251 concentration of one carrier type. The trap sensitivity can be manipulated by choice of the  
1252 dielectric, or by utilizing semiconductor blends which strategically increase the trap  
1253 density.<sup>269,271</sup>

1254         Sensing in the near infrared has many potential applications in imaging, night vision,  
1255 health diagnosis, and industrial monitoring. One example is a bulk heterojunction of poly (N-  
1256 alkyl diketopyrrolo-pyrrole dithienylthieno[3,2-b] thiophene) (DPP-DTT) and PCBM in a  
1257 phototransistor configuration. The narrow bandgap and high absorption in the near-infrared make  
1258 these materials ideal for NIR sensing. The devices exhibited responsivities of up to  $5 \times 10^5 \text{ A W}^{-1}$   
1259 <sup>1</sup>, with a gain of  $\sim 10^4$ , though the responsivity decreases with light intensity due to filling of  
1260 longest-lived trap states, leaving the short-lived trap states to dominate the gain effects.<sup>272</sup> A  
1261 similar strategy was used by Sun et al., who added PbS quantum dots in P3HT thin-film  
1262 transistors. In this case the electrons were trapped on the PbS domains, and responsivities up to  $2$   
1263  $\times 10^4 \text{ A W}^{-1}$  were achieved; for reference neat P3HT showed negligible photoresponse.<sup>273</sup> Qiu, et  
1264 al. used bis(2-oxoindolin-3-ylidene)-benzodifuran-dione (PBIBDF-TT) nanowires (PBIBDF-TT

1265 absorbs in the NIR region) to fabricate photodetectors, and recorded the highest sensitivity when  
1266 SiO<sub>2</sub> was used as dielectric owing to the high trap density characteristic to these devices.<sup>269</sup>  
1267 Operation in air increased the photoresponse further, and the authors postulated that the high  
1268 surface/volume ratio increased the number of trap sites from adsorbed H<sub>2</sub>O and O<sub>2</sub>, which further  
1269 traps photogenerated charges, increasing the photoconductive gain.

1270         Efforts focused on visible light sensing rely primarily on charge trapping at the dielectric  
1271 surface.<sup>271</sup> Park et. al fabricated pentacene FET devices using poly (methyl methacrylate)  
1272 (PMMA), poly(4-vinylphenol) (PVP), and Cytop dielectrics, and studied the impact of the  
1273 dielectric on photosensitivity: PMMA contains an ester group, which acts as a trapping site for  
1274 holes, PVP has electron trapping hydroxyl groups, and Cytop is inert. They found that the FETs  
1275 with PVP dielectric showed the greatest photo response and the traps induced a hysteresis effect,  
1276 which is useful in memory applications. By increasing the concentration of hydroxyl groups in  
1277 the PVP layer, the authors were able to increase the photocurrent and hysteresis effect. While  
1278 PMMA and Cytop did not give the hysteresis effect, they still exhibited a mild photoresponse,  
1279 which was attributed to trapping at the grain boundaries in the pentacene film. A similar effect  
1280 was observed by Kim et al., in inkjet printed  $\alpha,\omega$ -dihexylquarterthiophene (DH4T) OFETs with a  
1281 PVP dielectric: they found that electron trapping shifts the threshold voltage and results in an  
1282 increase in the density of photoinduced holes in the channel.<sup>274</sup> Polyactide (PLA) dielectrics also  
1283 increase photosensitivity by introducing strong polar groups into the dielectric. This dielectric  
1284 allowed them to detect light with intensity as low as 0.02 mW cm<sup>-2</sup>, with a photosensitivity of  
1285 10<sup>4</sup>.<sup>275</sup>

1286         The detection of UV light often requires the use of filters or waveguides to separate UV  
1287 from visible light,<sup>276</sup> which increases the complexity of traditional UV sensors. Smithson et al.

1288 demonstrated a sensor which was inert to visible light, and only detected UV radiation, without  
1289 the need for complicated waveguides.<sup>277</sup> This was achieved by creating a blend of a polymer  
1290 binder with strong electron donating amine groups, azobenzene derivative disperse red 1 (*p*-  
1291 DR1), and 2,7-dipentyl[1]benzothieno[3,2-*b*][1] benzothiophene (C5-BTBT) and recording the  
1292 shift in the threshold voltage as a function of the intensity of the radiation. Huang et. al used an  
1293 electret layer, namely a doped triphenylamine (TPA)-based polymer, between the pentacene film  
1294 and the dielectric layer, to achieve UV sensing and an UV programmable memory effect. The  
1295 electret layer serves a dual function: first, upon UV irradiation, it has an emission peak which  
1296 overlaps the absorption peak of pentacene, enhancing exciton creation, and second, it traps  
1297 electrons from dissociated excitons, increasing the hole photocurrent. The trapped electrons may  
1298 be ‘erased’ with UV light, serving the memory function, though the responsivity of these devices  
1299 was low, at  $\sim 45 \text{ A W}^{-1}$ .<sup>278</sup>

1300 Sensing of ionizing radiation (X-rays/ $\gamma$ -rays), as well as the sensing of charged particles,  
1301 such as protons, is a subject of recent attention,<sup>279,280</sup> owing to the possible applications that they  
1302 may enable. While in some devices the sensing mechanism is similar to that used to detect NIR  
1303 and visible light, other devices rely on the creation of traps in devices when exposed to radiation.  
1304 Batlogg and coworkers showed that proton irradiation of single crystal rubrene created deep trap  
1305 states in the crystal, which was attributed to a breaking in the C-H bonds.<sup>141</sup> They also showed  
1306 that X-ray irradiation causes local disorder in the crystal, a common source of traps in OSCs.<sup>281</sup>  
1307 Proton irradiation of TIPS pentacene OFETs resulted in a decrease in device mobility as a result  
1308 of the fact that the heavy particles caused structural disorder within the organic film.<sup>282</sup> In the  
1309 same material, it has been shown that irradiation with X-rays produces a photoconductive gain  
1310 effect: the authors attributed this to an increase in the conductivity of the films by the

1311 accumulation of free charge carriers, which act as a dopant.<sup>280</sup> Later, they amplified the  
1312 photoconductive gain by using a FET configuration and substituting TIPS-pentacene with diF-  
1313 TES ADT and diF-TEG ADT. The inclusion of Si and Ge atoms into the molecular structure  
1314 provided a high-Z component, which increased the response to high energy photons because of  
1315 the high scattering cross section of these atoms.<sup>279</sup>

1316

#### 1317 **7.4. Memory Devices based on Charge Trapping**

1318 A robust control of the dynamics of charge trapping led to its exploitation in memory  
1319 applications; long-lived trap states induce shifts in current-voltage characteristics, and while such  
1320 behavior is not desired for a typical device operation (see for example the effects described in  
1321 Section 4), it can give rise to discrete memory states. The memory states form the basis for a  
1322 variety of applications, from imparting memory capabilities to flexible circuits to mimicking  
1323 neurons in neuromorphic circuits for artificial intelligence and deep learning.<sup>283–287</sup> In synaptic  
1324 memory devices, control of the charge trapping was accomplished by doping the OSC with  
1325 either non-metallic particles (e.g. ZnO),<sup>288</sup> or metallic particles (e.g. Au).<sup>289</sup> These particles trap  
1326 charges in the conduction channel, therefore altering the device characteristics. Memories based  
1327 on this method have long retention times, but need to be ‘read’ by applying a gate voltage, which  
1328 can affect the stored memory state.<sup>284</sup> Techniques which make use of photochromic molecules,  
1329 such as spiropyran, azobenzene, or diarylethene, can overcome this limitation, since the memory  
1330 is switching using light, and not the electric field.<sup>290</sup> These molecules change their conformation  
1331 upon exposure to UV light, which is key to their function as memory devices.<sup>291,292</sup> For example,  
1332 Samorì and coworkers utilized a blend of diarylethene (DAE) photochromic molecules P3HT to  
1333 realize a photo-switchable memory device.<sup>293</sup> When the DAE was exposed to UV light, the

1334 isomer 'switched' to the closed state, whose HOMO was within the bandgap of the P3HT, and  
1335 therefore acted as a hole trap, reducing the current of the device. The trapping/de-trapping was  
1336 highly stable and reversible: DAE molecules revert to the open isomer by exposure to visible  
1337 light, and the devices modulated the current continuously, allowing many possible memory  
1338 states, imparting organic electronic devices the ability to act as memory devices in complex  
1339 circuits.

1340

## 1341 **8. Summary and future perspectives:**

1342 Charge carrier trapping is ubiquitous in OSCs and is a direct consequence of van der  
1343 Waals intermolecular interactions inherent in these materials. The details on the nature, spatial  
1344 and energetic distribution of traps, as well as timescales of trapping/de-trapping events, have a  
1345 profound impact on the performance of organic electronic devices. Studies related to the subject  
1346 date back to the 1960s, when the research focused almost exclusively on free standing molecular  
1347 crystals.<sup>33,34,54</sup> Later, the effort was expanded to address charge carrier trapping occurring in thin  
1348 films and at device interfaces. Tail states introduced by dynamic disorder arising from thermal  
1349 motions and their role in charge carrier trapping have also recently garnered attention. In this  
1350 review, we aimed to provide readers with a comprehensive overview on the phenomenon of  
1351 charge carrier trapping in OSC materials and opto-electronic devices. Beginning with the  
1352 definition of traps, we then discussed their origin and properties, categorized the sources of traps  
1353 in OSCs and provided examples for each case. Sources of traps range from structural defects to  
1354 chemical impurities, from devices interfaces to environmental effects, with many of these effects  
1355 being coupled. A discussion on the impact of charge carrier trapping on the mechanism of charge  
1356 transport and the performance of organic electronic devices was provided, including strategies

1357 adopted to mitigate these effects for optimal device function. Next, we discussed the  
1358 experimental techniques available for the detection and characterization of traps. Optical and  
1359 thermal methods rely on radiative and non-radiative electronic transitions between localized  
1360 band gap states enabling the extraction of trap parameters, with thermal methods having the  
1361 potential of probing deeper band gap states. Electrical measurements in device configurations  
1362 such as OFETs and two terminal devices serve as excellent tools to extract energetic distribution  
1363 of traps, while scanning probe techniques are useful in determining the spatial distribution of  
1364 traps. Applications such as chemical, temperature and radiation sensors, in which the  
1365 phenomenon of charge carrier trapping is exploited for detection were briefly discussed.

1366         Remarkable progress has been made over the years in terms of characterization of traps,  
1367 clarifying the impact on charge transport and reducing undesirable effects through innovations in  
1368 material design and device fabrication. Increasingly better understanding of the phenomenon has  
1369 led to new design rules for organic devices, and made the reduction in the density of charge  
1370 carrier traps possible. For example, OSCs with an ionization energy of less than 6 eV and an  
1371 electron affinity greater than 3.6 eV are predicted to yield trap-free charge transport of both holes  
1372 and electrons, which is an important milestone achieved that can subsequently enhance device  
1373 performance to a great extent.<sup>86</sup> Despite the numerous efforts, unanswered questions still persist.  
1374 Most methods for trap characterization are indirect and require different levels of  
1375 approximations, often making the interpretation of results difficult. Systematic studies involving  
1376 deliberate incorporation of traps to investigate their effect on the DOS spectrum are rare. Access  
1377 to each source of trap independently would clarify its impact on charge transport, but this is  
1378 practically impossible because many trapping events are correlated (e.g. an impurity generates  
1379 energetic as well as structural disorder). In addition, studying the dynamics of trap states is

1380 another challenging direction of future research. Elucidating the time evolution of trap states will  
1381 aid in comprehending the effect of dynamic disorder, the major performance-limiting factor in  
1382 electronic devices. Resolving these issues, coupled with progress in understanding and  
1383 enhancing charge injection, development of new materials, and optimizing device structure, will  
1384 lead to significant improvements in the performance of electronic devices, enabling their full  
1385 potential to be realized in real-world applications.

#### 1386 **Acknowledgements:**

1387 This work was supported by the National Science Foundation through Grant Nos. DMR-  
1388 1627925 and ECCS- 1810273.

#### 1389 **Conflicts of interest:**

1390 The authors declare no conflicts of interest.

#### 1391 **References:**

- 1392 1 A. C. Arias, J. D. MacKenzie, I. McCulloch, J. Rivnay and A. Salleo, *Chem. Rev.*, 2010,  
1393 **110**, 3–24.
- 1394 2 N. Gasparini, A. Salleo, I. McCulloch and D. Baran, *Nat. Rev. Mater.*, 2019, **4**, 229–242.
- 1395 3 H. Sirringhaus, *Adv. Mater.*, 2014, **26**, 1319–1335.
- 1396 4 H. Klauk, *Chem. Soc. Rev.*, 2010, **39**, 2643.
- 1397 5 J. E. Anthony, A. Facchetti, M. Heeney, S. R. Marder and X. Zhan, *Adv. Mater.*, 2010, **22**,  
1398 3876–3892.
- 1399 6 M. Kuik, G. J. A. H. Wetzelaer, H. T. Nicolai, N. I. Craciun, D. M. De Leeuw and P. W.  
1400 M. Blom, *Adv. Mater.*, 2014, **26**, 512–531.
- 1401 7 J. L. Bredas, J. P. Calbert, D. A. da Silva Filho and J. Cornil, *Proc. Natl. Acad. Sci.*, 2002,  
1402 **99**, 5804–5809.
- 1403 8 V. Coropceanu, J. Cornil, D. A. da Silva Filho, Y. Olivier, R. Silbey and J.-L. Brédas,  
1404 *Chem. Rev.*, 2007, **107**, 926–952.
- 1405 9 A. Troisi and G. Orlandi, *J. Phys. Chem. A*, 2006, **110**, 4065–4070.

- 1406 10 Z. A. Lamport, H. F. Haneef, S. Anand, M. Waldrip and O. D. Jurchescu, *J. Appl. Phys.*,  
1407 2018, **124**, 071101.
- 1408 11 J.-P. Yang, F. Bussolotti, S. Kera and N. Ueno, *J. Phys. D. Appl. Phys.*, 2017, **50**, 423002.
- 1409 12 C. D. Dimitrakopoulos and P. R. L. Malenfant, *Adv. Mater.*, 2002, **14**, 99–117.
- 1410 13 S. Fratini, D. Mayou and S. Ciuchi, *Adv. Funct. Mater.*, 2016, **26**, 2292–2315.
- 1411 14 E. A. Silinsh and V. Capek, *Organic Molecular Crystals: Interacton Localization, and*  
1412 *Transport Phenomena*, AIP Press, New York, 1994.
- 1413 15 A. Troisi, *Chem. Soc. Rev.*, 2011, **40**, 2347–2358.
- 1414 16 N. A. Minder, S. Ono, Z. Chen, A. Facchetti and A. F. Morpurgo, *Adv. Mater.*, 2012, **24**,  
1415 503–508.
- 1416 17 S. Ciuchi, S. Fratini and D. Mayou, *Phys. Rev. B - Condens. Matter Mater. Phys.*, 2011,  
1417 **83**, 1–4.
- 1418 18 S. M. Sze and K. K. Ng, *Physics of Semiconductor Devices*, Wiley-Interscience, Hoboken.  
1419 NJ, 2007.
- 1420 19 G. Horowitz, *J. Appl. Phys.*, 2015, **118**, 115502.
- 1421 20 A. R. Völkel, R. A. Street and D. Knipp, *Phys. Rev. B - Condens. Matter Mater. Phys.*,  
1422 2002, **66**, 1953361–1953368.
- 1423 21 J. Rivnay, R. Noriega, J. E. Northrup, R. J. Kline, M. F. Toney and A. Salleo, *Phys. Rev. B*  
1424 *- Condens. Matter Mater. Phys.*, 2011, **83**, 1–4.
- 1425 22 N. Mott, *J. Phys. C Solid State Phys.*, 1987, **20**, 3075–3102.
- 1426 23 H. Bässler, *Phys. status solidi*, 1993, 175, 15–56.
- 1427 24 I. V. Arkhipov, P. Heremans, E. V. Emelianova, G. J. Adriaenssens and H. Bässler, *J.*  
1428 *Phys. Condens. Matter*, 2002, **14**, 9899–9911.
- 1429 25 J. P. Sleigh, D. P. McMahon and A. Troisi, *Appl. Phys. A Mater. Sci. Process.*, 2009, **95**,  
1430 147–152.
- 1431 26 K. Willa, R. Häusermann, T. Mathis, A. Facchetti, Z. Chen and B. Batlogg, *J. Appl. Phys.*,  
1432 2013, **113**, 133707.
- 1433 27 J. E. Anthony, C. Warwick, L. Jiang, M. Nikolka, Y. Henri Geerts, H. Sirringhaus, G.  
1434 Schweicher, A. S. Eggeman, A. Troisi, S. G. Yeates and S. Illig, *Nat. Commun.*, 2016, **7**,  
1435 1–10.
- 1436 28 O. Simonetti and L. Giraudet, *Polym. Int.*, 2019, **68**, 620–636.
- 1437 29 G. Horowitz and P. Delannoy, *J. Appl. Phys.*, 1991, **70**, 469–475.
- 1438 30 G. Horowitz, P. Lang, M. Mottaghi and H. Aubin, *Adv. Funct. Mater.*, 2004, **14**, 1069–  
1439 1074.

- 1440 31 M. C. J. M. Vissenberg and M. Matters, *Phys. Rev. B*, 1998, **57**, 12964–12967.
- 1441 32 A. Salleo, in *Organic Electronics*, Wiley-VCH Verlag GmbH & Co. KGaA, Weinheim,  
1442 Germany, 2013, pp. 341–380.
- 1443 33 E. A. Silinsh, *Organic Molecular Crystals: Their electronic states*, Springer Berlin  
1444 Heidelberg, Berlin, Heidelberg, 1980.
- 1445 34 E. A. Silinsh, *Phys. status solidi*, 1970, **3**, 817–828.
- 1446 35 A. Rose, *Phys. Rev.*, 1955, **97**, 1538–1544.
- 1447 36 J. Sworakowski and K. Pigoń, *J. Phys. Chem. Solids*, 1969, **30**, 491–496.
- 1448 37 S. D. Baranovskii, *Phys. Status Solidi Basic Res.*, 2014, **251**, 487–525.
- 1449 38 P. W. Anderson, *Phys. Rev.*, 1958, **109**, 1492–1505.
- 1450 39 T. F. Harrelson, V. Dantanarayana, X. Xie, C. Koshnick, D. Nai, R. Fair, S. A. Nuñez, A.  
1451 K. Thomas, T. L. Murrey, M. A. Hickner, J. K. Grey, J. E. Anthony, E. D. Gomez, A.  
1452 Troisi, R. Faller and A. J. Moulé, *Mater. Horizons*, 2019, **6**, 182–191.
- 1453 40 H. T. Yi, Y. N. Gartstein and V. Podzorov, *Sci. Rep.*, 2016, **6**, 1–11.
- 1454 41 A. V Nenashev, J. O. Oelerich and S. D. Baranovskii, *J. Phys. Condens. Matter*, 2015, **27**,  
1455 093201.
- 1456 42 S. D. Baranovskii, *Phys. Status Solidi Appl. Mater. Sci.*, 2018, **215**, 1–12.
- 1457 43 N. R. Tummala, Z. Zheng, S. G. Aziz, V. Coropceanu and J.-L. Brédas, *J. Phys. Chem.*  
1458 *Lett.*, 2015, **6**, 3657–3662.
- 1459 44 A. Troisi and G. Orlandi, *Phys. Rev. Lett.*, 2006, **96**, 1–4.
- 1460 45 D. L. Cheung and A. Troisi, *Phys. Chem. Chem. Phys.*, 2008, **10**, 5941–5952.
- 1461 46 S. Ciuchi and S. Fratini, *Phys. Rev. B - Condens. Matter Mater. Phys.*, 2012, **86**, 1–14.
- 1462 47 A. Y. B. Meneau, Y. Olivier, T. Backlund, M. James, D. W. Breiby, J. W. Andreasen and  
1463 H. Sirringhaus, *Adv. Funct. Mater.*, 2016, **26**, 2326–2333.
- 1464 48 C. Krellner, S. Haas, C. Goldmann, K. P. Pernstich, D. J. Gundlach and B. Batlogg, *Phys.*  
1465 *Rev. B*, 2007, **75**, 245115.
- 1466 49 S. Haas, A. F. Stassen, G. Schuck, K. P. Pernstich, D. J. Gundlach, B. Batlogg, U. Berens  
1467 and H. J. Kirner, *Phys. Rev. B - Condens. Matter Mater. Phys.*, 2007, **76**, 1–6.
- 1468 50 H. Jiang and W. Hu, *Angew. Chemie Int. Ed.*, 2019, 2–23.
- 1469 51 P. M. Robinson and H. G. Scott, *Phys. status solidi*, 1967, **20**, 461–471.
- 1470 52 J. M. Thomas and J. O. Williams, *Prog. Solid State Chem.*, 1971, **6**, 119–154.
- 1471 53 F. Lohmann and W. Mehl, *J. Chem. Phys.*, 1969, **50**, 500–506.
- 1472 54 M. Pope and C. E. Swenberg, *Electronic Processes in Organic Crystals and Polymers*,

- 1473 Oxford University Press, 1999.
- 1474 55 T. He, Y. Wu, G. D'Avino, E. Schmidt, M. Stolte, J. Cornil, D. Beljonne, P. P. Ruden, F.  
1475 Würthner and C. D. Frisbie, *Nat. Commun.*, 2018, **9**, 2141.
- 1476 56 S. S. Lee, C. S. Kim, E. D. Gomez, B. Purushothaman, M. F. Toney, C. Wang, A.  
1477 Hexemer, J. E. Anthony and Y.-L. Loo, *Adv. Mater.*, 2009, **21**, 3605–3609.
- 1478 57 H. H. Choi, A. F. Paterson, M. A. Fusella, J. Panidi, O. Solomeshch, N. Tessler, M.  
1479 Heeney, K. Cho, T. D. Anthopoulos, B. P. Rand and V. Podzorov, *Adv. Funct. Mater.*,  
1480 2019, **1903617**, 1903617.
- 1481 58 O. D. Jurchescu, B. H. Hamadani, H. D. Xiong, S. K. Park, S. Subramanian, N. M.  
1482 Zimmerman, J. E. Anthony, T. N. Jackson and D. J. Gundlach, *Appl. Phys. Lett.*, 2008, **92**,  
1483 132103.
- 1484 59 J. Rivnay, L. H. Jimison, J. E. Northrup, M. F. Toney, R. Noriega, S. Lu, T. J. Marks, A.  
1485 Facchetti and A. Salleo, *Nat. Mater.*, 2009, **8**, 952–958.
- 1486 60 R. Li, J. W. Ward, D.-M. Smilgies, M. M. Payne, J. E. Anthony, O. D. Jurchescu and A.  
1487 Amassian, *Adv. Mater.*, 2012, **24**, 5553–5558.
- 1488 61 C. P. L. Rubinger, H. F. Haneef, C. Hewitt, D. Carroll, J. E. Anthony and O. D. Jurchescu,  
1489 *Org. Electron.*, 2019, **68**, 205–211.
- 1490 62 S. Hunter and T. D. Anthopoulos, *Adv. Mater.*, 2013, **25**, 4320–4326.
- 1491 63 L. G. Kaake, P. F. Barbara and X.-Y. Zhu, *J. Phys. Chem. Lett.*, 2010, **1**, 628–635.
- 1492 64 E. M. Muller and J. A. Marohn, *Adv. Mater.*, 2005, **17**, 1410–1414.
- 1493 65 M. Jaquith, E. M. Muller and J. A. Marohn, *J. Phys. Chem. B*, 2007, **111**, 7711–7714.
- 1494 66 M. J. Jaquith, J. E. Anthony and J. A. Marohn, *J. Mater. Chem.*, 2009, **19**, 6116–6123.
- 1495 67 K. Puntambekar, J. Dong, G. Haugstad and C. D. Frisbie, *Adv. Funct. Mater.*, 2006, **16**,  
1496 879–884.
- 1497 68 G. Horowitz, M. E. Hajlaoui and R. Hajlaoui, *J. Appl. Phys.*, 2000, **87**, 4456–4463.
- 1498 69 M. Tello, M. Chiesa, C. M. Duffy and H. Sirringhaus, *Adv. Funct. Mater.*, 2008, **18**,  
1499 3907–3913.
- 1500 70 L. C. Teague, B. H. Hamadani, O. D. Jurchescu, S. Subramanian, J. E. Anthony, T. N.  
1501 Jackson, C. A. Richter, D. J. Gundlach and J. G. Kushmerick, *Adv. Mater.*, 2008, **20**,  
1502 4513–4516.
- 1503 71 T. W. Kelley and C. D. Frisbie, *J. Phys. Chem. B*, 2001, **105**, 4538–4540.
- 1504 72 S. S. Lee, J. M. Mativetsky, M. A. Loth, J. E. Anthony and Y. L. Loo, *ACS Nano*, 2012, **6**,  
1505 9879–9886.
- 1506 73 L. H. Jimison, M. F. Toney, I. McCulloch, M. Heeney and A. Salleo, *Adv. Mater.*, 2009,  
1507 **21**, NA-NA.

- 1508 74 J. H. Kang, D. Da Silva Filho, J. L. Bredas and X. Y. Zhu, *Appl. Phys. Lett.*, 2005, **86**, 1–  
1509 3.
- 1510 75 P. J. Diemer, C. R. Lyle, Y. Mei, C. Sutton, M. M. Payne, J. E. Anthony, V. Coropceanu,  
1511 J. Brédas and O. D. Jurchescu, *Adv. Mater.*, 2013, **25**, 6956–6962.
- 1512 76 D. Abbaszadeh, A. Kunz, N. B. Kotadiya, A. Mondal, D. Andrienko, J. J. Michels, G.-J.  
1513 A. H. Wetzelaer and P. W. M. Blom, *Chem. Mater.*, 2019, **31**, 6380–6386.
- 1514 77 W. Graupner, G. Leditzky, G. Leising and U. Scherf, *Phys. Rev. B - Condens. Matter*  
1515 *Mater. Phys.*, 1996, **54**, 7610–7613.
- 1516 78 Z. A. Lampion, K. J. Barth, H. Lee, E. Gann, S. Engmann, H. Chen, M. Guthold, I.  
1517 McCulloch, J. E. Anthony, L. J. Richter, D. M. DeLongchamp and O. D. Jurchescu, *Nat.*  
1518 *Commun.*, 2018, **9**, 5130.
- 1519 79 D. Venkateshvaran, M. Nikolka, A. Sadhanala, V. Lemaire, M. Zelazny, M. Kepa, M.  
1520 Hurhangee, A. J. Kronemeijer, V. Pecunia, I. Nasrallah, I. Romanov, K. Broch, I.  
1521 McCulloch, D. Emin, Y. Olivier, J. Cornil, D. Beljonne and H. Sirringhaus, *Nature*, 2014,  
1522 **515**, 384–388.
- 1523 80 A. Karki, G. A. H. Wetzelaer, G. N. M. Reddy, V. Nádaždy, M. Seifrid, F. Schauer, G. C.  
1524 Bazan, B. F. Chmelka, P. W. M. Blom and T. Nguyen, *Adv. Funct. Mater.*, 2019, **29**,  
1525 1901109.
- 1526 81 N. Karl, in *Organic semiconductors. In: Queisser H.J. (eds) Festkörperprobleme*,  
1527 Springer Berlin Heidelberg, 1974, pp. 261–290.
- 1528 82 N. Karl, K.-H. Kraft, J. Marktanner, M. Münch, F. Schatz, R. Stehle and H.-M. Uhde, *J.*  
1529 *Vac. Sci. Technol. A Vacuum, Surfaces, Film.*, 1999, **17**, 2318–2328.
- 1530 83 K. H. Probst and N. Karl, *Phys. status solidi*, 1975, **27**, 499–508.
- 1531 84 O. D. Jurchescu, J. Baas and T. T. M. Palstra, *Appl. Phys. Lett.*, 2004, **84**, 3061–3063.
- 1532 85 P. K. Nayak, R. Rosenberg, L. Barnea-Nehoshtan and D. Cahen, *Org. Electron.*, 2013, **14**,  
1533 966–972.
- 1534 86 N. B. Kotadiya, A. Mondal, P. W. M. Blom, D. Andrienko and G. A. H. Wetzelaer, *Nat.*  
1535 *Mater.*, DOI:10.1038/s41563-019-0473-6.
- 1536 87 G. Zuo, M. Linares, T. Upreti and M. Kemerink, *Nat. Mater.*, 2019, **18**, 588–593.
- 1537 88 G. Zuo, Z. Li, O. Andersson, H. Abdalla, E. Wang and M. Kemerink, *J. Phys. Chem. C*,  
1538 2017, **121**, 7767–7775.
- 1539 89 S. Olthof, S. Mehraeen, S. K. Mohapatra, S. Barlow, V. Coropceanu, J.-L. Brédas, S. R.  
1540 Marder and A. Kahn, *Phys. Rev. Lett.*, 2012, **109**, 176601.
- 1541 90 M. L. Tietze, J. Benduhn, P. Pahner, B. Nell, M. Schwarze, H. Kleemann, M. Krammer,  
1542 K. Zojer, K. Vandewal and K. Leo, *Nat. Commun.*, 2018, **9**, 1182.
- 1543 91 M. L. Tietze, P. Pahner, K. Schmidt, K. Leo and B. Lüssem, *Adv. Funct. Mater.*, 2015, **25**,  
1544 2701–2707.

- 1545 92 B. Lüssem, M. Riede and K. Leo, *Doping of organic semiconductors*, 2013, vol. 210.
- 1546 93 H. Sirringhaus, *Adv. Mater.*, 2005, **17**, 2411–2425.
- 1547 94 R. R. Dasari, X. Wang, R. A. Wiscons, H. F. Haneef, A. Ashokan, Y. Zhang, M. S.  
1548 Fonari, S. Barlow, V. Coropceanu, T. V. Timofeeva, O. D. Jurchescu, J. Brédas, A. J.  
1549 Matzger and S. R. Marder, *Adv. Funct. Mater.*, 2019, **1904858**, 1904858.
- 1550 95 L. L. Chua, P. K. H. Ho, H. Sirringhaus and R. H. Friend, *Adv. Mater.*, 2004, **16**, 1609–  
1551 1615.
- 1552 96 L. Chua, J. Zaumseil, J. Chang, E. C.-W. Ou, P. K.-H. Ho, H. Sirringhaus and R. H.  
1553 Friend, *Nature*, 2005, **434**, 194–9.
- 1554 97 P. J. Diemer, Z. A. Lamport, Y. Mei, J. W. Ward, K. P. Goetz, W. Li, M. M. Payne, M.  
1555 Guthold, J. E. Anthony and O. D. Jurchescu, *Appl. Phys. Lett.*, 2015, **107**, 103303.
- 1556 98 A. F. Paterson, A. D. Mottram, H. Faber, M. R. Niazi, Z. Fei, M. Heeney and T. D.  
1557 Anthopoulos, *Adv. Electron. Mater.*, 2019, **5**, 1–9.
- 1558 99 Y.-Y. Noh, X. Cheng, A. Facchetti, H. Yan, H. Sirringhaus, J. Wang, M. Caironi and C.  
1559 Newman, *Chem. Mater.*, 2010, **22**, 1559–1566.
- 1560 100 W. L. Kalb, T. Mathis, S. Haas, A. F. Stassen and B. Batlogg, *Appl. Phys. Lett.*, 2007, **90**,  
1561 2005–2008.
- 1562 101 D. Knipp, P. Kumar, A. R. Völkel and R. A. Street, *Synth. Met.*, 2005, **155**, 485–489.
- 1563 102 S. Anand, K. P. Goetz, Z. A. Lamport, A. M. Zeidell and O. D. Jurchescu, *Appl. Phys.*  
1564 *Lett.*, 2019, **115**, 073301.
- 1565 103 M. Abe, T. Mori, I. Osaka, K. Sugimoto and K. Takimiya, *Chem. Mater.*, 2015, **27**, 5049–  
1566 5057.
- 1567 104 M. J. Kang, I. Doi, H. Mori, E. Miyazaki, K. Takimiya, M. Ikeda and H. Kuwabara, *Adv.*  
1568 *Mater.*, 2011, **23**, 1222–1225.
- 1569 105 Y. Mei, P. J. Diemer, M. R. Niazi, R. K. Hallani, K. Jarolimek, C. S. Day, C. Risko, J. E.  
1570 Anthony, A. Amassian and O. D. Jurchescu, *Proc. Natl. Acad. Sci.*, 2017, **114**, E6739–  
1571 E6748.
- 1572 106 I. N. Hulea, S. Fratini, H. Xie, C. L. Mulder, N. N. Iossad, G. Rastelli, S. Ciuchi and A. F.  
1573 Morpurgo, *Nat. Mater.*, 2006, **5**, 982–986.
- 1574 107 A. F. Stassen, R. W. I. De Boer, N. N. Losad and A. F. Morpurgo, *Appl. Phys. Lett.*, 2004,  
1575 **85**, 3899–3901.
- 1576 108 J. Veres, S. D. Ogier, S. W. Leeming, D. C. Cupertino and S. M. Khaffaf, *Adv. Funct.*  
1577 *Mater.*, 2003, **13**, 199–204.
- 1578 109 V. C. Sundar, *Science (80-. )*, 2004, **303**, 1644–1646.
- 1579 110 E. Menard, V. Podzorov, S.-H. Hur, A. Gaur, M. E. Gershenson and J. A. Rogers, *Adv.*  
1580 *Mater.*, 2004, **16**, 2097–2101.

- 1581 111 Y. Wu, A. R. Chew, G. A. Rojas, G. Sini, G. Haugstad, A. Belianinov, S. V. Kalinin, H.  
1582 Li, C. Risko, J. L. Brédas, A. Salleo and C. D. Frisbie, *Nat. Commun.*, 2016, **7**, 1–9.
- 1583 112 T. Sawabe, K. Okamura, T. Sueyoshi, T. Miyamoto, K. Kudo, N. Ueno and M. Nakamura,  
1584 *Appl. Phys. A Mater. Sci. Process.*, 2009, **95**, 225–232.
- 1585 113 M. Oehzelt, N. Koch and G. Heimel, *Nat. Commun.*, 2014, **5**, 1–8.
- 1586 114 C. Liu, Y. Xu and Y. Y. Noh, *Mater. Today*, 2015, **18**, 79–96.
- 1587 115 J. C. Scott, *J. Vac. Sci. Technol. A Vacuum, Surfaces, Film.*, 2003, **21**, 521–531.
- 1588 116 M. Waldrip, O. D. Jurchescu, D. J. Gundlach and E. G. Bittle, *Adv. Funct. Mater.*, 2019,  
1589 **1904576**, 1904576.
- 1590 117 D. Natali and M. Caironi, *Adv. Mater.*, 2012, **24**, 1357–1387.
- 1591 118 H. Baessler and G. Vaubel, *Phys. Rev. Lett.*, 1968, **21**, 615–617.
- 1592 119 R. W. I. de Boer and A. F. Morpurgo, *Phys. Rev. B*, 2005, **72**, 073207.
- 1593 120 M. Coll, K. P. Goetz, B. R. Conrad, C. A. Hacker, D. J. Gundlach, C. A. Richter and O. D.  
1594 Jurchescu, *Appl. Phys. Lett.*, 2011, **98**, 30–32.
- 1595 121 K. Kuribara, H. Wang, N. Uchiyama, K. Fukuda, T. Yokota, U. Zschieschang, C. Jaye, D.  
1596 Fischer, H. Klauk, T. Yamamoto, K. Takimiya, M. Ikeda, H. Kuwabara, T. Sekitani, Y. L.  
1597 Loo and T. Someya, *Nat. Commun.*, 2012, **3**, 723–727.
- 1598 122 C.-Y. Wang, C. Fuentes-Hernandez, J.-C. Liu, A. Dindar, S. Choi, J. P. Youngblood, R. J.  
1599 Moon and B. Kippelen, *ACS Appl. Mater. Interfaces*, 2015, **7**, 4804–4808.
- 1600 123 X. Jia, C. Fuentes-Hernandez, C.-Y. Wang, Y. Park and B. Kippelen, *Sci. Adv.*, 2018, **4**,  
1601 eaa01705.
- 1602 124 M. Nikolka, I. Nasrallah, B. Rose, M. K. Ravva, K. Broch, A. Sadhanala, D. Harkin, J.  
1603 Charmet, M. Hurhangee, A. Brown, S. Illig, P. Too, J. Jongman, I. McCulloch, J. Bredas  
1604 and H. Sirringhaus, *Nat. Mater.*, 2017, **16**, 356–362.
- 1605 125 J. A. Merlo and C. D. Frisbie, *J. Phys. Chem. B*, 2004, **108**, 19169–19179.
- 1606 126 V. Podzorov, E. Menard, A. Borissov, V. Kiryukhin, J. A. Rogers and M. E. Gershenson,  
1607 *Phys. Rev. Lett.*, 2004, **93**, 1–4.
- 1608 127 C. Pannemann, T. Diekmann and U. Hilleringmann, *J. Mater. Res.*, 2004, **19**, 1999–2002.
- 1609 128 T. Komoda, K. Kita, K. Kyuno and A. Toriumi, *Japanese J. Appl. Physics, Part 1 Regul.*  
1610 *Pap. Short Notes Rev. Pap.*, 2003, **42**, 3662–3665.
- 1611 129 Y. W. Wang, H. L. Cheng, Y. K. Wang, T. H. Hu, J. C. Ho, C. C. Lee, T. F. Lei and C. F.  
1612 Yeh, *Thin Solid Films*, 2004, **467**, 215–219.
- 1613 130 Z.-T. Zhu, J. T. Mason, R. Dieckmann and G. G. Malliaras, *Appl. Phys. Lett.*, 2002, **81**,  
1614 4643–4645.
- 1615 131 I. Kymissis, *Organic Field Effect Transistors*, Springer US, Boston, MA, 2009.

- 1616 132 L. Tsetseris and S. T. Pantelides, *Phys. Rev. B - Condens. Matter Mater. Phys.*, 2007, **75**,  
1617 1–4.
- 1618 133 S. G. J. Mathijssen, M. Kemerink, A. Sharma, M. Cölle, P. A. Bobbert, R. A. J. Janssen  
1619 and D. M. De Leeuw, *Adv. Mater.*, 2008, **20**, 975–979.
- 1620 134 C. Goldmann, D. J. Gundlach and B. Batlogg, *Appl. Phys. Lett.*, 2006, **88**, 063501.
- 1621 135 H. L. Gomes, P. Stallinga, M. Cölle, D. M. de Leeuw and F. Biscarini, *Appl. Phys. Lett.*,  
1622 2006, **88**, 082101.
- 1623 136 J. Kim, J. Jang, K. Kim, H. Kim, S. H. Kim and C. E. Park, *Adv. Mater.*, 2014, **26**, 7241–  
1624 7246.
- 1625 137 T. Sekitani, S. Iba, Y. Kato, Y. Noguchi, T. Someya and T. Sakurai, *Appl. Phys. Lett.*,  
1626 2005, **87**, 2003–2006.
- 1627 138 H. T. Nicolai, M. Kuik, G. A. H. Wetzelaer, B. De Boer, C. Campbell, C. Risko, J. L.  
1628 Brédas and P. W. M. Blom, *Nat. Mater.*, 2012, **11**, 882–887.
- 1629 139 J. Northrup and M. Chabinyk, *Phys. Rev. B - Condens. Matter Mater. Phys.*, 2003, **68**, 8–  
1630 11.
- 1631 140 D. Knipp and J. E. Northrup, *Adv. Mater.*, 2009, **21**, 2511–2515.
- 1632 141 T. Zimmerling, K. Mattenberger, M. Döbeli, M. J. Simon and B. Batlogg, *Phys. Rev. B -  
1633 Condens. Matter Mater. Phys.*, 2012, **85**, 2–5.
- 1634 142 M.-J. Tsai and H.-F. Meng, *J. Appl. Phys.*, 2005, **97**, 114502.
- 1635 143 G. A. H. Wetzelaer, M. Kuik, H. T. Nicolai and P. W. M. Blom, *Phys. Rev. B - Condens.  
1636 Matter Mater. Phys.*, 2011, **83**, 1–5.
- 1637 144 S. Scholz, D. Kondakov, B. Lüssem and K. Leo, *Chem. Rev.*, 2015, **115**, 8449–8503.
- 1638 145 M. Penconi, M. Cazzaniga, W. Panzeri, A. Mele, F. Cargnoni, D. Ceresoli and A. Bossi,  
1639 *Chem. Mater.*, 2019, **31**, 2277–2285.
- 1640 146 R. A. Street, M. Schoendorf, A. Roy and J. H. Lee, *Phys. Rev. B*, 2010, **81**, 205307:1-  
1641 205307:12.
- 1642 147 S. R. Cowan, A. Roy and A. J. Heeger, *Phys. Rev. B - Condens. Matter Mater. Phys.*,  
1643 2010, **82**, 1–10.
- 1644 148 H. Y. Mao, F. Bussolotti, D.-C. Qi, R. Wang, S. Kera, N. Ueno, A. T. S. Wee and W.  
1645 Chen, *Org. Electron.*, 2011, **12**, 534–540.
- 1646 149 J. Q. Zhong, H. Y. Mao, R. Wang, D. C. Qi, L. Cao, Y. Z. Wang and W. Chen, *J. Phys.  
1647 Chem. C*, 2011, **115**, 23922–23928.
- 1648 150 F. Bussolotti, J. Yang, A. Hinderhofer, Y. Huang, W. Chen, S. Kera, A. T. S. Wee and N.  
1649 Ueno, *Phys. Rev. B*, 2014, **89**, 115319.
- 1650 151 O. Rubel, S. D. Baranovskii, W. Stolz and F. Gebhard, *Phys. Rev. Lett.*, 2008, **100**,

- 1651 196602.
- 1652 152 G. Horowitz, R. Hajlaoui, H. Bouchriha, R. Bourguiga and M. Hajlaoui, *Adv. Mater.*,  
1653 1998, **10**, 923–927.
- 1654 153 G. Horowitz, R. Hajlaoui, D. Fichou and A. El Kassmi, *J. Appl. Phys.*, 1999, **85**, 3202–  
1655 3206.
- 1656 154 J. Huang, T. Minari, X. Liu, C. Liu, Y.-Y. Noh, R. Di Pietro and G. Li, *Phys. Rev. Appl.*,  
1657 2017, **8**, 034020.
- 1658 155 E. G. Bittle, J. I. Basham, T. N. Jackson, O. D. Jurchescu and D. J. Gundlach, *Nat.*  
1659 *Commun.*, 2016, **7**, 10908.
- 1660 156 E. G. Bittle, H. W. Ro, C. R. Snyder, S. Engmann, R. J. Kline, X. Zhang, O. D. Jurchescu,  
1661 D. M. DeLongchamp and D. J. Gundlach, *J. Polym. Sci. Part B Polym. Phys.*, 2017, **55**,  
1662 1063–1074.
- 1663 157 J. Smith, R. Hamilton, Y. Qi, A. Kahn, D. D. C. Bradley, M. Heeney, I. McCulloch and T.  
1664 D. Anthopoulos, *Adv. Funct. Mater.*, 2010, **20**, 2330–2337.
- 1665 158 U. Zschieschang, R. T. Weitz, K. Kern and H. Klauk, *Appl. Phys. A*, 2009, **95**, 139–145.
- 1666 159 R. Husermann and B. Batlogg, *Appl. Phys. Lett.*, 2011, **99**, 1–4.
- 1667 160 J. B. Chang and V. Subramanian, *Appl. Phys. Lett.*, 2006, **88**, 233513.
- 1668 161 A. Salleo and R. A. Street, *J. Appl. Phys.*, 2003, **94**, 471–479.
- 1669 162 D. K. Hwang, C. Fuentes-Hernandez, J. Kim, W. J. Potscavage, S.-J. Kim and B.  
1670 Kippelen, *Adv. Mater.*, 2011, **23**, 1293–1298.
- 1671 163 G. Gu and M. G. Kane, *Appl. Phys. Lett.*, 2008, **92**, 2006–2009.
- 1672 164 Y. H. Noh, S. Young Park, S. M. Seo and H. H. Lee, *Org. Electron. physics, Mater. Appl.*,  
1673 2006, **7**, 271–275.
- 1674 165 H. E. Katz, X. M. Hong, A. Dodabalapur and R. Sarpeshkar, *J. Appl. Phys.*, 2002, **91**,  
1675 1572–1576.
- 1676 166 V. Podzorov, *MRS Bull.*, 2013, **38**, 15–24.
- 1677 167 H. Xie, H. Alves and A. F. Morpurgo, *Phys. Rev. B*, 2009, **80**, 245305.
- 1678 168 C. Liu, T. Minari, X. Lu, A. Kumatani, K. Takimiya and K. Tsukagoshi, *Adv. Mater.*,  
1679 2011, **23**, 523–526.
- 1680 169 D. C. Hoesterey and G. M. Letson, *J. Phys. Chem. Solids*, 1963, **24**, 1609–1615.
- 1681 170 V. Podzorov, E. Menard, J. A. Rogers and M. E. Gershenson, *Phys. Rev. Lett.*, 2005, **95**,  
1682 1–4.
- 1683 171 T. Sakanoue and H. Sirringhaus, *Nat. Mater.*, 2010, **9**, 736–740.
- 1684 172 A. Laudari and S. Guha, *Phys. Rev. Appl.*, 2016, **6**, 044007.

- 1685 173 S. F. Nelson, Y.-Y. Lin, D. J. Gundlach and T. N. Jackson, *Appl. Phys. Lett.*, 1998, **72**,  
1686 1854–1856.
- 1687 174 K. P. Goetz and O. D. Jurchescu, in *Handbook of Organic Materials for Electronic and*  
1688 *Photonic Devices*, Elsevier, 2019, vol. 112, pp. 453–487.
- 1689 175 V. Podzorov, S. E. Sysoev, E. Loginova, V. M. Pudalov and M. E. Gershenson, *Appl.*  
1690 *Phys. Lett.*, 2003, **83**, 3504–3506.
- 1691 176 R. W. I. de Boer, M. Jochemsen, T. M. Klapwijk, A. F. Morpurgo, J. Niemax, A. K.  
1692 Tripathi and J. Pflaum, *J. Appl. Phys.*, 2004, **95**, 1196–1202.
- 1693 177 B. Fraboni, C. Femoni, I. Mencarelli, L. Setti, R. Di Pietro, A. Cavallini and A. Fraleoni-  
1694 Morgera, *Adv. Mater.*, 2009, **21**, 1835–1839.
- 1695 178 M. A. Lampert, *Phys. Rev.*, 1956, **103**, 1648–1656.
- 1696 179 P. Mark and W. Helfrich, *J. Appl. Phys.*, 1962, **33**, 205–215.
- 1697 180 D. Abbaszadeh, A. Kunz, G. A. H. Wetzelaer, J. J. Michels, N. I. Craciun, K. Koynov, I.  
1698 Lieberwirth and P. W. M. Blom, *Nat. Mater.*, 2016, **15**, 628–633.
- 1699 181 M. A. Lampert and P. Mark, *Current injection in solids*, Academic Press, 1970.
- 1700 182 S. Nešpůrek and J. Sworakowski, *Int. J. Radiat. Appl. Instrumentation. Part C. Radiat.*  
1701 *Phys. Chem.*, 1990, **36**, 3–12.
- 1702 183 O. Zmeskal, F. Schauer and S. Nespurek, *J. Phys. C Solid State Phys.*, 1985, **18**, 1873–  
1703 1884.
- 1704 184 F. Schauer, *J. Appl. Phys.*, 1998, **80**, 880.
- 1705 185 F. Schauer, R. Novotny and S. Nešpůrek, *J. Appl. Phys.*, 1997, **81**, 1244–1249.
- 1706 186 M. Nikolka, K. Broch, J. Armitage, D. Hanifi, P. J. Nowack, D. Venkateshvaran, A.  
1707 Sadhanala, J. Saska, M. Mascal, S. H. Jung, J. K. Lee, I. McCulloch, A. Salleo and H.  
1708 Siringhaus, *Nat. Commun.*, 2019, **10**, 1–9.
- 1709 187 J. S. Bonham and D. H. Jarvis, *Aust. J. Chem.*, 1977, **30**, 705–720.
- 1710 188 J. Bonham, *Aust. J. Chem.*, 1973, **26**, 927–939.
- 1711 189 S. Nespurek and J. Sworakowski, *J. Appl. Phys.*, 1980, **51**, 2098.
- 1712 190 J. Dacuña and A. Salleo, *Phys. Rev. B - Condens. Matter Mater. Phys.*, 2011, **84**, 195209.
- 1713 191 A. K. Muhammad and J. X. Sun, *Chinese Phys. B*, 2015, **24**, 047203.
- 1714 192 J. A. Geurst, *Phys. status solidi*, 1966, **15**, 107–118.
- 1715 193 J. Dacuña, W. Xie and A. Salleo, *Phys. Rev. B - Condens. Matter Mater. Phys.*, 2012, **86**,  
1716 115202.
- 1717 194 B. Blülle, R. Häusermann and B. Batlogg, *Phys. Rev. Appl.*, 2014, **1**, 034006.
- 1718 195 M. F. Calhoun, C. Hsieh and V. Podzorov, *Phys. Rev. Lett.*, 2007, **98**, 096402.

- 1719 196 M. Grünewald, P. Thomas and D. Würtz, *Phys. status solidi*, 1980, **100**, K139–K143.
- 1720 197 W. L. Kalb, F. Meier, K. Mattenberger and B. Batlogg, *Phys. Rev. B - Condens. Matter*  
1721 *Mater. Phys.*, 2007, **76**, 1–11.
- 1722 198 Y.-H. Lin, O. Solomeshch, A. D. Mottram, M. Heeney, T. D. Anthopoulos, M. R. Niazi,  
1723 N. Tessler, A. Amassian, Z. Fei, A. F. Paterson and A. R. Kirmani, *Adv. Electron. Mater.*,  
1724 2017, **4**, 1700464.
- 1725 199 M. Geiger, L. Schwarz, U. Zschieschang, D. Manske, J. Pflaum, J. Weis, H. Klauk and R.  
1726 T. Weitz, *Phys. Rev. Appl.*, 2018, **10**, 044023.
- 1727 200 G. Horowitz, R. Hajlaoui and P. Delannoy, *J. Phys. III*, 1995, **5**, 355–371.
- 1728 201 D. V. Lang, X. Chi, T. Siegrist, A. M. Sergent and A. P. Ramirez, *Phys. Rev. Lett.*, 2004,  
1729 **93**, 8–11.
- 1730 202 G. Fortunato, D. B. Meakin, P. Migliorato and P. G. Le Combers, *Philos. Mag. B*, 1988,  
1731 **57**, 573–586.
- 1732 203 W. L. Kalb, K. Mattenberger and B. Batlogg, *Phys. Rev. B - Condens. Matter Mater.*  
1733 *Phys.*, 2008, **78**, 1–11.
- 1734 204 W. L. Kalb and B. Batlogg, *Phys. Rev. B - Condens. Matter Mater. Phys.*, 2010, **81**, 1–13.
- 1735 205 P. J. Diemer, J. Hayes, E. Welchman, R. Hallani, S. J. Pookpanratana, C. A. Hacker, C. A.  
1736 Richter, J. E. Anthony, T. Thonhauser and O. D. Jurchescu, *Adv. Electron. Mater.*, 2017,  
1737 **3**, 1600294.
- 1738 206 T.-J. Ha, P. Sonar, B. Cobb and A. Dodabalapur, *Org. Electron.*, 2012, **13**, 136–141.
- 1739 207 D. Oberhoff, K. P. Pernstich, D. J. Gundlach and B. Batlogg, *IEEE Trans. Electron*  
1740 *Devices*, 2007, **54**, 17–25.
- 1741 208 R. Häusermann, K. Willa, B. Blülle, T. Morf, A. Facchetti, Z. Chen, J. Lee and B.  
1742 Batlogg, *Org. Electron.*, 2016, **28**, 306–313.
- 1743 209 S. Watanabe, H. Sugawara, R. Häusermann, B. Blülle, A. Yamamura, T. Okamoto and J.  
1744 Takeya, *Commun. Phys.*, 2018, **1**, 37.
- 1745 210 V. V. Brus, C. M. Proctor, N. A. Ran and T.-Q. Nguyen, *Adv. Energy Mater.*, 2016, **6**,  
1746 1502250.
- 1747 211 L. Zhang, H. Nakanotani and C. Adachi, *Appl. Phys. Lett.*, 2013, **103**, 093301.
- 1748 212 H. Hirwa, S. Pittner and V. Wagner, *Org. Electron. physics, Mater. Appl.*, 2015, **24**, 303–  
1749 314.
- 1750 213 H. Hatta, Y. Miyagawa, T. Nagase, T. Kobayashi, T. Hamada, S. Murakami, K.  
1751 Matsukawa and H. Naito, *Appl. Sci.*, 2018, **8**, 1493.
- 1752 214 L. Xu, J. Wang and J. W. P. Hsu, *Phys. Rev. Appl.*, 2016, **6**, 1–10.
- 1753 215 P. P. Boix, G. Garcia-Belmonte, U. Muñecas, M. Neophytou, C. Waldauf and R. Pacios,

- 1754 *Appl. Phys. Lett.*, 2009, **95**, 2009–2011.
- 1755 216 E. Von Hauff, *J. Phys. Chem. C*, 2019, **123**, 11329–11346.
- 1756 217 T. Walter, R. Herberholz, C. Müller and H. W. Schock, *J. Appl. Phys.*, 1996, **80**, 4411–  
1757 4420.
- 1758 218 S. Wang, P. Kaienburg, B. Klingebiel, D. Schillings and T. Kirchartz, *J. Phys. Chem. C*,  
1759 2018, **122**, 9795–9803.
- 1760 219 J. Scherbel, P. H. Nguyen, G. Paasch, W. Brütting and M. Schwoerer, *J. Appl. Phys.*,  
1761 1998, **83**, 5045–5055.
- 1762 220 T. Okachi, T. Nagase, T. Kobayashi and H. Naito, *Appl. Phys. Lett.*, 2009, **94**, 043301.
- 1763 221 D. Dascalu, *Int. J. Electron.*, 1966, **21**, 183–200.
- 1764 222 D. Dascălu, *Solid. State. Electron.*, 1968, **11**, 491–499.
- 1765 223 K. Takagi, T. Nagase, T. Kobayashi and H. Naito, *Appl. Phys. Lett.*, 2016, **108**, 053305.
- 1766 224 H. Hase, T. Okachi, S. Ishihara, T. Nagase, T. Kobayashi and H. Naito, *Thin Solid Films*,  
1767 2014, **554**, 218–221.
- 1768 225 F. Bussolotti, J. Yang, M. Hiramoto, T. Kaji, S. Kera and N. Ueno, *Phys. Rev. B -  
1769 Condens. Matter Mater. Phys.*, 2015, **92**, 1–7.
- 1770 226 Y. Nakayama, S. Machida, T. Minari, K. Tsukagishi, Y. Noguchi and H. Ishii, *Appl. Phys.  
1771 Lett.*, 2008, **93**, 173305.
- 1772 227 T. Sueyoshi, H. Fukagawa, M. Ono, S. Kera and N. Ueno, *Appl. Phys. Lett.*, 2009, **95**, 3–  
1773 6.
- 1774 228 K. Lee, M. S. Oh, S. J. Mun, K. H. Lee, T. W. Ha, J. H. Kim, S. H. K. Park, C. S. Hwang,  
1775 B. H. Lee, M. M. Sung and S. Im, *Adv. Mater.*, 2010, **22**, 3260–3265.
- 1776 229 M. Meier, S. Karg, K. Zuleeg, W. Brütting and M. Schwoerer, *J. Appl. Phys.*, 1998, **84**,  
1777 87–92.
- 1778 230 D. P. K. Tsang and C. Adachi, *Sci. Rep.*, 2016, **6**, 1–10.
- 1779 231 D. V. Lang, *J. Appl. Phys.*, 1974, **45**, 3023–3032.
- 1780 232 O. Gaudin, R. B. Jackman, T. P. Nguyen and P. Le Rendu, *J. Appl. Phys.*, 2001, **90**, 4196–  
1781 4204.
- 1782 233 T. P. Nguyen, J. Ip, O. Gaudin and R. B. Jackman, *Eur. Phys. J. Appl. Phys.*, 2004, **27**,  
1783 219–222.
- 1784 234 T. P. Nguyen, C. Renaud, P. Le Rendu and S. H. Yang, *Phys. Status Solidi Curr. Top.  
1785 Solid State Phys.*, 2009, **6**, 1856–1861.
- 1786 235 S. Neugebauer, J. Rauh, C. Deibel and V. Dyakonov, *Appl. Phys. Lett.*, 2012, **100**, 1–5.
- 1787 236 W. B. Jackson, N. M. Amer, A. C. Boccara and D. Fournier, *Appl. Opt.*, 1981, **20**, 1333.

- 1788 237 L. S. C. Pingree, O. G. Reid and D. S. Ginger, *Adv. Mater.*, 2009, **21**, 19–28.
- 1789 238 Y. Wu, X. Ren, K. A. McGarry, M. J. Bruzek, C. J. Douglas and C. D. Frisbie, *Adv.*  
1790 *Electron. Mater.*, 2017, **3**, 1–8.
- 1791 239 B. C. Hoffman, S. Pazoki, A. Apperson and D. B. Dougherty, *Phys. status solidi – Rapid*  
1792 *Res. Lett.*, 2019, **13**, 1800486.
- 1793 240 C.-W. Huang, X. You, P. J. Diemer, A. J. Petty, J. E. Anthony, O. D. Jurchescu and J. M.  
1794 Atkin, *Commun. Chem.*, 2019, **2**, 22.
- 1795 241 J. Rivnay, S. C. B. Mannsfeld, C. E. Miller, A. Salleo and M. F. Toney, *Chem. Rev.*, 2012,  
1796 **112**, 5488–5519.
- 1797 242 T. Someya, A. Dodabalapur, J. Huang, K. C. See and H. E. Katz, *Adv. Mater.*, 2010, **22**,  
1798 3799–3811.
- 1799 243 X. Wu, S. Mao, J. Chen and J. Huang, *Adv. Mater.*, 2018, **30**, 1–7.
- 1800 244 K. Xu, Y. Lu and K. Takei, *Adv. Mater. Technol.*, 2019, **4**, 1800628.
- 1801 245 X. Wu, Y. Ma, G. Zhang, Y. Chu, J. Du, Y. Zhang, Z. Li, Y. Duan, Z. Fan and J. Huang,  
1802 *Adv. Funct. Mater.*, 2015, **25**, 2138–2146.
- 1803 246 A. K. Bansal, S. Hou, O. Kulyk, E. M. Bowman and I. D. W. Samuel, *Adv. Mater.*, 2015,  
1804 **27**, 7638–7644.
- 1805 247 J. H. Park, J. E. Royer, E. Chagarov, T. Kaufman-Osborn, M. Edmonds, T. Kent, S. Lee,  
1806 W. C. Trogler and A. C. Kummel, *J. Am. Chem. Soc.*, 2013, **135**, 14600–14609.
- 1807 248 X. Yu, N. Zhou, S. Han, H. Lin, D. B. Buchholz, J. Yu, R. P. H. Chang, T. J. Marks and  
1808 A. Facchetti, *J. Mater. Chem. C*, 2013, **1**, 6532.
- 1809 249 C. Zhang, P. Chen and W. Hu, *Chem. Soc. Rev.*, 2015, **44**, 2087–2107.
- 1810 250 Y. H. Lee, M. Jang, M. Y. Lee, O. Y. Kweon and J. H. Oh, *Chem*, 2017, **3**, 724–763.
- 1811 251 L. Torsi, A. Dodabalapur, L. Sabbatini and P. G. Zamboni, *Sensors Actuators, B Chem.*,  
1812 2000, **67**, 312–316.
- 1813 252 T. Someya, H. E. Katz, A. Gelperin, A. J. Lovinger and A. Dodabalapur, *Appl. Phys. Lett.*,  
1814 2002, **81**, 3079–3081.
- 1815 253 B. Crone, A. Dodabalapur, A. Gelperin, L. Torsi, H. E. Katz, A. J. Lovinger and B. Bao,  
1816 *Appl. Phys. Lett.*, 2001, **78**, 2229–2231.
- 1817 254 W. Huang, J. Sinha, M.-L. Yeh, J. F. M. Hardigree, R. LeCover, K. Besar, A. M. Rule, P.  
1818 N. Breyse and H. E. Katz, *Adv. Funct. Mater.*, 2013, **23**, 4094–4104.
- 1819 255 F. Liao, C. Chen and V. Subramanian, *Sensors Actuators, B Chem.*, 2005, **107**, 849–855.
- 1820 256 G. Tang, S. S. Y. Chen, K. H. Lee, A. Pivrikas, M. Aljada, P. L. Burn, P. Meredith and P.  
1821 E. Shaw, *Appl. Phys. Lett.*, 2013, **102**, 243301.
- 1822 257 J. Huang, J. Miragliotta, A. Becknell and H. E. Katz, *J. Am. Chem. Soc.*, 2007, **129**, 9366–

- 1823 9376.
- 1824 258 A.-M. Andringa, W. S. Christian Roelofs, M. Sommer, M. Thelakkat, M. Kemerink and  
1825 D. M. de Leeuw, *Appl. Phys. Lett.*, 2012, **101**, 153302.
- 1826 259 A. M. Andringa, M. J. Spijkman, E. C. P. Smits, S. G. J. Mathijssen, P. A. va. Hal, S.  
1827 Setayesh, N. P. Willard, O. V. Borshchev, S. A. Ponomarenko, P. W. M. Blom and D. M.  
1828 de Leeuw, *Org. Electron. physics, Mater. Appl.*, 2010, **11**, 895–898.
- 1829 260 K. Besar, S. Yang, X. Guo, W. Huang, A. M. Rule, P. N. Breysse, I. J. Kymissis and H. E.  
1830 Katz, *Org. Electron.*, 2014, **15**, 3221–3230.
- 1831 261 K. Besar, J. Dailey, X. Zhao and H. E. Katz, *J. Mater. Chem. C*, 2017, **5**, 6506–6511.
- 1832 262 D. Duarte, D. Sharma, B. Cobb and A. Dodabalapur, *Appl. Phys. Lett.*, 2011, **98**, 133302.
- 1833 263 G. Schwartz, B. C.-K. Tee, J. Mei, A. L. Appleton, D. H. Kim, H. Wang and Z. Bao, *Nat.*  
1834 *Commun.*, 2013, **4**, 1859.
- 1835 264 S. Hannah, A. Davidson, I. Glesk, D. Uttamchandani, R. Dahiya and H. Gleskova, *Org.*  
1836 *Electron.*, 2018, **56**, 170–177.
- 1837 265 A. Spanu, L. Pinna, F. Viola, L. Seminara, M. Valle, A. Bonfiglio and P. Cosseddu, *Org.*  
1838 *Electron.*, 2016, **36**, 57–60.
- 1839 266 N. V. V. Subbarao, S. Mandal, M. Gedda, P. K. Iyer and D. K. Goswami, *Sensors*  
1840 *Actuators A Phys.*, 2018, **269**, 491–499.
- 1841 267 N. T. Boileau, R. Cranston, B. Mirka, O. A. Melville and B. H. Lessard, *RSC Adv.*, 2019,  
1842 **9**, 21478–21485.
- 1843 268 T. Yokota, P. Zalar, M. Kaltenbrunner, H. Jinno, N. Matsuhisa, H. Kitanosako, Y.  
1844 Tachibana, W. Yukita, M. Koizumi and T. Someya, *Sci. Adv.*, 2016, **2**, e1501856.
- 1845 269 M. Zhu, S. Lv, Q. Wang, G. Zhang, H. Lu and L. Qiu, *Nanoscale*, 2016, **8**, 7738–7748.
- 1846 270 M. C. Hamilton and J. Kanicki, *IEEE J. Sel. Top. Quantum Electron.*, 2004, **10**, 840–848.
- 1847 271 H. L. Park, I. H. Lee, C. M. Keum, S. H. Lee and S. D. Lee, *Thin Solid Films*, 2016, **619**,  
1848 297–301.
- 1849 272 H. Xu, J. Li, B. H. K. Leung, C. C. Y. Poon, B. S. Ong, Y. Zhang and N. Zhao,  
1850 *Nanoscale*, 2013, **5**, 11850.
- 1851 273 Z. Sun, J. Li and F. Yan, *J. Mater. Chem.*, 2012, **22**, 21673.
- 1852 274 C. H. Kim, M. H. Choi, S. H. Lee, J. Jang and S. Kirchmeyer, *Appl. Phys. Lett.*, 2010, **96**,  
1853 94–97.
- 1854 275 Y. Chu, X. Wu, J. Lu, D. Liu, J. Du, G. Zhang and J. Huang, *Adv. Sci.*, 2016, **3**, 1500435.
- 1855 276 L. Sang, M. Liao and M. Sumiya, *Sensors (Switzerland)*, 2013, **13**, 10482–10518.
- 1856 277 C. S. Smithson, Y. Wu, T. Wigglesworth and S. Zhu, *Adv. Mater.*, 2015, **27**, 228–233.

- 1857 278 T.-Y. Huang, C.-H. Chen, C.-C. Lin, Y.-J. Lee, C.-L. Liu and G.-S. Liou, *J. Mater. Chem. C*, 2019, **7**, 11014–11021.  
1858
- 1859 279 A. Ciavatti, L. Basiricò, I. Fratelli, S. Lai, P. Cosseddu, A. Bonfiglio, J. E. Anthony and B. Fraboni, *Adv. Funct. Mater.*, 2019, **29**, 1806119.  
1860
- 1861 280 L. Basiricò, A. Ciavatti, T. Cramer, P. Cosseddu, A. Bonfiglio and B. Fraboni, *Nat. Commun.*, DOI:10.1038/ncomms13063.  
1862
- 1863 281 T. Morf, T. Zimmerling, S. Haas and B. Batlogg, *arXiv*.
- 1864 282 L. Basiricò, A. F. Basile, P. Cosseddu, S. Gerardin, T. Cramer, M. Bagatin, A. Ciavatti, A. Paccagnella, A. Bonfiglio and B. Fraboni, *ACS Appl. Mater. Interfaces*, 2017, **9**, 35150–35158.  
1865  
1866
- 1867 283 H. He, W. He, J. Mai, J. Wang, Z. Zou, D. Wang, J. Feng, A. Zhang, Z. Fan, S. Wu, M. Zeng, J. Gao, G. Zhou, X. Lu and J. M. Liu, *J. Mater. Chem. C*, 2019, **7**, 1913–1918.  
1868
- 1869 284 Y. van de Burgt, A. Melianas, S. T. Keene, G. Malliaras and A. Salleo, *Nat. Electron.*, 2018, **1**, 386–397.  
1870
- 1871 285 F. Alibart, S. Pieutin, D. Guérin, C. Novembre, S. Lenfant, K. Lmimouni, C. Gamrat and D. Vuillaume, *Adv. Funct. Mater.*, 2010, **20**, 330–337.  
1872
- 1873 286 F. Alibart, S. Pleutin, O. Bichler, C. Gamrat, T. Serrano-Gotarredona, B. Linares-Barranco and D. Vuillaume, *Adv. Funct. Mater.*, 2012, **22**, 609–616.  
1874
- 1875 287 T. Zhang, D. Guérin, F. Alibart, D. Vuillaume, K. Lmimouni, S. Lenfant, A. Yassin, M. Oçafrain, P. Blanchard and J. Roncali, *J. Phys. Chem. C*, 2017, **121**, 10131–10139.  
1876
- 1877 288 D. I. Son, C. H. You, W. T. Kim, J. H. Jung and T. W. Kim, *Appl. Phys. Lett.*, 2009, **94**, 1–4.  
1878
- 1879 289 C. Novembre, D. Guérin, K. Lmimouni, C. Gamrat and D. Vuillaume, *Appl. Phys. Lett.*, 2008, **92**, 14–17.  
1880
- 1881 290 E. Orgiu and P. Samorì, *Adv. Mater.*, 2014, **26**, 1827–1844.
- 1882 291 M. Irie, T. Fukaminato, K. Matsuda and S. Kobatake, *Chem. Rev.*, 2014, **114**, 12174–12277.  
1883
- 1884 292 E. Orgiu, N. Crivillers, M. Herder, L. Grubert, M. Pätzelt, J. Frisch, E. Pavlica, D. T. Duong, G. Bratina, A. Salleo, N. Koch, S. Hecht and P. Samorì, *Nat. Chem.*, 2012, **4**, 675–679.  
1885  
1886
- 1887 293 T. Leydecker, M. Herder, E. Pavlica, G. Bratina, S. Hecht, E. Orgiu and P. Samorì, *Nat. Nanotechnol.*, 2016, **11**, 769–775.  
1888
- 1889

*The phenomenon of charge carrier trapping in organic semiconductors and their impact on electronic devices are reviewed*

